AMERICAN UNIVERSITY OF BEIRUT

EFFECTS OF FLUCTUATIONS ON MAGNETIC RECONNECTION AND HEATING IN THE SOLAR CORONA

by
MOSTAFA MOHAMMED HAMMOUD

A thesis
submitted in partial fulfillment of the requirements
for the degree of Doctor of Philosophy in Astrophysics
to the Department of Physics
of the Faculty of Arts and Sciences
at the American University of Beirut

Beirut, Lebanon
June 2020

AMERICAN UNIVERSITY OF BEIRUT

EFFECTS OF FLUCTUATIONS ON MAGNETIC RECONNECTION AND HEATING IN THE SOLAR CORONA

by

MOSTAFA MOHAMMED HAMMOUD

Approved by:

Dr. Mounib El Eid, Professor — Advisor

Physics Department at AUB - Lebanon

Dr. Ghassan Antar, Professor — Member of Committee

Physics Department at AUB - Lebanon

Dr. Marwan Darwish, Professor — Member of Committee

Mechanical Engineering Department at AUB - Lebanon

Hantao Ji Digitally signed by Hantao Ji Date: 2020.07.27 22:00:44 -04'00'

Dr. Hantao Ji, Professor — Member of Committee

Princeton Plasma Physics Laboratory - USA

Dr. Maher Dayeh, Adjoint Professor — Member of Committee

Department of Physics and Astronomy, University of Texas at San Antonio – USA

Principal Scientist, Space Science and Engineering Division, Southwest Research Institute – USA

Date of thesis defense: July 14, 2020

AMERICAN UNIVERSITY OF BEIRUT

THESIS, DISSERTATION, PROJECT RELEASE FORM

Student Name: Hammoud Mostafa Mohammed
Last First Middle

⬭ Master's Thesis ⬭ Master's Project ⊠ Doctoral Dissertation

☒ I authorize the American University of Beirut to: (a) reproduce hard or electronic copies of my thesis, dissertation, or project; (b) include such copies in the archives and digital repositories of the University; and (c) make freely available such copies to third parties for research or educational purposes.

☐ I authorize the American University of Beirut, to: (a) reproduce hard or electronic copies of it; (b) include such copies in the archives and digital repositories of the University; and (c) make freely available such copies to third parties for research or educational purposes after: **One ___ year from the date of submission of my thesis, dissertation or project.**
Two ___ years from the date of submission of my thesis , dissertation or project.
Three ___ years from the date of submission of my thesis , dissertation or project.

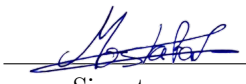

Signature Friday 11/09/2020
Date

This form is signed when submitting the thesis, dissertation, or project to the University Libraries

Acknowledgements

A thesis project is built in an environment of support and motivation. This project has been supported by AUB's IT's Research computing team where the simulations were run on the HPC cluster Arza.

A big gratitude to my advisor, Prof. Mounib El Eid, for his utmost supervision and care. His motivation and enthusiasm to work have provided me with the continuous push forward and forward in thesis research.

I would also like to thank my committee members, Prof. Ghassan Antar, Prof. Marwan Darwish, Prof. Maher Dayeh and Prof. Hantao Ji for their encouragement.

A special thanks to Prof. Ghassan Antar, for all the discussions and the time he spent sharing his knowledge with me and helping me complete my thesis.

Further thanks to Prof. Marwan Darwish and Prof. Maher Dayeh for their detailed and constructive comments and for their essential support throughout this work.

Above all, I thank my parents, my brothers and my sister for supporting me throughout all my studies at AUB and for providing me with a lovely environment.

Finally, I would like to thank my wife, Malak, for all the love, kindness and support she has shown during the past five years, the period it took to finalize this thesis.

An Abstract of the Thesis of

Mostafa Mohammed Hammoud for PhD of Physics
Major: Astrophysics

Title: Effects of Fluctuations on Magnetic Reconnection and Heating in the Solar Corona

The solar corona exhibits unusually high temperatures ($\sim 10^6$ K) compared to the temperature in the Sun's photosphere ($\sim$ 5800 K). This coronal heating is one of the fundamental problems in solar physics that is yet to be resolved. Magnetic reconnection is thought to play a critical role in driving this enigmatic heating process. In this work, we present a newly-developed resistive magnetohydrodynamic (MHD) numerical model in which we investigate the effects of magnetic fluctuations, generated by the photospheric motion of footpoints at which the coronal field lines are anchored, on the reconnection rate and the heating process in the solar corona. The treatment of magnetic reconnection is done using OpenFOAM for numerically solving the resistive MHD equations, which are modified by implementing the fluctuations as source or sink terms. Our results show that the use of the uniform resistivity model in the framework of resistive MHD leads to slow reconnection process even if fluctuations are added. Moreover, compared to the case of no fluctuations using the Spitzer resistivity model and starting with a zero initial velocity, it is noticed when sinusoidal fluctuations are added that: (1) the reconnection process is enhanced since the reconnection rate ηJ_z is almost 10 times higher, and (2) the magnetic energy is diffused fast and extra amount of heat and high values of particle acceleration (jets) are generated. Furthermore, the results show also that sinusoidal fluctuations of shorter wavelength promote a faster formation of X-points through plasmoid restructuring of the magnetic field lines. The reconnection rate is thus enhanced leading to a rapid heating process by pumping extra thermal energy in the coronal regions surrounding the reconnection site. Therefore, the magnetic reconnection process influenced by magnetic fluctuations can be considered as an effective candidate which contributes in the solar coronal heating.

Contents

List of Figures

List of Tables

Chapter 1

Introduction

1.1 Introduction

Plasma is pervasive in the universe. Tremendous amount of nuclear energy is continuously released by the stars in our galaxy. Due to this energy, particles escape stellar surfaces, forming plasma that streams into space. For example, the plasma streaming from the Sun, the solar wind, interacts with the Earth's magnetosphere leading to geomagnetic storms, and to the formation of the auroras [4, 5]. An important candidate is believed to be behind all these phenomena is the magnetic reconnection.

Magnetic reconnection (MGR) is widespread in astrophysical plasma systems and in laboratory plasma devices as well [6]. It is a topological rearrangement of field line directions. Such rearrangement is initiated by diffusion, caused by turbulence and other processes, which in turn breaks down the frozen-in condition between field lines and plasma particles.

MGR is an active area of theoretical research in astrophysical plasma physics. It is believed to be the power source behind various phenomena, such as solar flares. MGR also frequently controls transport of charged particles and heat in interstellar and intergalactic media [7, 8]. As mentioned in [9], the temperature

increase in the solar transition region is a response to MGR that takes place between two magnetic flux tubes in the photosphere. Moreover, the temperature of the solar corona is higher by two orders of magnitude compared to that of the Sun's photosphere. This anomalous temperature denotes a solar mystery known as the "coronal heating problem". Although it is still not clear whether waves or reconnection play a dominant role in heating the solar corona [10], we believe that the MGR process plays an important role in this heating.

In March of 2015, NASA launched a mission called "Magnetospheric Multiscale Mission" or simply "MMS" aimed at obtaining information about the MGR between the plasma associated with the solar wind and the plasma of the Earth's magnetosphere. More recently, in August of 2018, NASA launched another mission titled the "Parker Solar Probe", which aims at finding answers about many mysterious issues in the solar atmosphere including the coronal heating problem.

1.2 NASA's Latest Launch - Parker Solar Probe

NASA's Parker Solar Probe launched, from Florida (USA), on the 12^{th} of August, 2018. It began its journey to the Sun, where it would undertake a landmark mission. The spacecraft, shown by Figure (1.1), expands our understanding of the star that makes life on Earth possible.

The Parker Solar Probe (PSP) is a historic mission flying into the Sun's corona for the first time, exploring the last and most important region of the solar system to be visited by spacecraft. The Sun is the only star we can study up close. By studying our star we can learn more about stars throughout the universe. The Sun is the source of the solar wind, a flow of ionized gases from the Sun that stream past Earth at speeds of more than 500 km/sec. The spacecraft and instruments of PSP are protected by a thermal protection system composed mainly of carbon foam blocks. Because the carbon composite shield is such a poor conductor of heat, the spacecraft and scientific instruments behind it will be at about room

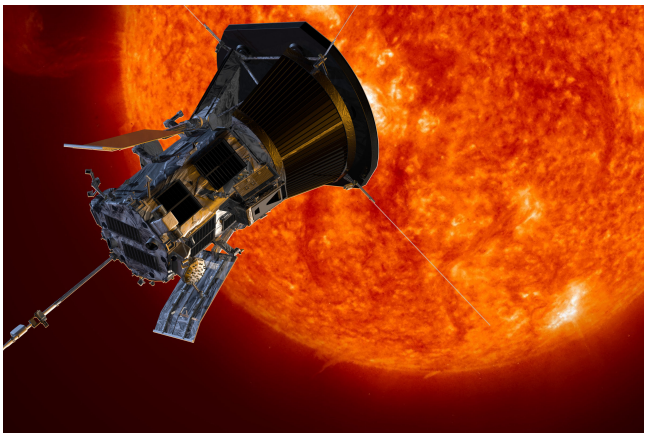

Figure 1.1: The Parker Solar Probe launched by NASA on the 12^{th} of August, 2018. This NASA's spacecraft will zoom close to the Sun 24 times between 2018 and 2025 gathering a variety of data about the Sun's structure and magnetic and electric fields.

temperature; protecting most of the spacecraft's components from the brunt of the heat encountered near the Sun.

The PSP flies through the Sun's atmosphere as close as 6.2 million kilometers from our star's surface. It will zoom close to the Sun 24 times between 2018 and 2025, gathering a variety of data about the Sun's structure as well as its magnetic and electric fields. The probe will spend a total of 30 hours within the corona. This helped scientists in understanding why the Sun's outer atmosphere is more than 200 times hotter than the Sun's surface. It will fly close enough to watch the solar wind speeds up from subsonic to supersonic. It allowed scientists to achieve a better understanding of how and why this acceleration happens. For more information, please visit [11].

1.3 Coronal Field Lines

The coronal field lines, open and closed, are always observed in the solar atmosphere. They are actually magnetic field lines surrounded by plasma particles ejected out from and below the solar surface. The continual existence of those

field lines indicate that the solar magnetic field is always maintained. A possible mechanism for maintaining the solar magnetic field was the dynamo process, first suggested by Larmor since 1919 [12]. The basis of his theory is that the magnetic field can be sustained by the motion of the highly ionized plasma in the Sun. Solar physicists have decomposed the solar magnetic field into poloidal and toroidal parts. The toroidal part is believed to lead to sunspots, while the poloidal field corresponds to the large-scale coronal field [13]. The solar field can be maintained by the fluid flow if there is persistent conversion between its two components. To understand such conversion, we need an equation relating the magnetic field to the fluid velocity. This equation is the famous induction equation derived from coupling between Maxwell's equations and Ohm's law,

$$\frac{\partial \vec{B}}{\partial t} = \vec{\nabla} \times (\vec{u} \times \vec{B}) + \frac{\eta}{\mu_0} \vec{\nabla}^2 \vec{B}, \tag{1.1}$$

where $\vec{B}$ is the magnetic field, $\vec{u}$ is the fluid velocity, η is the resistivity of the conducting fluid, and μ_0 is the permeability of vacuum. The parameter $\frac{\eta}{\mu_0}$ refers to magnetic diffusivity. The induction equation shows that the evolution of the magnetic field follows two processes given by the two terms on the right hand side. The magnetic field gets enhanced by the first term (the convection term), and, in contrast, it gets diffused by the second term (the diffusion term).

According to Equation (1.1), it is evident that any gradients in the fluid velocity will induce toroidal field from poloidal field. These gradients of velocity are believed to be due to the presence of shears or differential rotation in the interior of the Sun. This is known as the ω-effect. Thus, the large-scale poloidal field leads to toroidal field via the ω-effect. However, the generation of poloidal field from toroidal field is not straightforward. Parker in 1955 [14] considered that the interactions of small-scale magnetic field and turbulent fluid velocity will produce large-scale poloidal field from a toroidal field. This is known as the α-effect. Alternatively, another scenario was proposed by Babcock [15] and Leighton [16]

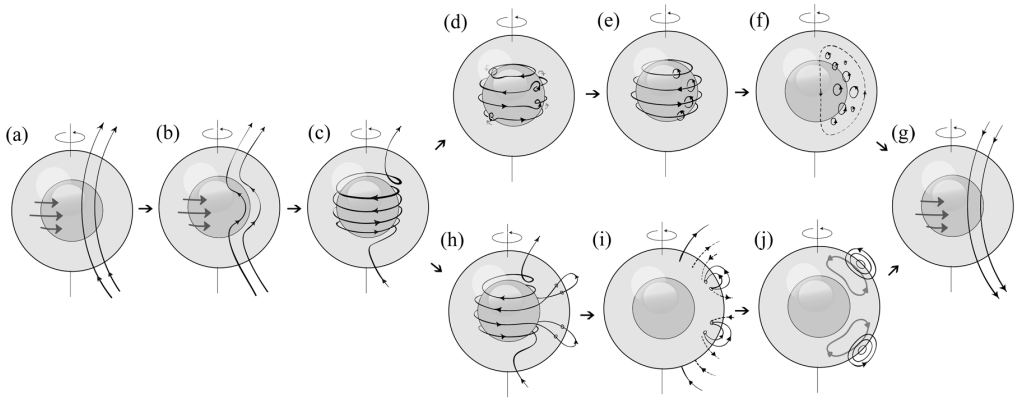

Figure 1.2: Illustration of the ω-effect, the α-effect and the Babcock-Leighton mechanism, which are proposed to model the evolution of the solar magnetic field lines. (a) is the initial poloidal field. (b) and (c) represent the generation of the toroidal field by differential rotation, the ω-effect. (d), (e), (f) and (g) show the α-effect during which the toroidal field transforms into poloidal field. (h) and (i) represent the beginning of the Babcock-Leighton mechanism: toroidal flux tubes buoyantly rise to the surface forming sunspots and coronal loops. In (j), the magnetic fields from the bipolar regions diffuse and reconnect with each other and with the polar fields generating the final large-scale poloidal field in (g).

explaining the poloidal field regeneration. Strong gradients of differential rotation take place in the tachocline layer between the radiative and convective zones. The tachocline is thus responsible for the generation of the strong toroidal field leading to reduce the local density of the plasma. Regions of strong magnetic fields are thus buoyant. Only a very strong magnetic field is buoyant enough to rise from the tachocline to the solar surface and form sunspot pairs [17]. The Babcock-Leighton mechanism suggested that the regeneration of poloidal field from toroidal field is a result of the diffusion and reconnection processes of the magnetic field of the sunspot pairs.

The ω-effect, the α-effect and the Babcock-Leighton mechanism are all illustrated in Figure (1.2) [18]. In the photosphere, convection pushes material toward the edge of the so called "supergranules", which are very large conception cells. As a result, vertical magnetic field lines pile up around the supergranules, creating

large and wandering magnetic field lines. As illustrated in images (h) and (i) of Figure (1.2), coronal loops thus form and linked to the photosphere at locations called footpoints.

1.4 Fluid Approach of MGR

Plasma is more accurately modeled using kinetic theory where it is described by distribution functions in phase space and time. Plasma dynamics is completely described using Boltzmann equation coupled with Maxwell's equations for electromagnetic fields [19]. Averaging over velocity space for each plasma species, the resulting equations comprise the two-fluid plasma model. Using several approximations, the two-fluid equations are then combined to form the magnetohydrodynamics (MHD) model [20]. The main interest of a fluid model over the kinetic model is the reduced dimensionality. Physics is lost in this reduction but a huge amount of phenomena and mechanisms based on plasma physics are still well described in the fluid model [21, 22]. In the present work, we are modeling the MGR process in the framework of resistive MHD.

1.5 Early Models of MGR

MGR was first investigated by Sweet [23] and Parker [24] using incompressible MHD. A drawback of their approach is the long time-scale of the energy release, which is approximately about 0.3 years. This contradicts the observations which indicate time-scales in the order of minutes to hours in the case of solar flares [25]. Another problem is related to the size of the diffusion region [26]. According to [8], the typical length-scale of the coronal loop is $L \sim 10^7$ m, and the thickness of the diffusion region represented by a current sheet is $\rho_i \sim 10$ m (ρ_i is the ion-Larmor radius). It is emphasized that magnetic field lines break on microscopic scales, but nonetheless the energy is stored and the plasma responds on global

scales. This implies that the dynamics of large-scale motion is linked to the behavior of the magnetic fields at small scales. In other words, it is challenging to find out how the stored magnetic energy is released so fast. According to the Petscheck modeling [27], the fast reconnection time was obtained through introducing magneto-sonic shocks. This idea has been accepted for a relatively long time. However, the formation of such shocks were questionable and it was actually based purely on geometrical arguments [28, 29].

1.6 Link between Turbulence and MGR

A different approach [30], which was based on two-dimensional simulation of resistive MHD reconnection, reproduced the Petscheck model's results only if resistivity is enhanced within the current sheet. Various works have applied the high resistivity model including the Hall effect [31], electron pressure [32], ambipolar diffusion [33], and kinetic effect [34]. However, the question is how one would understand the enhanced resistivity within the diffusion region. In the work done by [35], turbulence caused by some fluctuations is invoked in order to explain the enhanced resistivity. According to [36], the effect of turbulence may be described by an effective resistivity, which should lead to fast energy release by MGR.

The advantage of including turbulence is to bridge the gap between the short dissipation scale and the large-scale of the MGR process [37]. The earliest investigation on how MGR is affected by turbulence was presented by [38], based on two-dimensional numerical simulation. Their results showed multiple X-point structures created simultaneously leading to fast reconnection rate. Later, Lazarian and Vishniac [39] developed a scaling theory of turbulent MGR based on the work done by [40] on strong Alfvénic turbulence. They discovered that the reconnection speed becomes independent of the ohmic resistivity and is determined by the magnetic field wandering induced by turbulence. The magnetic field wan-

dering proposed by Lazarian and Vishniac has been confirmed by $3D$ numerical simulation done by Kowal *et al.* [41]. Their basic results were as follows:

- The MGR rate is largely enhanced in the turbulent state, and the rate does not depend on the magnetic diffusivity due to collisions.
- It was also shown that the larger the magnitude of fluctuation imposed and the turbulence injection scale is, the larger the reconnection rate becomes.
- They suggested that several collisionless effects are irrelevant to the reconnection rate in the turbulent state.

The numerical simulation done by Servidio *et al.* [42] investigated turbulent reconnection using MHD with a periodic boundary condition at a high *Reynolds* number. They found that a large number of X-point structures with various sizes and energies are generated, and a reconnection occurs at each X-point. Again, using $2D$ direct numerical simulations with a periodic boundary condition, Loureiro *et al.* [43] investigated how noise can affect the reconnection process. They showed that the reconnection rate has a weak dependence on the *Lundquist* number in highly turbulent systems. Another approach in treating the turbulence is the plasmoid instability [44]. In such an approach, turbulent reconnection is self-generated in the system without using any pre-existing turbulence. The formation of multiple plasmoid effectively reduces the width of the reconnection region, and consequently contribute to a fast reconnection [45, 46]. The effective transport caused by the turbulent magnetic diffusivity and the turbulent viscosity affects the dynamics of the plasma. A different approach of treating turbulence was done by the authors of [47] who developed a turbulence model for MHD plasmas consisting of mean and turbulent field equations. The main statistical quantities in MHD turbulence equations are the turbulent energy and cross-helicity. Dynamics of mean field and turbulent quantities have to be simultaneously treated in a consistent manner [48]. The advantage of this approach

is to find a relation between the fluctuations and the mean field inhomogeneities in plasma systems of high *Reynolds* number [49].

1.7 Solar Coronal Heating

The very high-temperature of the solar corona was first observed using spectroscopical study in the late 19^{th} century, the so-called coronal "green line" at 530.3 nm. None of the known elements on Earth has matched the observed spectral line of the corona, and it was concluded that a new element, named coronium, was discovered [50]. Later on, it was proved by Edlén in 1939 [51] that the coronium line is found in the emission spectrum of highly ionized iron at temperatures ≈ 1 MK. This was the moment of birth of the coronal heating problem.

Various physical models have been come up shortly after the detection of the unexpected hot plasma in the solar corona. The temperature of the core of the Sun, about 15 Mk, is produced mainly by thermonuclear fusion. Cooling processes start taking place as the solar energy flows outwardly from the core, passing through radiation and convection zones, right to the solar surface. Minimum temperature ($\approx$ 4200 K) is observed at the top of the photosphere. However, instead of decreasing, the temperature goes up slowly to around 2×10^4 K in the chromosphere. In the narrow transition region, the temperature shows an eminent increase of its value ($\approx 10^5$ K) up to around 2 Mk in the corona (Figure 1.3). Having preserved this high temperature, the corona must compromise some sort of energy input. Otherwise, the corona would cool down on a minute-scale.

The corona loses each second a flux of energy of roughly 10^4 J/m^2 in active regions and 300 J/m^2 in the Sun [52]. Hence, an energy source must be provided in order to sustain these losses. It's quite recognized that the mechanical motions in the photosphere is the essential source of the energy [53]. Such motions allow the footpoints of coronal magnetic field lines to displace. Compared to Alfvén dis-

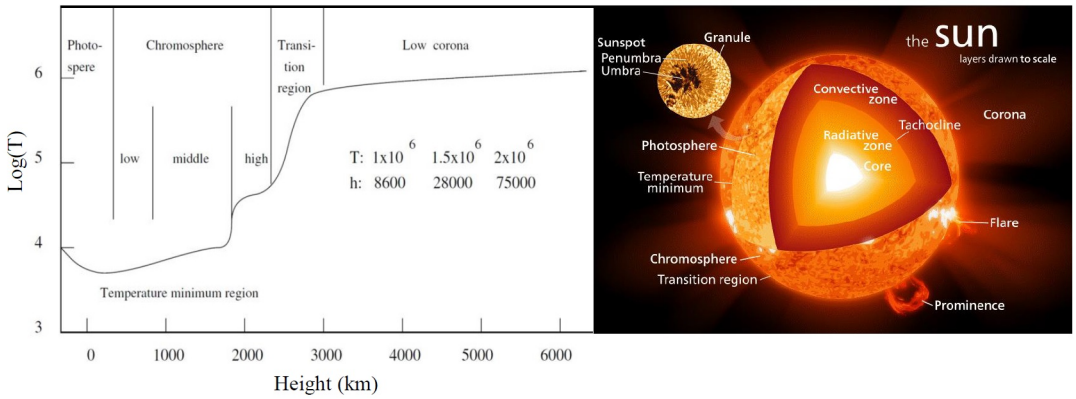

Figure 1.3: The variation of the temperature (on logarithmic scale) in the solar atmosphere as a function of the height measured in km.

placement time, long time-scale motions stress quasi-statically the magnetic field, whereas short time-scale motions generate waves. Dissipation of either magnetic stresses or waves heats the corona up. Processes of magnetic stress dissipation are referred to as direct current heating, and those of wave dissipation are referred to as alternating current heating.

Illustrations of solar corona heating is realized based on a couple of models providing diverse mechanisms that result in feeding the corona by additional heating. From an observational point of view, it is difficult to survey one heating mechanism alone because several mechanisms may operate at the same time [54]. We should rather predict the macroscopic outcome of a particular heating mechanism [55, 56, 57, 58] and confirm these signatures by observations [59]. The heating mechanisms in the solar atmosphere can be classified whether they involve magnetism or not. For magnetic-free regions (regions where plasma is weakly affected by magnetic fields) such as chromosphere of quiet Sun, one may suggest heating mechanisms in the framework of hydrodynamics (HD). Acoustic waves are examples of HD heating which provide shock dissipation processes [60]. It is accepted today that HD heating mechanisms still contribute but only at lower layers of the solar atmosphere [61]. However, the plasma of most parts of the solar atmosphere is strongly influenced by magnetic fields. In this case, the framework

of MHD may be the more relevant approach. The interest of magnetic fields is that they allow energy and magnetic stresses to channel from the inner solar bulk and surface to the higher atmosphere [62]. Heating in the MHD framework refers to MHD heating mechanisms [63, 64, 65, 66, 53]. Examples of the MHD heating mechanisms are the slow and fast MHD waves, Alfvén waves, current sheets, etc... . Joule heating plays an important role in the dissipation processes of these MHD models [54].

Converting the magnetic stress energy or wave energy into heat is an essential mechanism for coronal heating. Due to dissipation coefficients being highly small in the corona, significant heating seeks sharp gradients and very small spatial scales. Magnetic gradients and their associated electrical currents lead to heating by reconnection and ohmic dissipation, while velocity gradients lead to heating by viscous dissipation [53]. Compared to Alfvénic transit time, long characteristic time-scales of magnetic footpoint motions, that take place in the photosphere, will result in a magnetic tension along the field lines involving highly localized current sheets. These current sheets may release their energy through MGR process coupled with the fluctuations generated due to the photospheric footpoint motions.

Microphysics plays an important role in heating mechanisms via reconnection. In collisional plasma, resistivity would play a notable role in the reconnection process. As debated by Parker in 1973 [67] and verified with numerical simulations thereafter ([68] and others), that enhancement of electrical resistivity by 3 or more orders of magnitude allows the MGR to proceed at the fast Petschek rate. Moreover, as mentioned in [53], it was accepted by some modelers that artificial numerical resistivity of existing MHD codes captures the essential physical effects of the corona. However, several studies pointed out that MGR process needs plasma to be collisionless [31, 69]. The Hall term in the generalized Ohm's law forces ions to leave the magnetic field at a scale of the ion skin depth which is $\sim$ 10 m in the corona [70]. The interplay between large and small scales is

important for coronal heating and other interesting coronal problems. Thus, it is helpful to associate microphysics with MHD codes for better results. One example is to use the anomalous resistivity due to current-driven instability. This anomalous condition allows resistivity to depend on the ratio of the drift velocity of the electric current to the thermal velocity of the particles [71, 72, 73].
We have pointed out a little literature review about the solar coronal heating problem, and it still remains one of the most unresolved problems in Astrophysics. Small scales observations, improved numerical modeling and theoretical approaches should be pursued for better understanding the solar atmosphere. In the work done here, we are going to investigate the MGR with magnetic fluctuations, thought to be generated by the photospheric footpoint motions, as an effective process for the solar coronal heating.

1.8 Statement of the Problem

Extreme ultraviolet and X-ray observations of the Sun's outer layer indicate a sharp increase of the temperature from 10^4 K in the photosphere to more than 10^6 K in the corona (See Figure 1.3). Usually temperature gets reduced when moving away from a heat source. This is why the anomalous temperature observed in the corona denotes a major solar mystery namely the coronal heating problem.
Several mechanisms have been suggested to understand the process of coronal heating. All these mechanisms may operate simultaneously. For this sake, and since high resolution data are needed to realize the contribution of each individual mechanism in the solar coronal heating, NASA has launched the PSP which is the first-ever mission to touch the Sun. In this thesis, we are going to investigate the MGR process with magnetic fluctuations as one candidate which can enhance heating in the solar corona.
The role of the MGR in establishing the high temperature observed in the solar

corona is a fundamental question in astrophysical research. The solar layers, such as the photosphere, are highly turbulent. The coronal field lines are thought to be originated in the photosphere at sites called footpoints. The turbulent motion of the photospheric footpoints can easily produce fluctuations in the coronal magnetic field. Consequently, one way incorporating the effect of the photospheric turbulence is by adding fluctuations to the coronal magnetic field. Our approach assumes sinusoidal behavior of such fluctuations, and they are treated in the framework of resistive MHD using the Spitzer resistivity model. The contribution of the MGR process in the solar coronal heating is thus addressed in the scope of magnetic fluctuations generated by the turbulent motion of the photospheric footpoints, hence the thesis title: "Effects of Fluctuations on Magnetic Reconnection and heating in the Solar Corona".

1.9 Thesis Overview

This thesis is organized as follows:

- In Chapter 2, we discuss how the basic plasma equations are derived from the Vlasov equation. Next, we present two sets of equations along with the Maxwell's equations for the two-fluid plasma model. Then, after applying some useful assumptions, we conclude the one-fluid plasma approach, the MHD model. Finally, we introduce the equations of our model using the two-dimensional resistive MHD equations, modified by adding magnetic field fluctuations and the z-components of velocity and magnetic field.

- In Chapter 3, we discuss the methodology of space discretization using the finite volume approach. We present a proper way to discretize a conservation equation in one dimensional space. Then, we study the discretization process of the temporal term, and discuss the difference among three time schemes: explicit, implicit and Crank-Nicolson. Finally, the discretized

equations are transformed into a system of linear equations of the form $\mathbf{A}\phi = \mathbf{B}$, where ϕ's are the unknowns we seek. Such a system is solved using either direct or iterative methods.

- In Chapter 4, we present a brief literature about the numerical methods that have been proposed for solving the compressible and incompressible Euler and Navier-Stokes equations. We focus only on SIMPLE and PISO algorithms, which are pressure based algorithms, and they are used to guarantee the continuity equation. We also present the BPISO algorithm which uses the method of magnetic field projection, and it is used to reduce the divergence of the magnetic field. Then follows a discussion about the features of the openFOAM code, the code we use to solve our basic equations with the help of PISO and BPISO methods.

- In Chapter 5, we check out the validity of our MHD code using three test cases in the literature. Two cases are done to test the dynamics of the MHD flow with and without magnetic field. The third case is performed to test the ability of our code in handling the MGR process. The three test cases show good agreement with the literature.

- In Chapter 6, we assume sinusoidal fluctuations whose angular frequency and wavenumber are selected based on the observed time-scales of the photospheric footpoint motion. Then follows the simulation setup: the mesh size, the initial and boundary conditions. Finally in this chapter, we present and compare the results of three MGR cases, with and without fluctuations, using the Spitzer resistivity model with a zero initial velocity. The results show that the fluctuations contribute significantly to reconnection and heat processes of the solar corona.

- In Chapter 7, we perform two runs of new MGR cases applying the uniform resistivity model instead of the Spitzer one, with and without magnetic

fluctuations, using the same initial and boundary conditions and the same mesh as in Chapter 6. We find that the fast MGR process is not achieved when using uniform resistivity in the framework of resistive MHD model.

- In Chapter 8, we do two runs simulating other MGR cases, with and without fluctuations, using the same Spitzer-like resistivity form of Chapter 6 and starting with a non-zero initial velocity along the outflow direction. We present one part of the new results and remove the other part due to the presence of numerical instabilities near the boundaries. Reducing these numerical instabilities is related to the choice of the boundary conditions that are convenient with those cases, and this is left for future work.

- In Chapter 9, we summarize all what has been done in this thesis and we provide the conclusion of our work. Of course, this is not the end, a future work is also presented showing that our work can address many applications in astrophysical plasma systems and laboratory plasma devices as well.

Chapter 2

Plasma Modeling - Basic Equations

2.1 Introduction

A plasma is a complex system because the motion of the particles and the electromagnetic fields are interdependent. Understanding and modeling the dynamics of such a system is a challenging task. There are different approaches modeling the plasma behavior, but they can be broadly divided into two classes: microscopic modeling and macroscopic modeling [74].

Microscopic modeling considers the plasma behavior on the length-scale of the particles' orbits around the magnetic field lines, defined as the Larmor radius. For example, in tokamak plasma the ion Larmor radius is 10^{-3} m and the electron's is 10^{-5} m, while the ion Larmor radius in the solar corona plasma is few meters and that for electrons is few centimeters [8].

The other class is the macroscopic modeling, which considers the plasma behavior on the length-scale of the total plasma size by averaging over the smaller-scale behavior. The macroscopic models are used to further simplify the problem by making some additional physical assumptions about the plasma's behavior. In

the two-fluid treatment, the ions and electrons in the plasma are modeled as fluids, each described by a number of macroscopic parameters including density, pressure and mean fluid velocity at each point in the plasma. The evolution of these quantities is described by a set of equations obtained by averaging over the equations that describe the kinetic model. Magnetohydrodynamics (MHD) is a further simplification of the two-fluid model in which the ion and electron fluids are combined as a single fluid. The main approximations made in the MHD model is to neglect the mass of the electrons compared to the ion mass, and to apply the quasi-neutrality condition namely $n_i \approx n_e$. Those approximations are satisfied for the plasmas used in contemporary tokamak fusion experiments as well as in many solar activities such as solar flares and geomagnetic storms [5].
In what follows, we present the two-fluid plasma model in which electrons and ions are considered as two separate fluids interacting together with the electromagnetic fields. The electron and ion equations are all derived from the famous Vlasov equation. A little review of such equation is useful to understand where the fundamental plasma equations are coming from. Since we are dealing with charged species, the Maxwell's equations for the electromagnetic fields $\vec{E}$ and $\vec{B}$ are also introduced. Further, having applied some useful assumptions, we can easily recover the MHD model from the two-fluid model. Finally, we present the equations of our model using the two-dimensional resistive MHD equations.

2.2 The Vlasov Equation

The Vlasov equation is a differential equation describing time evolution of the distribution function of plasma consisting of charged particles with long-range (for example, Coulomb) interaction. In what follows, we want to show the derivation of the Vlasov equation.
The phase space is a six-dimensional space whose a volume element is $\mathrm{d}^3v\mathrm{d}^3x$, where v and x refer to speed and position respectively. The distribution function

representing the number density of particles n found in the vicinity of a point in the six-dimensional phase space is $f(\vec{x}, \vec{v}, t)$, where $\vec{x}$ and $\vec{v}$ denote the three-dimensional vectors of position and velocity respectively.
Having been averaged over the velocity space, the number density of particles in physical space is given simply by

$$n(\vec{x}, t) = \int f(\vec{x}, \vec{v}, t) \mathrm{d}^3 v.$$

The number of particles located within a volume element $\mathrm{d}^3 x$ in physical space and having velocities lying within a volume element $\mathrm{d}^3 v$ in velocity space is defined as $\mathrm{d}N = f(\vec{x}, \vec{v}, t) \mathrm{d}^3 v \mathrm{d}^3 x$. Thus, the number of particles N in a volume of phase space is given by:

$$N = \int f(\vec{x}, \vec{v}, t) \mathrm{d}^3 v \mathrm{d}^3 x.$$

Conservation of the number of particles requires that the total time derivative of N must vanish, where the "total" time derivative means that we allow the boundary surface to move with the particles that lie on it:

$$0 = \frac{\mathrm{d}N}{\mathrm{d}t} = \int \left(\frac{\partial f}{\partial t} + \vec{\nabla}.\big(f\vec{U}\big) \right) \mathrm{d}^3 v \mathrm{d}^3 x. \tag{2.1}$$

Here, $\vec{\nabla}$ denotes a six-component divergence operator, whose components are $(\vec{\nabla}_x, \vec{\nabla}_v)$ and $\vec{U}$ denotes a six-dimensional vector in phase space. Since Equation (2.1) must hold for every volume element in phase space, we must have

$$\frac{\partial f}{\partial t} + \vec{\nabla}.\big(f\vec{U}\big) = 0. \tag{2.2}$$

It is necessary to keep in mind that the components of $\vec{U}$ are $\left(\dot{\vec{x}}, \dot{\vec{v}}\right) = \left(\vec{v}, \frac{\vec{F}}{m}\right)$. The divergence of $\vec{U}$ is then written as

$$\vec{\nabla}.\vec{U} = \vec{\nabla}_x.\vec{U} + \vec{\nabla}_v.\vec{U} = \vec{\nabla}_x.\vec{v} + \vec{\nabla}_v.\left(\frac{\vec{F}}{m}\right) = 0,$$

and this is true for $\vec{F}$ independent of $\vec{v}$ such as electric and gravitational forces. Now we can rewrite Equation (2.2) as

$$\frac{\partial f}{\partial t} + \vec{v}.\vec{\nabla} f + \frac{\vec{F}}{m}.\frac{\partial f}{\partial \vec{v}} = 0,$$

where $\vec{\nabla}$ here represents our familiar gradient:

$$\vec{\nabla} = \frac{\partial}{\partial x}\hat{x} + \frac{\partial}{\partial y}\hat{y} + \frac{\partial}{\partial z}\hat{z}.$$

We may now give our final result, the Vlasov equation, for the case of plasma whose particles are acted upon by electric and magnetic forces, the so-called the *Lorentz* force

$$\vec{F} = q(\vec{E} + \vec{v} \times \vec{B}),$$

as

$$\frac{\partial f}{\partial t} + \vec{v}.\vec{\nabla} f + \frac{q}{m}(\vec{E} + \vec{v} \times \vec{B}).\frac{\partial f}{\partial \vec{v}} = 0, \tag{2.3}$$

where $\vec{E}$ and $\vec{B}$ represent the electromagnetic fields.

2.3 The Moments Equations

The full plasma equations are all derived from the Vlasov equation. They can be obtained by integrating Equation (2.3) over velocity space [75]. If we consider the entire plasma system as a single fluid medium, the following integrations are useful in obtaining the one-fluid plasma equations.

- $\int$(Eq. 2.3)d^3v yields the zeroth-order moment or the continuity equation.
- $\int m\vec{v}$(Eq. 2.3)d^3v yields the first-order moment or the momentum balance equation.
- $\int \frac{1}{2}mv^2$(Eq. 2.3)d^3v yields the second-order moment or the energy equation.

2.3.1 Zeroth-Order Moment: The Continuity Equation

In order to derive the continuity equation, we have to integrate the Vlasov equation, Equation (2.3), over the velocity space, i.e.

$$\underbrace{\int \frac{\partial f}{\partial t} \mathrm{d}^3 v}_{①} + \underbrace{\int \vec{v}.\vec{\nabla} f \mathrm{d}^3 v}_{②} + \underbrace{\int \frac{q}{m}(\vec{E} + \vec{v} \times \vec{B}).\frac{\partial f}{\partial \vec{v}} \mathrm{d}^3 v}_{③} = 0. \tag{2.4}$$

The first two terms are straightforwardly evaluated as follows:

$$① \text{ gives } \frac{\partial}{\partial t}\Big(\int f \mathrm{d}^3 v \Big) = \frac{\partial n}{\partial t} \qquad \text{and} \qquad ② \text{ gives } \vec{\nabla}.\Big(\int \vec{v} f \mathrm{d}^3 v \Big) = \vec{\nabla}. < n\vec{v} >,$$

where the operator <> represents the average value over the velocity space. Let us define the average velocity to be $\vec{u}$, such that $< \vec{v} >= \vec{u}$. Thus, the second term becomes

$$② = \vec{\nabla}. < n\vec{v} > = \vec{\nabla}.(n\vec{u}).$$

Concerning the last term we have to divide it into two sub-terms: ③ $\Longrightarrow$

$$\int \frac{q}{m}(\vec{E} + \vec{v} \times \vec{B}).\frac{\partial f}{\partial \vec{v}} \mathrm{d}^3 v = \frac{q}{m} \underbrace{\int \vec{E}.\frac{\partial f}{\partial \vec{v}} \mathrm{d}^3 v}_{③a} + \frac{q}{m} \underbrace{\int (\vec{v} \times \vec{B}).\frac{\partial f}{\partial \vec{v}} \mathrm{d}^3 v}_{③b}. \tag{2.5}$$

By using the Gauss' divergence theorem in velocity space, we can write ③a as

$$\int_{-\infty}^{+\infty} \vec{E}.\frac{\partial f}{\partial \vec{v}} \mathrm{d}^3 v = \int_{-\infty}^{+\infty} \frac{\partial}{\partial \vec{v}}.(f\vec{E}) \mathrm{d}^3 v = \int_{-\infty}^{+\infty} (f\vec{E}).d\vec{S} = 0.$$

Note that the surface area S in velocity space goes as v^2 and the distribution function f goes as e^{-v^2} (we assume here a Maxwellian distribution), so as $v \longrightarrow \infty$; $f \longrightarrow 0$ more quickly than $S \longrightarrow \infty$.

Having used the Gauss' divergence theorem in velocity space again and the fact that the term $\frac{\partial}{\partial \vec{v}}.(\vec{v} \times \vec{B})$ vanishes, we can deduce the following

$$\textcircled{3b} = \int_{-\infty}^{+\infty} \frac{\partial}{\partial \vec{v}}.[f(\vec{v} \times \vec{B})]\mathrm{d}^3v - \int_{-\infty}^{+\infty} f \frac{\partial}{\partial \vec{v}}.(\vec{v} \times \vec{B}) = 0.$$

The summation of ①, ② and ③ together gives the zeroth-order moment or simply the continuity equation for particle density n, and it is written as

$$\frac{\partial n}{\partial t} + \vec{\nabla}.(n\vec{u}) = 0. \tag{2.6}$$

Let us define further the mass density $\rho = mn$ for a single-fluid plasma. The continuity equation for the mass density is thus determined by multiplying Equation (2.6) by the mass m and it is given as follows

$$\frac{\partial \rho}{\partial t} + \vec{\nabla}.(\rho\vec{u}) = 0. \tag{2.7}$$

2.3.2 First-Order Moment: The Momentum Balance Equation

The first-order moment or simply the momentum balance equation is obtained by multiplying the Vlasov equation, Equation (2.3), by $m\vec{v}$ and integrating over the velocity space,

$$\underbrace{\int m\vec{v}\frac{\partial f}{\partial t}\mathrm{d}^3v}_{①} + \underbrace{\int m\vec{v}(\vec{v}.\vec{\nabla}f)\mathrm{d}^3v}_{②} + \underbrace{q\int \vec{v}(\vec{E} + \vec{v} \times \vec{B}).\frac{\partial f}{\partial \vec{v}}\mathrm{d}^3v}_{③} = \vec{0}. \tag{2.8}$$

- Evaluating ①:

$$\int m\vec{v}\frac{\partial f}{\partial t}\mathrm{d}^3v = m\frac{\partial}{\partial t}\int (\vec{v}f)\mathrm{d}^3v = m\frac{\partial(n\vec{u})}{\partial t}.$$

- Evaluating ②:

$$\int m\vec{v}(\vec{v}.\vec{\nabla}f)\mathrm{d}^3v = m\vec{\nabla}.\int(f\vec{v}\vec{v})\mathrm{d}^3v = m\vec{\nabla}.(<n\vec{v}\vec{v}>).$$

Let us now separate the velocity $\vec{v}$ into the average fluid velocity $\vec{u}$ and a thermal velocity $\vec{w}$, such that $\vec{v} = \vec{u} + \vec{w}$. So we can expand now $<\vec{v}\vec{v}>$ as

$$<\vec{v}\vec{v}>=<\vec{u}\vec{u}>+<\vec{w}\vec{w}>+<\vec{u}\vec{w}>+<\vec{w}\vec{u}>.$$

Since $<\vec{u}>=\vec{u}$ (average velocity) and $<\vec{w}>=0$ (thermal velocity), so we have

$$<\vec{u}\vec{u}>=\vec{u}\vec{u} \qquad \text{and} \qquad <\vec{u}\vec{w}>=\vec{u}<\vec{w}>=<\vec{w}>\vec{u}=0.$$

Therefore, we can write

$$m\vec{\nabla}.(<n\vec{v}\vec{v}>) = m\vec{\nabla}.(n\vec{u}\vec{u}) + m\vec{\nabla}.(<n\vec{w}\vec{w}>).$$

Define the pressure or stress tensor to be:

$$P = m<n\vec{w}\vec{w}>,$$

thus we end up with: $\qquad (2) = m\vec{\nabla}.(<n\vec{v}\vec{v}>) = m\vec{\nabla}.(n\vec{u}\vec{u}) + \vec{\nabla}.P.$

- Evaluating (3):

It is easy to show that: $\quad \vec{v}(\vec{E}+\vec{v}\times\vec{B}).\frac{\partial f}{\partial\vec{v}} = \frac{\partial}{\partial\vec{v}}.[f\vec{v}(\vec{E}+\vec{v}\times\vec{B})] - f[(\vec{E}+\vec{v}\times\vec{B})].$

So $\qquad (3) = q\int_{-\infty}^{+\infty}\frac{\partial}{\partial\vec{v}}.[f\vec{v}(\vec{E}+\vec{v}\times\vec{B})]\mathrm{d}^3v - q\int_{-\infty}^{+\infty}f\vec{E}\mathrm{d}^3v - q\int_{-\infty}^{+\infty}f(\vec{v}\times\vec{B})\mathrm{d}^3v,$

$$= q\int_{-\infty}^{+\infty}[f\vec{v}(\vec{E}+\vec{v}\times\vec{B})].\vec{dS} - qn\vec{E} - qn\vec{u}\times\vec{B} = \vec{0} - qn(\vec{E}+\vec{u}\times\vec{B}).$$

The summation of (1), (2) and (3) together gives the first-order moment or simply the momentum balance equation, and it is written as

$$\frac{\partial(mn\vec{u})}{\partial t} + \vec{\nabla}.(mn\vec{u}\vec{u}) = -\vec{\nabla}.P + nq(\vec{E}+\vec{u}\times\vec{B}). \tag{2.9}$$

Finally, the momentum balance equation in terms of the mass density ρ is thus given as follows

$$\frac{\partial(\rho\vec{u})}{\partial t} + \vec{\nabla}.(\rho\vec{u}\vec{u}) = -\vec{\nabla}.P + nq(\vec{E} + \vec{u} \times \vec{B}). \tag{2.10}$$

2.3.3 Second-Order Moment: The Energy Equation

In a similar way to the momentum equation, the energy equation is obtained by multiplying the Vlasov equation by $\frac{1}{2}mv^2$ ($v^2 = \vec{v}.\vec{v}$) and then integrating it over the velocity space. The new equation is

$$\underbrace{\int \frac{1}{2}mv^2 \frac{\partial f}{\partial t} \mathrm{d}^3v}_{①} + \underbrace{\int \frac{1}{2}mv^2(\vec{v}.\vec{\nabla}f)\mathrm{d}^3v}_{②} + q\underbrace{\int \frac{1}{2}v^2(\vec{E} + \vec{v} \times \vec{B}).\frac{\partial f}{\partial \vec{v}}\mathrm{d}^3v}_{③} = 0. \tag{2.11}$$

- Evaluating ①:

$$\int \frac{1}{2}mv^2 \frac{\partial f}{\partial t}\mathrm{d}^3v = \frac{\partial}{\partial t}\int (\frac{1}{2}mv^2 f)\mathrm{d}^3v = \frac{\partial}{\partial t}\Big(\frac{1}{2}m < n\vec{v}^2 > \Big).$$

Let us expand again the velocity $\vec{v}$ in terms of $\vec{u}$ and $\vec{w}$, we thus have

$$\vec{v}^2 = \vec{u}^2 + \vec{w}^2 + 2\vec{u}.\vec{w}.$$

Using the fact that $< \vec{w} >= \vec{0}$ and $< \vec{w}^2 >= Trace(P)$, the first term yields

$$① = \frac{\partial}{\partial t}\Big(\frac{1}{2}mnu^2 + \frac{3}{2}p\Big),$$

where p is the scalar thermal pressure considering the pressure tensor P to be isotropic in all directions.

- Evaluating ②:

It is not straightforward to do the derivation of the second term. In what follows, we show only a simplification, and if you are interested for more details, please visit Section 7.1 of [76] and Chapter 3 of [77]. Anyway, the second term can be expressed as

$$② = \int \tfrac{1}{2}mv^2(\vec{v}.\vec{\nabla}f)\mathrm{d}^3v = \vec{\nabla}.\int(\tfrac{1}{2}mv^2\vec{v}f)\mathrm{d}^3v = \vec{\nabla}.\Big(\tfrac{1}{2}mnu^2 + \tfrac{3}{2}p\Big)\vec{u} + \vec{\nabla}.\Big(P\vec{u}\Big).$$

- Evaluating ③:

It is easy to show that ③ can be written as

$$\int \frac{1}{2}v^2(\vec{E} + \vec{v} \times \vec{B}).\frac{\partial f}{\partial \vec{v}}\mathrm{d}^3v = \int \frac{1}{2}v^2\frac{\partial}{\partial \vec{v}}.\Big[\big(\vec{E} + \vec{v} \times \vec{B}\big)f\Big]\mathrm{d}^3v. \tag{2.12}$$

There are 9 terms in the integration of Equation (2.12), in which six of them are in the following form:

$$\begin{aligned}\int\int\int \frac{1}{2}v_x^2\frac{\partial}{\partial v_y}\big(E_y f\big)\mathrm{d}^3v &= \frac{1}{2}\int\int v_x^2\Big[\int \frac{\partial}{\partial v_y}\big(E_y f\big)\mathrm{d}v_y\Big]\mathrm{d}^2v \\ &= \frac{1}{2}\int\int v_x^2 E_y\big[f\big]_{v_y=-\infty}^{v_y=+\infty}\mathrm{d}^2v \\ &= 0,\end{aligned} \tag{2.13}$$

and the rest three terms of Equation (2.12) are in the following form:

$$\begin{aligned}\int\int\int \frac{1}{2}v_x^2\frac{\partial}{\partial v_x}\big(E_x f\big)\mathrm{d}^3v &= \frac{1}{2}\int\int\Big[\int v_x^2\frac{\partial}{\partial v_x}\big(E_x f\big)\mathrm{d}v_x\Big]\mathrm{d}^2v \\ &= \frac{1}{2}\int\int E_x\big[v_x^2 f\big]_{v_x=-\infty}^{v_x=+\infty}\mathrm{d}^2v - \frac{1}{2}\int\int\int 2E_x v_x f\mathrm{d}v_x\mathrm{d}^2v \\ &= 0 - E_x u_x n.\end{aligned} \tag{2.14}$$

Therefore, $\textcircled{3} = -nq(E_x u_x + E_y u_y + E_z u_z) = -nq\big(\vec{E}.\vec{u}\big).$

The summation of $\textcircled{1}$, $\textcircled{2}$ and $\textcircled{3}$ together gives the second-order moment or simply the energy equation

$$\frac{\partial}{\partial t}\Big(\frac{1}{2}mnu^2 + \frac{3}{2}p\Big) + \vec{\nabla}.\Big(\frac{1}{2}mnu^2 + \frac{3}{2}p\Big)\vec{u} = -\vec{\nabla}.\Big(P\vec{u}\Big) + nq\big(\vec{E}.\vec{u}\big). \tag{2.15}$$

Note that Equation (2.15) represents the hydrodynamic (kinetic + internal) energy equation. The kinetic energy equation is obtained by making the scalar product of $\vec{u}$ (the average fluid velocity) with the momentum equation, Equation (2.9). This equation is thus given as follows

$$\frac{\partial}{\partial t}\big(\frac{1}{2}mnu^2\big) + \vec{\nabla}.\big(\frac{1}{2}mnu^2\big)\vec{u} = -\vec{u}.\big(\vec{\nabla}.P\big) + nq\big(\vec{E}.\vec{u}\big). \tag{2.16}$$

In order to get the internal energy equation alone, we have to subtract the kinetic energy equation from the hydrodynamic energy equation, i.e. Equation (2.15) − Equation (2.16), which yields

$$\frac{\partial}{\partial t}\big(\frac{3}{2}p\big) + \vec{\nabla}.\big(\frac{3}{2}p\big)\vec{u} = -P\vec{\nabla}.\vec{u}. \tag{2.17}$$

Let us further assume that the plasma gas is ideal and monoatomic, and the pressure tensor P is reduced to the thermal pressure p, which is a scalar quantity. The thermal pressure p is thus written in terms of the internal energy per unit mass ε as

$$p = \frac{2}{3}mn\varepsilon = \big(\frac{5}{3} - 1\big)mn\varepsilon = (\gamma - 1)\rho\varepsilon, \tag{2.18}$$

where γ $(= 5/3)$ is the ratio of the specific heats, and $\rho = mn$ is again the plasma mass density. Equation (2.18) is known as the equation of state and it is needed to close any system of fluid equations. Finally, the internal energy equation is

thus written as

$$\frac{\partial(\rho\varepsilon)}{\partial t} + \vec{\nabla}.\big(\rho\vec{u}\varepsilon\big) = -p\vec{\nabla}.\vec{u}. \tag{2.19}$$

2.4 The Two-Fluid Plasma Model

Equations. (2.7, 2.10, 2.19) are derived for one species-fluid. In the two-fluid plasma approach, we have to take into consideration both electrons and ions as two separate fluids. The evolution of the particle densities of the ions and electrons are expressed by the continuity equations

$$\frac{\partial\rho_i}{\partial t} + \vec{\nabla}.(\rho_i\vec{u_i}) = 0, \tag{2.20}$$

$$\frac{\partial\rho_e}{\partial t} + \vec{\nabla}.(\rho_e\vec{u_e}) = 0, \tag{2.21}$$

where ρ_i/ρ_e are the ion/electron mass densities and $\vec{u_i}/\vec{u_e}$ are the ion/electron fluid velocities.

The Vlasov equation, Equation (2.3) also called the collisionless Boltzmann equation, was derived for collisionless particles. However, if collision between particles takes place, extra terms should be added on the right hand side of Equation (2.3), and the obtained equation is the famous Boltzmann equation. One important term is the momentum transfer $\vec{R}$ between particles due to collisions. Thus, the first moment of the Vlasov equation, including the effect of momentum transfer, yields the momentum equation for each species

$$\frac{\partial(\rho_i\vec{u_i})}{\partial t} + \vec{\nabla}.(\rho_i\vec{u_i}\vec{u_i}) = -\vec{\nabla}p_i + n_ie(\vec{E} + \vec{u_i}\times\vec{B}) + \vec{R_i}, \tag{2.22}$$

$$\frac{\partial(\rho_e\vec{u_e})}{\partial t} + \vec{\nabla}.(\rho_e\vec{u_e}\vec{u_e}) = -\vec{\nabla}p_e - n_ee(\vec{E} + \vec{u_e}\times\vec{B}) + \vec{R_e}, \tag{2.23}$$

where p_i/p_e are the ion/electron thermal pressures, and e is the elementary charge. $\vec{E}$ is the electric field, and $\vec{B}$ is the magnetic field. $\vec{R_i}$ and $\vec{R_e}$ are the momentum transfers between electrons and ions, and for a good approximation it can be

assumed that $\vec{R_i} = -\vec{R_e}$.

The second moment of the Vlasov equation yields internal energy equations for each species

$$\frac{\partial(\rho_i \varepsilon_i)}{\partial t} + \vec{\nabla}.\big(\rho_i \vec{u_i} \varepsilon_i\big) = -p_i \vec{\nabla}.\vec{u_i} + Q_i, \tag{2.24}$$

$$\frac{\partial(\rho_e \varepsilon_e)}{\partial t} + \vec{\nabla}.\big(\rho_e \vec{u_e} \varepsilon_e\big) = -p_e \vec{\nabla}.\vec{u_e} + Q_e, \tag{2.25}$$

where Q_i/Q_e are the ion/electron generated heat associated with resistivity, and they are arisen from the collision terms on the right hand side of Equation (2.3). In other words, Q_i is the heat transferred to the ions due to collisions with the electrons, and Q_e is the heat transferred to the electrons due to collisions with the ions.

2.5 The Maxwell's Equations

As mentioned before, electrons and ions are also governed by the electromagnetic fields $\vec{E}$ and $\vec{B}$, since they are charged particles. By combining the electric field $\vec{E}$ and the magnetic field $\vec{B}$ to the fluid, we have to survey other equations which describe their behavior. Those equations are the famous Maxwell's equations [78], and they are given as follows

$$\frac{1}{c^2}\frac{\partial \vec{E}}{\partial t} + \mu_0 \vec{J} = \vec{\nabla} \times \vec{B}, \tag{2.26}$$

$$\frac{\partial \vec{B}}{\partial t} + \vec{\nabla} \times \vec{E} = \vec{0}, \tag{2.27}$$

$$\vec{\nabla}.\vec{E} = \frac{\rho_c}{\varepsilon_0}, \tag{2.28}$$

$$\vec{\nabla}.\vec{B} = 0, \tag{2.29}$$

where c is the speed of light. ε_0 and μ_0 are respectively the permittivity and the permeability of vacuum, such that $\varepsilon_0 \mu_0 = 1/c^2$. $\vec{J} = e(n_i \vec{u_i} - n_e \vec{u_e})$ is the

current density, where e is the elementary charge. $\rho_c = e(n_i - n_e)$ is the charge density. The first two equations, Equations (2.26) and (2.27), are respectively the Ampère's law and the Faraday's law. The last two equations, Equations (2.28) and (2.29), represent two constraints for the electromagnetic fields $\vec{E}$ and $\vec{B}$.

2.6 MHD Model

2.6.1 The Fluid Equations

In order to derive the continuity, the momentum, and the energy equations of the MHD model, we consider the simplest plasma of fully ionized hydrogen. The mass of the electron is neglected relative to that of the ion ($m_i \approx 1836 m_e$). Usually quasi-neutrality condition is applied for such a plasma namely $n_e \approx n_i$, which in turn leads to vanish the charge density ($\rho_c \approx 0$), and allows us to write the current density as $\vec{J} \approx n_i e(\vec{u_i} - \vec{u_e})$. We introduce the mass m, the particle density n, the mass density ρ, the mean velocity $\vec{u}$, and the thermal pressure p_{th} in the single-fluid (MHD) description as

- $m = m_i + m_e = m_i(1 + \frac{m_e}{m_i}) \approx m_i$,
- $n = \frac{m_i n_i + m_e n_e}{m_i + m_e} \approx n_i \approx n_e$,
- $\rho = \rho_i + \rho_e = m_i n_i + m_e n_e \approx n m_i(1 + \frac{m_e}{m_i}) \approx nm$,
- $\vec{u} = \frac{\rho_i \vec{u_i} + \rho_e \vec{u_e}}{\rho_i + \rho_e} \approx \vec{u_i}$,
- $p_{th} = p_i + p_e$.

By summing up the two continuity equations, Equations (2.20) and (2.21), and exploiting the definitions of ρ and $\vec{u}$, we get the continuity equation for the MHD model,

$$\frac{\partial \rho}{\partial t} + \vec{\nabla}.(\rho \vec{u}) = 0. \tag{2.30}$$

Now, if we sum up the two momentum equations, Equations (2.22) and (2.23), and exploit the definitions of ρ, $\vec{u}$, the current density $\vec{J}$ and the thermal pressure p_{th}, we get the momentum equation for the MHD model,

$$\frac{\partial(\rho\vec{u})}{\partial t} + \vec{\nabla}.(\rho\vec{u}\vec{u}) = -\vec{\nabla}p_{th} + \vec{J} \times \vec{B}. \tag{2.31}$$

Note that all terms that are proportional to the electron inertia are omitted. Furthermore, before presenting the energy equation of the MHD model and to close the full set of the MHD equations, an equation for the current density is needed. For negligible displacement currents, we simply use the Ampère's law in the MHD limit ($u << c$) and $\vec{B}$ as a dynamic variable. In other words, we use the Faraday's law (Equation 2.27) as it is and get the current density from the Ampère's law (Equation 2.26) as

$$\vec{J} = \frac{1}{\mu_0}\vec{\nabla} \times \vec{B}. \tag{2.32}$$

By using Equation (2.32), we can expand the last term on the right hand side of Equation (2.31) as

$$\vec{J} \times \vec{B} = -\vec{\nabla}\big(\frac{B^2}{2\mu_0}\big) + \frac{1}{\mu_0}\vec{\nabla}.(\vec{B}\vec{B}) - \frac{1}{\mu_0}\vec{B}\vec{\nabla}.\vec{B}. \tag{2.33}$$

The momentum equation thus becomes

$$\frac{\partial(\rho\vec{u})}{\partial t} + \vec{\nabla}.(\rho\vec{u}\vec{u}) = -\vec{\nabla}\big(p_{th} + \frac{B^2}{2\mu_0}\big) + \frac{1}{\mu_0}\vec{\nabla}.(\vec{B}\vec{B}) - \frac{1}{\mu_0}\vec{B}\vec{\nabla}.\vec{B}. \tag{2.34}$$

Similarly, following the same procedure by summing up the two energy equations, Equations (2.24) and (2.25), we get the energy equation for the MHD model,

$$\frac{\partial(\rho\varepsilon)}{\partial t} + \vec{\nabla}.\big(\rho\vec{u}\varepsilon\big) = -p_{th}\vec{\nabla}.\vec{u} + Q_i + Q_e. \tag{2.35}$$

For a good approximation as given in Chapter II of [79], we can express the full generated heat due to collisions between electrons and ions in terms of the resistivity η as

$$Q_e + Q_i \approx \eta |\vec{J}|^2,$$

where $\eta|\vec{J}|^2 (= \eta J^2)$ is also referred to as the Joule heating term. Thus, the final form of the internal energy equation is

$$\frac{\partial(\rho\varepsilon)}{\partial t} + \vec{\nabla}.\big(\rho\vec{u}\varepsilon\big) = -p_{th}\vec{\nabla}.\vec{u} + \eta J^2. \tag{2.36}$$

2.6.2 The Ohm's Law

To this stage, we still need an equation for the electric field $\vec{E}$, and this can be done using the Ohm's law. The full derivation of Ohm's law is not straightforward. However, the easiest way to derive it is to use the momentum balance equation for electrons, Equation (2.23). By neglecting the left hand side due to the electron inertia, Equation (2.23) becomes

$$\vec{0} = -\vec{\nabla} p_e - ne(\vec{E} + \vec{u_e} \times \vec{B}) + \vec{R}. \tag{2.37}$$

If we solve for the electric field $\vec{E}$, we get

$$\vec{E} = -\frac{1}{ne}\vec{\nabla} p_e - \vec{u_e} \times \vec{B} + \frac{1}{ne}\vec{R}. \tag{2.38}$$

Moreover, by using the quasi-neutrality condition, the electron velocity can be written as $\vec{u_e} = \vec{u} - \frac{1}{ne}\vec{J}$, and the fluid bulk velocity is $\vec{u_i} = \vec{u}$. Additionally, by considering plasma particles to be collisional, the ion-electron collision term $\vec{R}$ with frequency ν_{ei} is assumed to be proportional to the velocity difference, $\vec{R} = m_e n \nu_{ei}(\vec{u_i} - \vec{u_e})$ [80]. The resistivity for such a collisional plasma is defined

as $\eta = \frac{m_e \nu_{ei}}{ne^2}$ [80]. The collisional term $\vec{R}$ is thus written in terms of η as

$$\vec{R} = ne\eta\vec{J}. \tag{2.39}$$

Finally, the generalized form of Ohm's law is

$$\vec{E} + \vec{u} \times \vec{B} = \eta\vec{J} + \frac{1}{ne}\vec{J} \times \vec{B} - \frac{1}{ne}\vec{\nabla}p_e, \tag{2.40}$$

where the first term on the right hand side is the resistive term, the second is the Hall term, and the third is the electron pressure term. The Hall and the electron pressure terms introduce new physics into the system at short length-scales. They enter in at the ion inertial length (ion skin depth) which is the characteristic length-scale for ions to be accelerated by electromagnetic forces in a plasma. In the solar corona for particle density 10^{15} m^{-3}, the inertial length is ~ 7 m [8]. Thus, for large length-scales such as a current sheet width of roughly 100 km, the resistive term dominates all other terms on the right hand side. We then end up with the reduced Ohm's law given by

$$\vec{E} + \vec{u} \times \vec{B} = \eta\vec{J}. \tag{2.41}$$

2.6.3 The Induction Equation

Usually in MHD calculations, it is useful to make coupling among the Faraday's law (Equation 2.27), the reduced Ampère's law (Equation 2.32) and the reduced Ohm's law (Equation 2.41). The resulted equation is the so called "induction" equation, and it governs the time and space evolution of the magnetic field $\vec{B}$ coupled with the plasma velocity $\vec{u}$ and the resistivity η. As a first step in deriving this equation, by substituting the electric field of the reduced Ohm's law in the

Faraday's law, we get the basic form of the induction equation which reads

$$\frac{\partial \vec{B}}{\partial t} - \underbrace{\vec{\nabla} \times (\vec{u} \times \vec{B})}_{①} + \underbrace{\vec{\nabla} \times (\eta \vec{J})}_{②} = \vec{0}. \tag{2.42}$$

It is easy to show that $① = \vec{\nabla}.(\vec{B}\vec{u}) - \vec{\nabla}.(\vec{u}\vec{B})$. Concerning ②, we have to use the reduced Ampère's law and then do few calculation steps in order to get the final form of the induction equation. Thus, by using Equation (2.32), ② can be written as

$$\vec{\nabla} \times (\eta \vec{J}) = \frac{1}{\mu_0} \Big[\underbrace{\vec{\nabla}(\vec{B}.\vec{\nabla}\eta) + \vec{\nabla}.(\vec{\nabla}\eta\vec{B} - \vec{B}\vec{\nabla}\eta)}_{②a} - \underbrace{\vec{\nabla}^2(\eta\vec{B}) + \vec{\nabla}(\eta\vec{\nabla}.\vec{B})}_{②b} \Big]. \tag{2.43}$$

The second term of ②a can be written as follows

$$\vec{\nabla}.(\vec{\nabla}\eta\vec{B} - \vec{B}\vec{\nabla}\eta) = \hat{z} \times \vec{\nabla}\big[(\vec{\nabla}\eta \times \vec{B}).\hat{z}\big].$$

After doing some calculation steps, we find ②a equals to

$$②a = \vec{B}\vec{\nabla}^2\eta + \vec{\nabla}\eta.\vec{\nabla}\vec{B} - \big[\hat{z}.(\vec{\nabla}\eta \times \vec{\nabla}B_y)\big]\hat{x} + \big[\hat{z}.(\vec{\nabla}\eta \times \vec{\nabla}B_x)\big]\hat{y}, \tag{2.44}$$

where the last two terms of Equation (2.44) can easily be shown to be vanished according to the following

$$\begin{aligned} -\big[\hat{z}.(\vec{\nabla}\eta \times \vec{\nabla}B_y)\big]\hat{x} + \big[\hat{z}.(\vec{\nabla}\eta \times \vec{\nabla}B_x)\big]\hat{y} &= -\hat{z}.\vec{\nabla} \times \big[\eta\vec{\nabla}(\vec{B} \times \hat{z})\big] \\ &= -\vec{\nabla} \times \Big[\eta\vec{\nabla}\big[(\vec{B} \times \hat{z}).\hat{z}\big]\Big] = \vec{0}. \end{aligned}$$

Thus, the term (2) of Equation (2.42) is now written as

$$\begin{aligned}\vec{\nabla}\times(\eta\vec{J}) &= \frac{1}{\mu_0}\big[\vec{B}\vec{\nabla}^2\eta+\vec{\nabla}\eta.\vec{\nabla}\vec{B}-\vec{\nabla}^2(\eta\vec{B})+\vec{\nabla}(\eta\vec{\nabla}.\vec{B})\big] \\ &= \frac{1}{\mu_0}\big[-\vec{\nabla}.(\eta\vec{\nabla}\vec{B})+\vec{\nabla}(\eta\vec{\nabla}.\vec{B})\big].\end{aligned} \tag{2.45}$$

Finally, the induction equation can be written in its final form as

$$\frac{\partial\vec{B}}{\partial t}+\vec{\nabla}.(\vec{u}\vec{B})-\vec{\nabla}.\big(\frac{\eta}{\mu_0}\vec{\nabla}\vec{B}\big)=\vec{\nabla}.(\vec{B}\vec{u})-\vec{\nabla}\big(\frac{\eta}{\mu_0}\vec{\nabla}.\vec{B}\big). \tag{2.46}$$

2.6.4 The Total Energy Equation

The total energy per unit mass is $E_{total}=\varepsilon+E_k+E_{mag}$, where ε, E_k and E_{mag} are respectively the internal, kinetic and magnetic energy per unit mass. The equation for ε is given above by Equation (2.36). The equations for E_k and E_{mag} are obtained by making the scalar product of $\vec{u}$ and $\mu_0^{-1}\vec{B}$ respectively with the momentum equation of the MHD model and the Faraday's law, i.e. Equation (2.31) and Equation (2.27), where the electric field $\vec{E}$ is determined according to the reduced Ohm's law, i.e. Equation (2.41). In what follows, we derive the kinetic and the magnetic energy equations separately, and then we add them up along with the internal energy equation in order to get the total energy equation.

By making the dot product of $\vec{u}$ with Equation (2.31), we obtain the kinetic energy equation,

$$\frac{\partial(\rho E_k)}{\partial t}+\vec{\nabla}.(\rho\vec{u}E_k)=-\vec{u}.\vec{\nabla}p_{th}+\vec{u}.(\vec{J}\times\vec{B}), \tag{2.47}$$

where $\rho E_k=\rho u^2/2$ is the kinetic energy density.

The magnetic energy equation is not straightforward, and it is obtained by doing few calculation steps. Let us start by making the scalar product of $\mu_0^{-1}\vec{B}$ with

Equation (2.27), and this yields the following equation

$$\frac{\partial(\rho E_{mag})}{\partial t} + \frac{\vec{B}}{\mu_0}.\vec{\nabla} \times \vec{E} = 0, \tag{2.48}$$

where $\rho E_{mag} = B^2/2\mu_0$ is the magnetic energy density. Using now the reduced Ohm's law, Equation (2.41), we can write Equation (2.48) as

$$\frac{\partial(\rho E_{mag})}{\partial t} + \underbrace{\frac{1}{\mu_0}\vec{\nabla}.(\eta\vec{J} \times \vec{B})}_{①} - \underbrace{\frac{1}{\mu_0}\vec{\nabla}.\big[(\vec{u} \times \vec{B}) \times \vec{B}\big]}_{②} = -\eta J^2 - \vec{u}.(\vec{J} \times \vec{B}), \tag{2.49}$$

where ① gives $\frac{\vec{B}}{\mu_0}.\big[\vec{\nabla} \times (\eta\vec{J})\big] - \eta J^2$ and ② gives $\frac{1}{\mu_0}\vec{\nabla}.\big[\vec{B}(\vec{u}.\vec{B})\big] - \vec{\nabla}.\big(\frac{B^2}{\mu_0}\vec{u}\big)$. The magnetic energy equation is thus written now as

$$\begin{aligned} \frac{\partial(\rho E_{mag})}{\partial t} + \vec{\nabla}.(\rho\vec{u}E_{mag}) = & - \vec{\nabla}.\big(\vec{u}\frac{B^2}{2\mu_0}\big) + \frac{1}{\mu_0}\vec{\nabla}.\big[\vec{B}(\vec{u}.\vec{B})\big] \\ & - \frac{\vec{B}}{\mu_0}.\big[\vec{\nabla} \times (\eta\vec{J})\big] - \vec{u}.(\vec{J} \times \vec{B}). \end{aligned} \tag{2.50}$$

The total energy equation is thus obtained by summing up Equation (2.36), Equation (2.47) and Equation (2.50) together, and it is given in its conservative form as

$$\begin{aligned} \frac{\partial(\rho E_{total})}{\partial t} + \vec{\nabla}.\big(\rho\vec{u}E_{total}\big) = & - \vec{\nabla}.\big[\vec{u}\big(p_{th} + \frac{B^2}{2\mu_0}\big)\big] + \eta J^2 \\ & + \frac{1}{\mu_0}\vec{\nabla}.\big[\vec{B}(\vec{u}.\vec{B})\big] - \frac{\vec{B}}{\mu_0}.\big(\vec{\nabla} \times (\eta\vec{J})\big) \\ & - \frac{1}{\mu_0}(\vec{u}.\vec{B})\vec{\nabla}.\vec{B}. \end{aligned} \tag{2.51}$$

Summarizing the above, Equations (2.30, 2.34, 2.46, 2.51) along with the reduced Ampère's law (Equation 2.32) and the ideal gas law (Equation 2.18) form the full set of equations of the resistive MHD model namely

$$\begin{aligned}
\frac{\partial \rho}{\partial t} + \vec{\nabla}.(\rho\vec{u}) &= 0 \quad , \\
\frac{\partial(\rho\vec{u})}{\partial t} + \vec{\nabla}.(\rho\vec{u}\vec{u}) &= - \quad \vec{\nabla}\big(p_{th} + \frac{B^2}{2\mu_0}\big) + \frac{1}{\mu_0}\vec{\nabla}.(\vec{B}\vec{B}) \\
&\quad - \quad \frac{1}{\mu_0}\vec{B}\vec{\nabla}.\vec{B}, \\
\frac{\partial \vec{B}}{\partial t} + \vec{\nabla}.(\vec{u}\vec{B}) - \vec{\nabla}.\big(\frac{\eta}{\mu_0}\vec{\nabla}\vec{B}\big) &= + \quad \vec{\nabla}.(\vec{B}\vec{u}) - \vec{\nabla}\big(\frac{\eta}{\mu_0}\vec{\nabla}.\vec{B}\big), \\
\frac{\partial(\rho E_{total})}{\partial t} + \vec{\nabla}.\big(\rho\vec{u}E_{total}\big) &= - \quad \vec{\nabla}.\big[\vec{u}\big(p_{th} + \frac{B^2}{2\mu_0}\big)\big] + \eta J^2 \\
+\frac{1}{\mu_0}\vec{\nabla}.\big[\vec{B}(\vec{u}.\vec{B})\big] &\quad - \quad \frac{\vec{B}}{\mu_0}.\big(\vec{\nabla}\times(\eta\vec{J})\big) - \frac{1}{\mu_0}(\vec{u}.\vec{B})\vec{\nabla}.\vec{B}.
\end{aligned} \tag{2.52}$$

2.7 The MHD Equations with Fluctuations

In this section, we first describe how the magnetic fluctuations are introduced for the coronal magnetic field. Then, we list the resistive MHD equations including the fluctuation terms.

As outlined in Chapter 1, our basic assumption is that the coronal magnetic field can be affected by fluctuations, which thought to be originated from the turbulent motion of the photospheric footpoints. We further assume that the fluctuations are lying in two-dimensional space, the $x-y$ plane. To implement the fluctuations into the MHD equations, we consider the total magnetic field $\vec{B}$ consisting of two parts $\vec{B}_M$ and $\vec{B}_F$, such that

$$\vec{B} = \vec{B}_M + \vec{B}_F, \tag{2.53}$$

where $\vec{B}_M$ is the mean magnetic field, and $\vec{B}_F$ represents the magnetic field fluctuations. Furthermore, in order to insure initially the momentum balance with a uniform plasma pressure, the initial coronal magnetic field must have a z-component B_z. As a consequence, the coronal magnetic field, including magnetic field fluctuations, is now generalized as

$$\vec{B} = \underbrace{\vec{B}_M + \vec{B}_F}_{x-y\ plane} + B_z\hat{z}. \tag{2.54}$$

Note that, in the present work, we refer to $\vec{B}_M$ as the coronal magnetic field in the $x-y$ plane ($\vec{B}_M = B_x\hat{x} + B_y\hat{y}$). Moreover, we use the resistive MHD model in which we insert the magnetic field according to Equation (2.54). The basic equations of our model, including the fluctuation part $\vec{B}_F$, are thus obtained as follows

$$\frac{\partial \rho}{\partial t} + \vec{\nabla}.(\rho\vec{u}_{xy}) = 0, \tag{2.55}$$

$$\begin{aligned}\frac{\partial(\rho\vec{u}_{xy})}{\partial t} + \vec{\nabla}.(\rho\vec{u}_{xy}\vec{u}_{xy}) = &- \vec{\nabla}p + \mu_0^{-1}\vec{\nabla}.\big(\vec{B}_M\vec{B}_M\big) \\ &- \mu_0^{-1}\big(\vec{B}_M\vec{\nabla}.\vec{B}_M\big) + \vec{S}_{u_{xy}},\end{aligned} \tag{2.56}$$

$$\begin{aligned}\frac{\partial(\rho u_z)}{\partial t} + \vec{\nabla}.(\rho\vec{u}_{xy}u_z) = &+ \mu_0^{-1}\vec{\nabla}.(\vec{B}_M B_z) - \mu_0^{-1}B_z\vec{\nabla}.\vec{B}_M \\ &+ S_{u_z},\end{aligned} \tag{2.57}$$

$$\begin{aligned}\frac{\partial\vec{B}_M}{\partial t} + \vec{\nabla}.(\vec{u}_{xy}\vec{B}_M) - \mu_0^{-1}\vec{\nabla}.(\eta\vec{\nabla}\vec{B}_M) = &+ \vec{\nabla}.(\vec{B}_M\vec{u}_{xy}) - \mu_0^{-1}\vec{\nabla}(\eta\vec{\nabla}.\vec{B}_M) \\ &+ \vec{S}_{B_M},\end{aligned} \tag{2.58}$$

$$\frac{\partial B_z}{\partial t} + \vec{\nabla}.(\vec{u}_{xy}B_z) - \mu_0^{-1}\vec{\nabla}.(\eta\vec{\nabla}B_z) = + \vec{\nabla}.(\vec{B}_M u_z) + S_{B_z}, \tag{2.59}$$

$$\begin{aligned}\frac{\partial(\rho E_{total})}{\partial t} + \vec{\nabla}.\big(\rho\vec{u}_{xy}E_{total}\big) = &- \vec{\nabla}.(\vec{u}_{xy}p) + \eta\vec{J}^2 \\ +\mu_0^{-1}\vec{\nabla}.\big[\vec{B}_M(\vec{u}_{xy}.\vec{B}_M + u_zB_z)\big] &- \mu_0^{-1}\big(\vec{B}_M + B_z\hat{z}\big).\big(\vec{\nabla}\times(\eta\vec{J})\big) \\ -\mu_0^{-1}(\vec{u}_{xy}.\vec{B}_M + u_zB_z)\vec{\nabla}.\vec{B}_M &+ S_E.\end{aligned} \tag{2.60}$$

The various quantities mentioned in the above equations are defined below:

- The plasma density is ρ, the plasma bulk velocity in the $x-y$ plane is $\vec{u}_{xy}$ $(= u_x\hat{x} + u_y\hat{y})$, and $\vec{\nabla}$ is the gradient operator in the $x-y$ plane. Moreover, we consider that the flow is uniform in the z-direction which implies $\partial_z = 0$.

- The total pressure is defined as $p = p_{th} + p_{mag}$, where p_{th} and p_{mag} are respectively the thermal and the magnetic pressure. Considering a hydrogen plasma in the corona as a monoatomic ideal gas, the thermal pressure can be written as $p_{th} = (\gamma - 1)\rho\varepsilon$, where $\gamma = 5/3$ is the ratio of the specific heats and ρ is the plasma density. The internal energy per unit mass ε is related to the plasma temperature T by $\varepsilon = (\gamma - 1)^{-1} R_M T$, where R_M $(= 8250$ SI units) is the ideal gas constant per molar mass. On the other hand, the magnetic pressure is $p_{mag} = B^2/2\mu_0$, where μ_0 is the permeability of free space and B is the magnitude of the total coronal field $\vec{B}$ given previously by Equation (2.54).

- The resistivity η used is either uniform or Spitzer-like. For reasons discussed later in Chapter 6, we artificially enhance the value of η by a multiplication factor in order to avoid small scales in our calculations at which the resistive MHD description fails.

- Recall that the total energy per unit mass is $E_{total} = \varepsilon + E_k + E_{mag}$, where $E_k = (u_x^2 + u_y^2 + u_z^2)/2$ is the kinetic energy per unit mass, and E_{mag} is the magnetic energy per unit mass equals to p_{mag}/ρ.

- The current density $\vec{J}$ is obtained from the Ampère's law according to $\vec{J} = \mu_0^{-1}\vec{\nabla} \times \vec{B}$.

- The terms $\vec{S}_{u_{xy}}$, S_{u_z}, $\vec{S}_{B_M}$, S_{B_z}, and S_E are handled as sources and sinks to the main plasma quantities due to fluctuations, and they are written in terms of $\vec{B}_F$ as follows:

- $\vec{S}_{u_{xy}} = +\mu_0^{-1}\Big[\vec{\nabla}.\big(\vec{B}_M\vec{B}_F + \vec{B}_F\vec{B}_M + \vec{B}_F\vec{B}_F\big) - \vec{B}_F\vec{\nabla}.\vec{B}_M\Big]$,
- $S_{u_z} = +\mu_0^{-1}\vec{\nabla}.\big(\vec{B}_F B_z\big)$,
- $\vec{S}_{B_M} = -\partial\vec{B}_F/\partial t - \vec{\nabla}.(\vec{u}_{xy}\vec{B}_F) + \vec{\nabla}.\big(\frac{\eta}{\mu_0}\vec{\nabla}\vec{B}_F\big) + \vec{\nabla}.(\vec{B}_F\vec{u}_{xy})$,
- $S_{B_z} = +\vec{\nabla}.\big(\vec{B}_F u_z\big)$,
- $S_E = +\mu_0^{-1}\Big[\vec{\nabla}.\big[(\vec{B}_M + \vec{B}_F)(\vec{u}_{xy}.\vec{B}_F)\big] + \vec{\nabla}.\big[\vec{B}_F(\vec{u}_{xy}.\vec{B}_M + u_z B_z)\big]$
  $- (\vec{u}_{xy}.\vec{B}_F)\vec{\nabla}.\vec{B}_M - \vec{B}_F.\vec{\nabla}\times(\eta\vec{J})\Big]$.

We treat the effects of turbulent motion of the photospheric footpoints as fluctuations in the coronal magnetic fields. In other words, $\vec{B}_F$ is an imposed quantity in the Equations. (2.55)−(2.60) assumed coming from the photosphere. Therefore, all the coronal quantities in the MHD equations will thus be changed due to $\vec{B}_F$ when exists. Finally, note that the traditional two-dimensional resistive MHD equations, without fluctuations, are recovered by setting $\vec{B}_F = \vec{0}$, $B_z = 0$, $u_z = 0$, and take $\vec{B} = \vec{B}_M$ and $\vec{u} = \vec{u}_{xy}$.

Chapter 3

Discretization processes and Algorithms

3.1 Introduction

The study of partial differential equations (PDEs) in complete generality is a vast undertaking. As almost all of them are not solved analytically, we must rely on numerical methods. The most conservative one is the finite volume method. In this chapter, we first discuss the methodology of the finite volume approach by presenting a proper way to discretize a conservation equation in one dimensional space. Second, we study the discretization process of the temporal term and use the appropriate time scheme for our simulation. Third, the discretized equations are then transformed into a system of linear algebraic equations of the form $\mathbf{A}\phi = \mathbf{B}$. $\mathbf{A}$ and $\mathbf{B}$ are respectively the matrix and the vector of all known quantities comprising the coefficients and the source/sink terms of the discretized equations, and ϕ's are the unknowns we seek. Finally, the obtained system of linear equations is solved using either direct or iterative methods. The direct methods solve the problem by a finite sequence of operations like solving a linear system of equations by Gaussian elimination. The iterative methods solve the

problem using an initial guess to generate a sequence of improving approximate solutions.

3.2 Finite Volume Method

The finite volume method is based on the integral form of the governing equations. According to Patankar [81], the most attractive feature of the formulation in finite volumes is that the conservation principle is satisfied exactly for any control volume. It is easy to conclude that this principle holds for the entire solution domain, which is no more than the sum of all control volumes.
As mentioned in the book of Moukalled et al. [82], the Finite Volume Method (FVM) is a numerical technique that transforms partial differential equations representing the conservation laws of differential volumes into discrete algebraic equations over finite volumes (or elements or cells). Similar to the finite difference or finite element method, the first step in the solution process is the discretization of the geometric domain into non-overlapping elements or finite volumes. The partial differential equations are then discretized or transformed into algebraic equations by integrating them over each discrete element. The system of algebraic equations is then solved to compute the values of the dependent variable for each element. In the FVM, some terms of the conservative equation are transformed into face fluxes and evaluated at the finite volume faces. As the flow entering a given volume is identical to that coming out from the adjacent volume, the FVM is strictly conservative. This conservation property inherent to the FVM is the preferred method in Computational Fluid Dynamics (CFD). Another important attribute of FVM is that it can be formulated in a physical space on unstructured polygonal meshes. Finally, in the FVM, it is very easy to implement a variety of boundary conditions, because the unknown variables are evaluated at the centroids of the volume elements and not at their boundary faces. These features have made the FVM perfectly suitable for the numerical simulation of

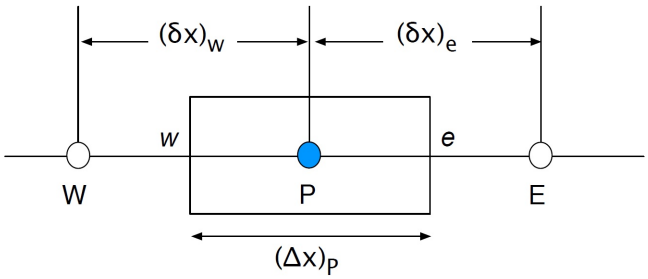

Figure 3.1: The discretization of the computational domain in one-dimensional space.

various applications involving fluid flow, heat and mass transfer, etc... . From an exclusive prospect limited to solving simple physical and geometric problems on structured meshes, FVM is now able to handle all types of physics and complex applications.

3.3 Space Discretization

In the finite volume discretization process, we integrate the governing equation over the finite volumes of the computational domain, then we transform the volume integrals of the convection and diffusion terms into surface integrals using Gauss' theorem. After that, the surface and volume integrals are transformed into discrete ones and integrated numerically through the use of integration points. To clarify this approach, let's take as an example the following steady-state conservation equation for a general scalar variable ϕ which can be expressed as

$$\underbrace{\vec{\nabla}.(\rho\vec{v}\phi)}_{Convection\ Term} = \underbrace{\vec{\nabla}.(\Gamma\vec{\nabla}\phi)}_{Diffusion\ Term} + \underbrace{Q}_{Source\ Term} . \tag{3.1}$$

By integrating the above equation over the element P of one-dimensional domain

shown in Figure (3.1), Equation (3.1) is transformed to

$$\int_{V_P} \vec{\nabla}.(\rho\vec{v}\phi)\mathrm{dv} = \int_{V_P} \vec{\nabla}.(\Gamma\vec{\nabla}\phi)\mathrm{dv} + \int_{V_P} Q\mathrm{dv}. \tag{3.2}$$

By using the divergence theorem, we replace the volume integrals of the convection and diffusion terms by surface integrals, the above equation becomes

$$\oint_{\partial V_P} (\rho\vec{v}\phi).\mathrm{d}\vec{S} = \oint_{\partial V_P} (\Gamma\vec{\nabla}\phi).\mathrm{d}\vec{S} + \int_{V_P} Q\mathrm{dv}, \tag{3.3}$$

where **bold** letters indicate vectors, (.) is the dot product operator, Q represents the source term, $\vec{S}$ is the surface vector, $\vec{v}$ is the velocity vector, ϕ is the conserved quantity, and $\oint_{\partial V_P}$ the surface integral over the volume V_P. Let's continue now in one-dimensional space, the surface integral represents the sum of all the fluxes of the variable ϕ over the faces e and w of the element (or control volume) P. Thus, Equation (3.3) transforms to

$$\sum_f \dot{m}_f\phi_f - \sum_f \Gamma_f(\vec{\nabla}\phi)_f.\vec{S} = \int_w^e Q\mathrm{dx}, \tag{3.4}$$

where $\dot{m}$ $(= \rho\vec{v}.\vec{S})$ represents the mass flow rate evaluated at the faces of the elements, and the subscript f refers to faces e and w of the control volume P. The convection and diffusion terms on the left hand side can be thus written as

$$\begin{aligned} \sum_f \dot{m}_f\phi_f &= (\rho v\phi)_e - (\rho v\phi)_w, \\ \sum_f \Gamma_f(\vec{\nabla}\phi)_f.\vec{S} &= (\Gamma\nabla\phi)_e - (\Gamma\nabla\phi)_w. \end{aligned} \tag{3.5}$$

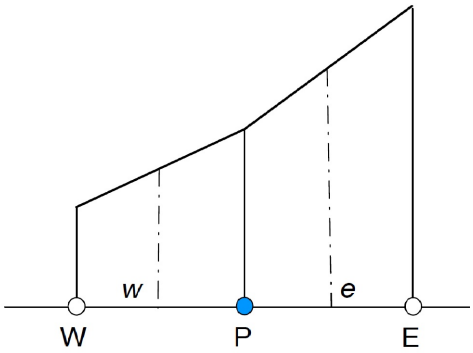

Figure 3.2: Linear profile applied to evaluate the variable ϕ and its derivative on the faces e and w of the control volume of element P.

The terms v and $\nabla\phi$ on the right hand sides of Equation (3.5) are respectively $v = \vec{v}.\vec{S}$ and $\nabla\phi = \vec{\nabla}\phi.\vec{S}$. Thus, Equation (3.4) can be written now as

$$(\rho v\phi)_e - (\rho v\phi)_w - [(\Gamma\nabla\phi)_e - (\Gamma\nabla\phi)_w] = \int_w^e Q\mathrm{dx}. \tag{3.6}$$

Each term on the left hand side of Equation (3.6) should be evaluated using an interpolation profile. For example, if we apply the linear profile, shown in Figure (3.2), on the terms $(\rho v\phi)_e$ and $(\Gamma\nabla\phi)_w$, they can be expressed as

$$\begin{aligned} (\rho v\phi)_e &= (\rho v)_e\phi_e \quad = (\rho v)_e \frac{(\phi_E + \phi_P)}{2}, \\ (\Gamma\nabla\phi)_w &= \Gamma_w\Big(\frac{\mathrm{d}\phi}{\mathrm{dx}}\Big)_w = \Gamma_w \frac{\phi_P - \phi_W}{(\delta x)_w}. \end{aligned} \tag{3.7}$$

Having applied the linear profile to all terms, we write Equation (3.6) as

$$(\rho v)_e \frac{(\phi_E + \phi_P)}{2} - (\rho v)_w \frac{(\phi_W + \phi_P)}{2} + \Gamma_w \frac{\phi_P - \phi_W}{(\delta x)_w} - \Gamma_e \frac{\phi_E - \phi_P}{(\delta x)_e} = Q_P(\Delta x)_P. \tag{3.8}$$

Finally, we get the algebraic form of Eq.(3.8) which reads

$$a_p\phi_P = a_E\phi_E + a_W\phi_W + b = \sum_{NB=E,W} a_{NB}\phi_{NB} + b, \tag{3.9}$$

where

$$a_E = \frac{\Gamma_e}{(\delta x)_e} - \frac{(\rho v)_e}{2}, \qquad a_W = \frac{\Gamma_w}{(\delta x)_w} + \frac{(\rho v)_w}{2},$$

$$a_P = \frac{(\rho v)_e}{2} - \frac{(\rho v)_w}{2} + \frac{\Gamma_w}{(\delta x)_w} + \frac{\Gamma_e}{(\delta x)_e}, \qquad b = Q_P(\Delta x)_P.$$

The subscript $_{NB}$ shown above represents the neighbor elements of the control volume of element P.

3.4 Time Discretization

Time discretization involves the integration of every term in the differential equation over a time step Δt. The evolution of the interior points could be done by an explicit, an implicit scheme or by a hybrid one made of the two. These mentioned schemes will be discussed in this section by using Equation (3.1) as an example. Let us include the time contribution to Equation (3.1) which reads now

$$\frac{\partial(\rho\phi)}{\partial t} + \vec{\nabla}.(\rho\vec{v}\phi) - \vec{\nabla}.(\Gamma\vec{\nabla}\phi) = Q. \tag{3.10}$$

The time discretization process of Equation (3.10) is performed in the equation resulting from the spatial discretization treated in the previous section. The implications of including the non-stationary term in the discretized equation are given by:

$$\int_t^{t+\Delta t} \left[\left(\frac{\partial(\rho\phi)}{\partial t} \right)_P V_P + \sum_f \dot{m}_f \phi_f - \sum_f \Gamma_f (\vec{\nabla}\phi)_f . \vec{S} \right] \mathrm{dt} = \int_t^{t+\Delta t} Q_P V_P \mathrm{dt}. \tag{3.11}$$

Since time is a one-way coordinate, the calculation is done by time marching. It starts from an initial value $\phi^n = \phi(t)$, based on the previous time step, and progresses in time in order to obtain a new value for the dependent variable, $\phi^{n+1} = \phi(t + \Delta t)$

Assuming a linear variation,

$$\phi(t+\Delta t) = \phi(t) + \Delta t \left(\frac{\partial \phi}{\partial t}\right)_t, \tag{3.12}$$

the temporal term and the integration in time can be calculated as

$$\begin{aligned} \left(\frac{\partial(\rho\phi)}{\partial t}\right)_P &= \frac{\rho_P^{n+1}\phi_P^{n+1} - \rho_P^n \phi_P^n}{\Delta t}, \\ \int_t^{t+\Delta t} \phi(t)\mathrm{dt} &= \left(g_t \phi_P^{n+1} + (1-g_t)\phi_p^n\right). \end{aligned} \tag{3.13}$$

where g_t is a temporal interpolation factor, which can range from 0 to 1. If $g_t = 0$ the discretization results is a totally explicit scheme, since the value of ϕ of the previous time step prevails (ϕ^n). If $g_t = 1$ the scheme reverts to the fully implicit one, since it is the new value of ϕ (ϕ^{n+1}) that remains in Equation (3.13).
Using a totally explicit scheme, and assuming that the density and the diffusion coefficient do not change with time, the discretized equation, Equation (3.11), is given by:

$$\left(\frac{\rho_P V_P}{\Delta t}\right)\phi_P^{n+1} = -\sum_f \dot{m}_f \phi_f^n + \sum_f \Gamma_f (\vec{\nabla}\phi)_f^n . \vec{S} + Q_P^n V_P + \left(\frac{\rho_P V_P}{\Delta t}\right)\phi_P^n. \tag{3.14}$$

Thus, all terms in Equation (3.14) depend only on the values obtained in the previous time step, and there is no relation to the other variables of the current time step. This approach simplifies the resolution of the transport equation, since the value of ϕ^{n+1} can be calculated directly without the need to solve a system of linear equations. Of course there is a snag, this is given by Courant's criterion of stability or number [83]. For a case of one-dimensional flow with variation along the x-direction, the stability criterion is given by:

$$Co = \frac{U_x \Delta t}{\Delta x}. \tag{3.15}$$

Equation (3.15) represents the ratio between the time step Δt and the characteristic convection time $\frac{\Delta x}{U_x}$. It should be noted that the characteristic time of convection, although it can vary spatially, is a fundamental parameter and depends on the physics of the flow. In the specific case of compressible MHD flow, it is in the interest of the formulation to consider not only the flow velocity but also the fast-wave velocity, see [84]. In the explicit formulation, when the Courant number is greater than unity, numerical instabilities occur which completely destroy the results. On the other hand, in the fully implicit scheme the discretized equation is identical to Equation (3.14), and there is only the need to replace the upper indices n by $n+1$. The scheme is still of the first order in time, however, in contrast to the explicit scheme, there is a need to solve a system of equations, since the value of ϕ_p^{n+1} depends on the new values of the neighboring control volumes of element P. As an advantage, this scheme allows a better coupling between the variables and the system becomes more stable, even if the stability criterion $Co > 1$.

There is also the possibility of assuming an interpolation factor equal to $g_t = 0.5$, which leads to the Crank-Nicolson scheme. Such a scheme calculates the new value of ϕ based on the values of ϕ known in the previous time step, and the unknown values of the current time step. So, by using the Crank-Nicolson scheme, Equation (3.14) reads now

$$\begin{aligned}\left(\frac{\rho_P V_P}{\Delta t}\right)\phi_P^{n+1} &= \left(\frac{\rho_P V_P}{\Delta t}\right)\phi_P^{n} + \frac{1}{2}\Bigg[- \sum_f \dot{m}_f \phi_f^n + \sum_f \Gamma_f (\vec{\nabla}\phi)_f^n . \vec{S} \\ &+ \frac{1}{2} Q_P^n V_P \Bigg] + \frac{1}{2}\Bigg[- \sum_f \dot{m}_f \phi_f^{n+1} + \sum_f \Gamma_f (\vec{\nabla}\phi)_f^{n+1} . \vec{S} + \frac{1}{2} Q_P^{n+1} V_P \Bigg].\end{aligned} \tag{3.16}$$

Unlike the two schemes presented earlier, the Crank-Nicolson scheme is a second order scheme in time. However this scheme can also lead to oscillations if the Δt is not small enough. The criterion of stability is again given by the Courant number, but this criterion is not as restrictive as for the totally explicit case. So,

we may able to have stability even if $Co > 1$.

3.5 Solving Algebraic Equations

The result, Equation (3.9), of the discretization process is a system of linear equations of the form $\mathbf{A}\phi = \mathbf{B}$ where the unknowns ϕ, located at the centroids of the mesh elements, are the sought after values. In this system, the coefficients of the unknown variables constituting the matrix $\mathbf{A}$ are the result of the linearization procedure and the mesh geometry, while the vector $\mathbf{B}$ contains all sources, constants, boundary conditions, and non-linearizable components [82].

The term a_P of Equation (3.9) represents the coefficients present in the main diagonal of the matrix $\mathbf{A}$, and a_{NB} represents the coefficients outside the main diagonal. In transient state, when this system is solved it generates a new set of ϕ's for the current time. The coefficient a_P includes all terms corresponding to the current time step, namely: the time derivative; the diffusion term; the convection term and the linear part of the source term. The coefficient a_{NB} contains the terms corresponding to the neighboring nodes of the point P. The term b, in Equation (3.9), has all the terms that can be calculated without having to know the values of ϕ of the current time step. Namely, the constant part of the source term and the parts of the diffusion, convection and temporal terms corresponding to the previous time step.

Techniques for solving linear systems of equations are generally grouped into direct and iterative methods, with many sub-groups in each category. Since flow problems are highly non-linear, the coefficients resulting from their linearization process are generally dependent. For this reason and since an accurate solution is not needed at each iteration, direct methods have been rarely used in CFD applications. Iterative methods, on the other hand, have been more popular because they are more suited for this type of applications requiring lower computational cost per iteration and lower memory.

Chapter 4

Implementation and Simulation

4.1 Introduction

An overview of the literature reveals that there are plenty of methods handling compressible flow problems at arbitrary Mach numbers. Those methods have been proposed for solving the Euler and Navier-Stokes equations. However, the development of similar methods for the analysis of MHD flow is practically rare existent. In this chapter, a method of analysis of compressible MHD flow will be described, which should be applicable to a wide range of Mach numbers. Initially the method will be developed to solve the Euler equations, which can be considered as a special case of the MHD equations when the magnetic field is zero. We will focus here on the Pressure Based Algorithm (PBA) methods that were deduced for the compressible flow analysis. There are several algorithms of this type but we can identify two that clearly stand out, namely the SIMPLE (Semi-Implicit Method for Pressure-Linked Equations) and the PISO (Pressure-Implicit with Splitting Operators).

4.2 Numerical Methods

4.2.1 Overview

The SIMPLE was initially proposed by Patankar and Spalding [85] for the modeling of incompressible flow at steady state. The PISO was introduced by Issa [86] for the calculation of non-stationary flow, incompressible or compressible, of the Navier-Stokes equations.

SIMPLE was the first algorithm of the PBA methods. However, numerous modifications were introduced in order to improve its robustness and convergence rate. As an example we can refer to SIMPLEC (SIMPLE Consistent) by Van Doormaal and Raithby [87]; or the SIMPLEM of Acharya and Moukalled [88]. For the PISO algorithm, some variants have also appeared in relation to the original scheme, such as that introduced by Oliveira and Issa [89], in order to calculate natural convection dominated flows.

In the modeling of plasma flow, there is sometimes a need to construct a system of equations for each of the species involved (ions, electrons and neutral species). Such systems are known as multi-species or multi-fluid MHD equations. Although the basic algorithm that will be proposed is based on the MHD approximation for a single fluid, it seems obvious to us that it must have the capacity to be adapted to much more complex flow regimes. Darwish et al. [90] modified the formulation of several algorithms of SIMPLE and PISO type so that they can calculate multi-fluid flow where, depending on the adopted formulation, two new concepts emerged. The first concept was based on Mass Conservation Based Algorithm (MCBA) and the second concept was based on the so-called Geometric Conservation Based Algorithm (GCBA). Following the MCBA model, the pressure equation must be constructed on the basis of the mass conservation equation, which is nothing more than the sum of all n continuity equations for n fluids. On the other hand, in the deduction of the pressure equation with the GCBA

formulation, a geometric conservation equation must be used, which is given by the sum of all the volume fractions. Both algorithms were subsequently modified and tested by Moukalled et al [91] and later by Moukalled and Darwish [92, 93] for the calculation of flow to arbitrary Mach number.

A fundamental characteristic, which must be considered in the deduction of a numerical method of solution, is the calculation time required to reach convergence. The PISO algorithm, being a non-stationary solution method, allows us to obtain time dependent solutions with relative precision. On the other hand, SIMPLE is an adequate choice when accelerating the convergence rate for steady-state solutions. Nevertheless, it is possible to use PISO in obtaining stationary solutions with the disadvantage that it requires a very short time step in extremely refined meshes. Darwish et al [94] developed a comparative study of the performance of the various algorithms with regard to their convergence rate, in which they implemented the multiple mesh technique. In algorithms of the segregated type, for steady-state solutions, the multiple-mesh technique is expected to increase the convergence rate considerably. A further discussion about the implementations of SIMPLE and PISO methods is presented in the next subsection.

4.2.2 Implementations of SIMPLE and PISO Methods

SIMPLE and PISO are two proposed algorithms for solving the Navier-Stokes equations. Both methods are used to guarantee the continuity equation. SIMPLE is designed for steady cases (time derivatives are set to zero) and incompressible flows, whereas PISO is used for unsteady cases and incompressible or compressible flows. Thus, the main difference between the two algorithms is the time derivative if it takes into account or not.

Let us now explain the implementation of the SIMPLE and PISO methods. The two methods follow a segregated approach, which implies that the set of governing equations is solved sequentially. That is, each equation is solved for the reference

variable assuming that the other variables do not vary. The segregated method is iterative in nature and, in the case of SIMPLE and PISO, involves prediction and correction steps. In the prediction step, the velocity field is calculated by solving the momentum equation in its implicit form. This is based on the pressure values obtained in the previous time step, or estimated if we are in the initial time step. In the correction step an implicit equation for the pressure is deduced and solved, and subsequently the velocity field and the density are corrected through algebraic expressions.

The table of Figure (4.1) presents the steps of SIMPLE and PISO methods. The upper index n is relative to the values obtained in the previous time step, and the upper indices *, **, *** represent the consecutive predictions and corrections of the algorithm.

4.2.3 BPISO Method

Based on Gauss's law for magnetism, the divergence of the magnetic field should remain free at all times. However, numerical solutions may violate this divergence-free constraint leading to nonphysical quantities and numerical instabilities. Several methods were developed trying to enforce $\vec{\nabla}.\vec{B} = 0$. These methods are the constraint transport method [95], the eight-wave solution [96], the projection and the hyperbolic divergence cleaning methods [97]. For more details, see the book of [98] and the references therein.

In our MHD calculations, we use the projection method for the magnetic field divergence cleaning. We solve the Poisson's equation in order to remove the additional part of the magnetic field that leads to non-zero divergence [99]. Let $\vec{B}^*$ be the magnetic field after a time-step Δt with $\vec{\nabla}.\vec{B}^* \neq 0$. The field $\vec{B}$ at the next time-step should be corrected by subtracting the unphysical part, generated

SIMPLE (Semi Implicit Methods Pressure Linked Equations)	PISO (Pressure Implicit Split Operator)
• Algorithm is designed for steady cases • Assume Navier-Stokes equations for incompressible fluid flow: $\nabla . U = 0.$ • The momentum conservation equation (velocity equation): $U . \nabla U - \nabla . (\nu \nabla U) = -\nabla p$ • When the momentum equation is discretized: $M . U = -\nabla p$ $A . U - H = -\nabla p$ A is a diagonal matrix of the original matrix M, and H is a vector. • Express U from the momentum equation: $U = A^{-1} . H - A^{-1} . \nabla p$ • Combine momentum correction equation and continuity equation, which gives us: $\nabla . (A^{-1} . \nabla p) = \nabla . (A^{-1} . H)$	• Algorithm is designed for unsteady cases • Assume Navier-Stokes equations for incompressible fluid flow: $\nabla . U = 0.$ • The momentum conservation equation (velocity equation): $\frac{\partial U}{\partial t} + U . \nabla U - \nabla . (\nu \nabla U) = -\nabla p$ • When the momentum equation is discretized: $M . U = -\nabla p$ $A . U - H = -\nabla p$ A is a diagonal matrix of the original matrix M, and H is a vector. • Express U from the momentum equation: $U = A^{-1} . H - A^{-1} . \nabla p$ • Combine momentum correction equation and continuity equation, which gives us: $\nabla . (A^{-1} . \nabla p) = \nabla . (A^{-1} . H)$
SIMPLE algorithm description	PISO algorithm description
1) Computation starts, initial U^n and p^n are chosen 2) Time step starts 3) Boundary conditions are updated 4) Linear system is solved $M . U^n = -\nabla p^n$ 5) Relaxation for velocity U 6) Obtain new velocity U^* 7) Building matrix A and vector H 8) Mass flow rate over cell faces is computed 9) Pressure correction is applied $\nabla . (A^{-1} . \nabla p^n) = \nabla . (A^{-1} . H)$ 10) Relaxation for pressure p 11) Obtain new pressure p' 12) Mass flow over cell faces is corrected 13) Momentum correction is applied $U = A^{-1} . H - A^{-1} . \nabla p'$ 14) Obtain new corrected velocity U^{**} 15) Boundary conditions are updated 16) Steps 5 – 15 are repeated with respect to *nCorrectors* value 17) Time step ends	1) Computation starts, initial U^n and p^n are chosen 2) Time step starts 3) Boundary conditions are updated 4) Linear system is solved $M . U^n = -\nabla p^n$ 5) Obtain new velocity U^* 6) Building matrix A and vector H 7) Mass flow rate over cell faces is computed 8) Pressure correction is applied $\nabla . (A^{-1} . \nabla p^n) = \nabla . (A^{-1} . H)$ 9) Obtain new pressure p' 10) Mass flow rate over cell faces is corrected 11) Momentum correction is applied $U = A^{-1} . H - A^{-1} . \nabla p'$ 12) Obtain new corrected velocity U^{**} 13) Boundary conditions are updated 14) Steps 6 – 13 are repeated with respect to *nCorrectors* value 15) Time step ends

Figure 4.1: The steps of SIMPLE and PISO algorithms.

by the numerical scheme, according to

$$\vec{B} = \vec{B}^* - \vec{\nabla}\phi. \tag{4.1}$$

The scalar function ϕ is obtained using the Poisson's equation

$$\vec{\nabla}^2\phi = \vec{\nabla}.\vec{B}^*. \tag{4.2}$$

Consequently, the divergence of the magnetic field gets reduced to a minimum value, but $\vec{\nabla}.\vec{B}$ is still non-zero. In Chapter 6, we discuss a critical value in order to assess the non-zero divergence of the magnetic field $\vec{B}$. By using Equation (4.1), we can verify that this correction does not change the current density $\vec{J} = \vec{\nabla}\times\vec{B} = \vec{\nabla}\times\vec{B}^*$, where $\vec{\nabla}\times\vec{\nabla}\phi = 0$. This method does not need to be applied in all time steps, but only to eliminate errors when they reach a predetermined value. Its use becomes useful when the initial field $\vec{B}$ is not known, because this technique allows to eliminate the divergence errors of the initial field $\vec{B}$.

4.3 OpenFOAM Code

The OpenFOAM (Open source Field Operation And Manipulation) code is a numerical simulation package of continuous media mechanics [82]. The source code is written in C++ language and follows an object-oriented programming line. The choice of this tool as a support for the development of the codes was that it is completely open to the public and relatively easy to acquire.

I do not intend, in this section, to analyze this program in detail, just to give the reader a certain notion of its capabilities. First of all, this code uses a space discretization based on the finite volume method. The various operators of the differential equations can be treated explicitly by the finite volume calculus (fvc) method or implicitly through the finite volume method (fvm). The first method

computes a field by solving the explicit derivatives, and the second method converts the expression to matrix coefficients through the implicit derivatives. The proposed idea is to look at each of the differential equations as the sum of the several associated differential operators, which can be approximated separately through the different discretization schemes.

Let us take for example the momentum equation for a viscous fluid written in its vector form:

$$\frac{\partial(\rho\vec{U})}{\partial t} + \vec{\nabla}.(\rho\vec{U}\vec{U}) - \vec{\nabla}.(\nu\vec{\nabla}\vec{U}) = -\vec{\nabla}p. \tag{4.3}$$

This equation can be easily implemented within the OpenFoam code through a very intuitive language,

$$\begin{aligned} solve(\quad & fvm \;\; :: \;\; ddt(rho, U) \\ & +fvm \;\; :: \;\; div(mdotf, U) \\ & -fvm \;\; :: \;\; laplacian(nu, U) == -fvc :: grad(p) \quad); \end{aligned}$$

where $mdotf$ ($\dot{m}_f = \rho\vec{U}.\vec{S}$) is the mass flux evaluated at the faces of the elements, and ν is the dynamic viscosity of the considered fluid.

Besides the ease of programming, there are other advantages that result from the use of this tool, such as: parallel processing capacity; several algorithms for solving systems of algebraic equations; various high-resolution interpolation schemes; various pre- and post-processing tools; and also the possibility of using unstructured meshes. These particularities, together with many others, make this an ideal tool for the development of new numerical codes. Thus, this seems to be the best choice to develop and test the algorithms proposed in this thesis. In this way, the investigator can look at the physics of his problem, and can direct his work plan for further research goals.

Finally, remember that our goal in this thesis is to investigate the effect of fluctuations on the MGR and the heating processes in the solar corona. For this sake, we have derived our basic equations using the resistive MHD model, as discussed in Chapter 2, modified by including the fluctuation terms, Equation (2.55) to Equation (2.60). We have already developed a code using the openfoam toolbox simulating the MGR process, without fluctuations, based on the solar corona conditions [100, 101]. The MHD code applied here, unlike [100], is improved using PISO and BPISO, and it is done for both fluctuation and non-fluctuation cases. The PISO is used to guarantee the conservation of mass (continuity), whereas the BPISO is used to minimize the divergence of the magnetic field.

Chapter 5

Test Cases

5.1 Introduction

Before presenting our results and to check out the validity of our MHD code when handling the MGR process, we have recovered three cases in the literature. The MHD equations mentioned in Chapter 2, Equation (2.55) to Equation (2.60), can be divided into two parts, the fluid part and the MHD one. Numerical code testing is done for these two parts using two test cases in the literature. The fluid test case is the flow over a bump; it is a special case analyzing the gas dynamics of the MHD flow when the magnetic field $\vec{B} = \vec{0}$. The MHD test case is the Orszag-Tang vortex; it analyses the dynamics of an ideal MHD conductive flow subject to a magnetic field ($\vec{B} \neq \vec{0}$). Furthermore, and since our aim is to investigate the MGR with and without fluctuations, a third case is needed to test the MGR process. This MGR case is done for the Spitzer resistivity model initiated by a localized resistivity around the origin.

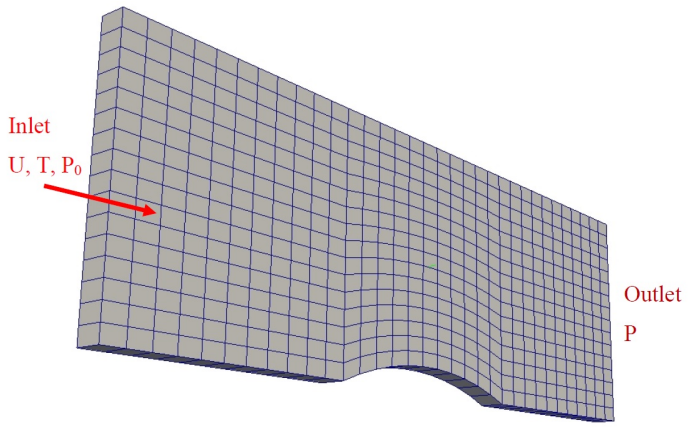

Figure 5.1: A 3D view of the mesh of the channel flow over a bump and its corresponding boundary conditions.

5.2 Test Case for Fluid Dynamics: Transonic Flow over a Bump

The equations for this test case are

$$\begin{aligned} \frac{\partial \rho}{\partial t} + \vec{\nabla}.(\rho\vec{u}) &= 0, \\ \frac{\partial(\rho\vec{u})}{\partial t} + \vec{\nabla}.(\rho\vec{u}\vec{u}) &= -\vec{\nabla}p, \\ \frac{\partial \rho(\varepsilon + \frac{1}{2}u^2)}{\partial t} + \vec{\nabla}.(\rho\vec{u}(\epsilon + \frac{1}{2}u^2)) &= -\vec{\nabla}.(p\vec{u}), \end{aligned}$$

where p is the thermal pressure, and remember that ε is the internal energy per unit mass. The third equation in the above set denotes the hydrodynamic energy equation, i.e. internal + kinetic.

This case is two-dimensional and refers to a transonic flow with a Mach number at the input equal to $Ma = 0.675$. Figure (5.1) is a 3D view of the mesh used to perform the computation and the corresponding boundary conditions. The length of the bump is equal to the channel height, and its thickness is 10 percent of the channel height. This type of flow is characterized by being subsonic in the inlet and outlet regions. However, the increase in velocity will create a shock

wave in the region downstream the top of the bump. For the pure gas dynamic

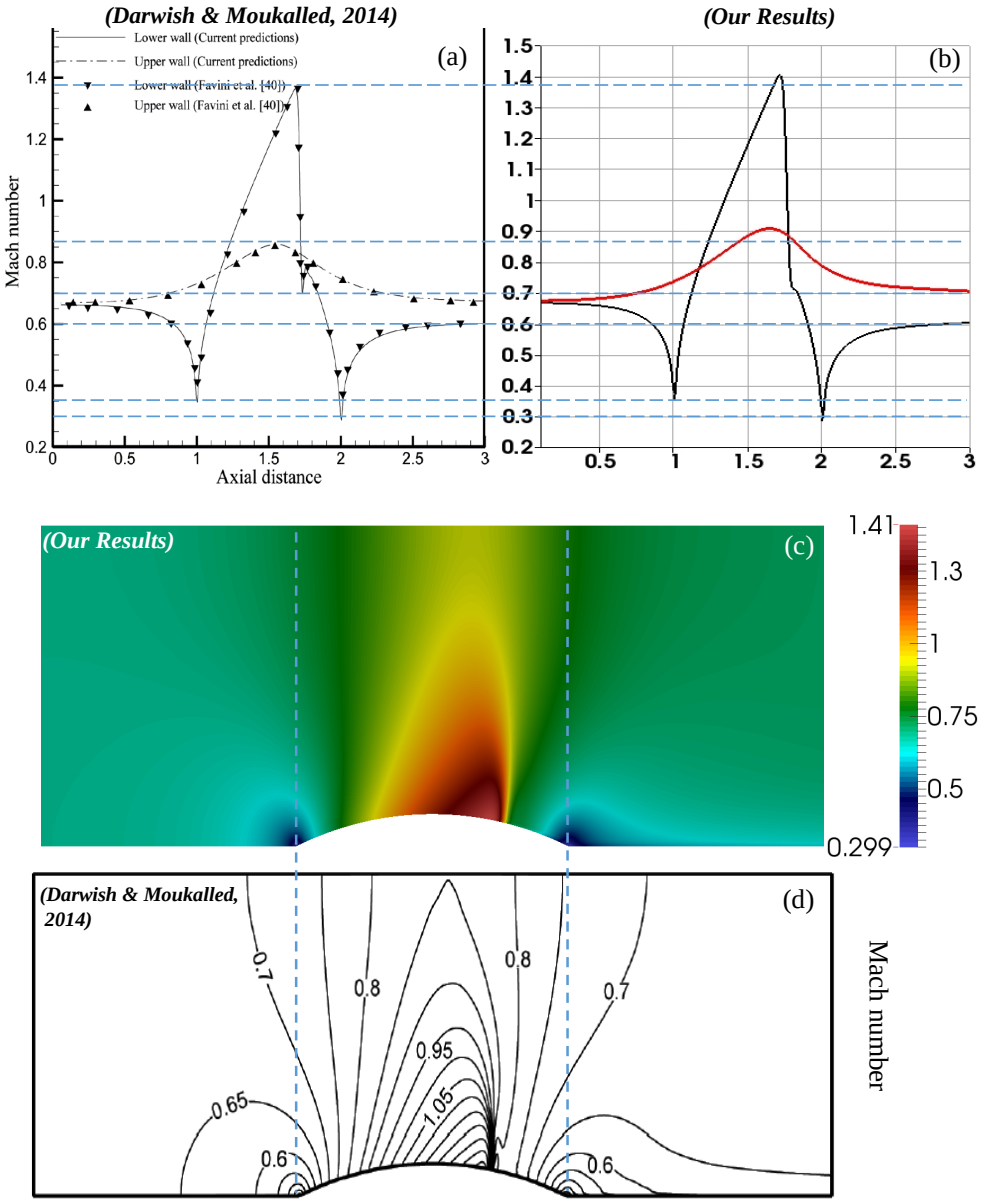

Figure 5.2: Test case of transonic flow over a circular arc bump where inlet Mach number is 0.675. (a) is the plot of Mach number values along the upper and lower walls published by [1, 2]. (b) is the same plots using the fluid part of our code. (c) is the Mach contours for the flow using our code. (d) is the same contours of Mach number published by [1].

problem, the following boundary conditions are considered: at inlet we impose temperature and total pressure; at outlet we impose static pressure. All the remaining variables are extrapolated from the domain.
In Figure (5.2), Mach number values are plotted along the upper and lower walls of the domain. Panel (a) is the results of these two plots found in the literature. Panel (b) shows the same plots using our code. Similarly, a distribution of the isolines relative to the Mach number is shown for both literature (panel (d)) and by using the data of our code (panel (c)). The results present good agreement with those obtained by Darwish and Moukalled [1].

5.3 Test Case for MHD: Orszag-Tang Vortex

The equations for this test case are

$$\begin{aligned}
\frac{\partial \rho}{\partial t} + \vec{\nabla}.(\rho\vec{u}) &= 0, \\
\frac{\partial(\rho\vec{u})}{\partial t} + \vec{\nabla}.(\rho\vec{u}\vec{u}) &= -\vec{\nabla}\big(p + \frac{B^2}{2\mu_0}\big) + \vec{\nabla}.\big(\frac{\vec{B}\vec{B}}{\mu_0}\big), \\
\frac{\partial \vec{B}}{\partial t} + \vec{\nabla}.(\vec{u}\vec{B}) &= \vec{\nabla}.(\vec{B}\vec{u}), \\
\frac{\partial \rho E_{total}}{\partial t} + \vec{\nabla}.(\rho\vec{u}E_{total}) &= -\vec{\nabla}.\big[\big(p + \frac{B^2}{2\mu_0}\big)\vec{u}\big] + \frac{1}{\mu_0}\vec{\nabla}.\big[(\vec{B}.\vec{u})\vec{B}\big],
\end{aligned}$$

where $E_{total} = \varepsilon + \frac{1}{2}u^2 + \frac{B^2}{2\rho\mu_0}$ is the total energy per unit mass, i.e. internal + kinetic + magnetic. The Orszag-Tang vortex is a standard two-dimensional test case that is often used in the validation of high resolution numerical schemes for ideal MHD flow. This problem is characterized by developing a very complex interaction between the various MHD discontinuities generated by the evolution of the vortex. This feature makes this test case suitable for evaluating the proposed method in terms of accuracy and robustness. The purpose of the Orszag-Tang vortex is to test how well the code handles MHD turbulence and shocks. The

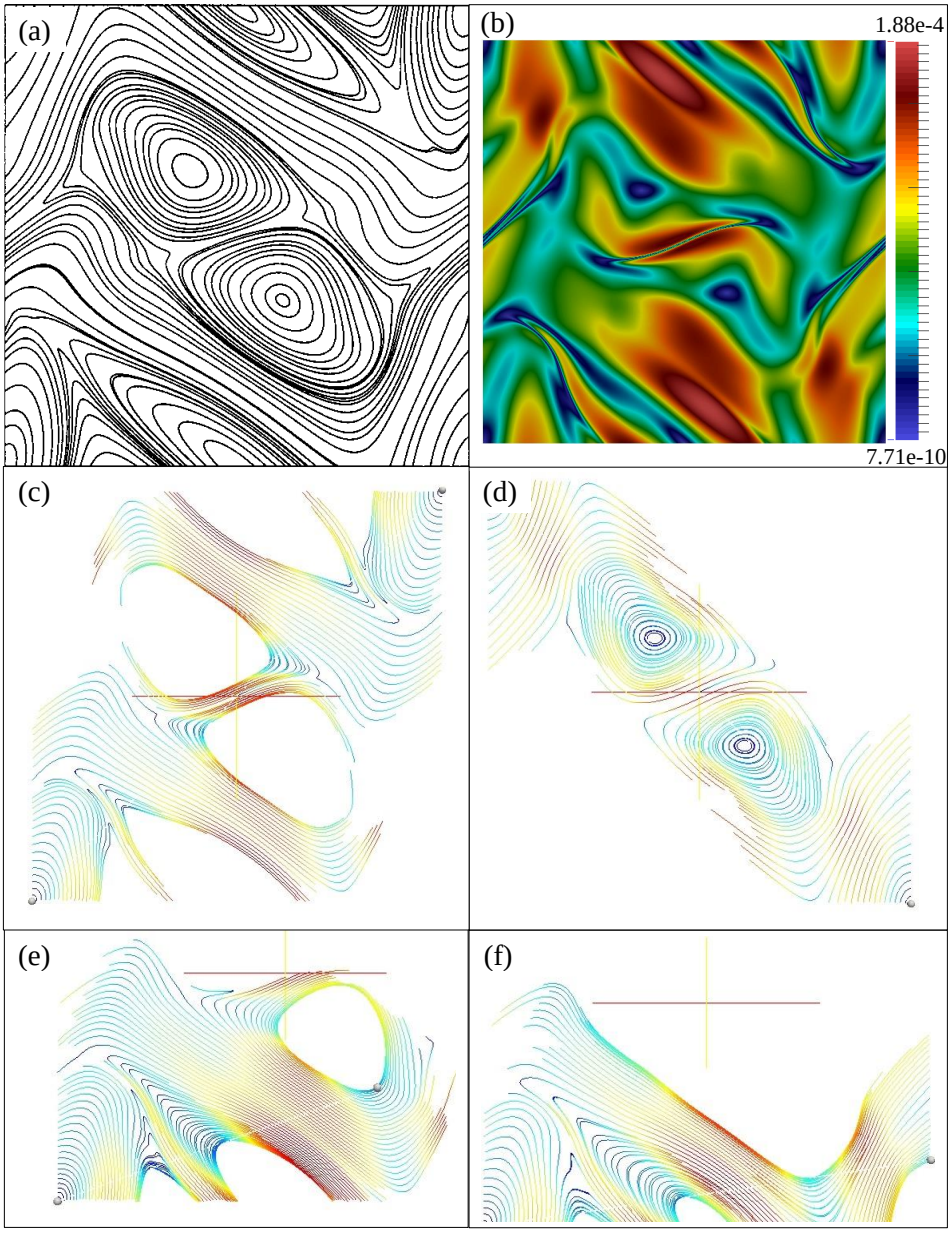

Figure 5.3: Numerical results obtained for the Orszag-Tang vortex at time t = 2 sec. Distribution of magnetic streamlines where double periodic condition is applied. Panel (a) is the magnetic streamlines found in the literature [3]. Panel (b) is the magnitude of the magnetic field (in T) at time t = 2 sec using our code. The other panels are the magnetic streamlines of the Orszag-Tang vortex using our MHD code.

computational domain used is a square of sides $L_x = L_y = 10^5\ m$, and all the four boundaries are periodic. The initial conditions, which do not have any type of discontinuity, being defined as:

$$\rho = 1.67 \times 10^{-11}\ kg/m^3\ ;\ T = 8 \times 10^4\ K\ ;\ p = \rho RT;$$

$$U_x = -V_A sin(2\pi y)\ ;\ U_y = V_A sin(2\pi x)\ ;\ B_x = -B_0 sin(2\pi y)\ ;\ B_y = B_0 sin(4\pi x).$$

Figure (5.3) shows the stream lines of the magnetic field of the plasma at t = 2 sec. As the solution evolves in time, the initial vortex splits into two vortices as shown in the figure. Sharp gradients accumulate and the vortex pattern becomes increasingly complex due to highly non-linear interactions between multiple intermediate shock waves traveling at different speeds. The results compare well with those given in the literature such as [3, 102, 103].

Let us now check out the robustness of the Bpiso method. Figure (5.4) shows us the distribution of the magnetic field along with its divergence ($\vec{\nabla}.\vec{B}$) of the Orszag-Tang vortex at time t = 3.5 sec using our MHD code. Numerical instabilities are noticed when BPISO method is not applied (panel (b)). Moreover, plots of $\vec{\nabla}.\vec{B}$ show 3 or 4 orders of magnitude less in the case where Bpiso method is used (panels (c) and (d)).

5.4 Test Case for MGR

The treatment of MGR using the MHD approach is widespread in the literature. The two test cases mentioned above show good agreement with the literature concerning the dynamics of the MHD flow with and without magnetic field. Nevertheless, before presenting the results of our model, we need to test our code whether it can handle well the MGR process, using the Spitzer resistivity model, or not. For this sake, we have selected one case which was done by Ugai [104] for the Spitzer resistivity model. Ugai assumed a localized resistivity around the

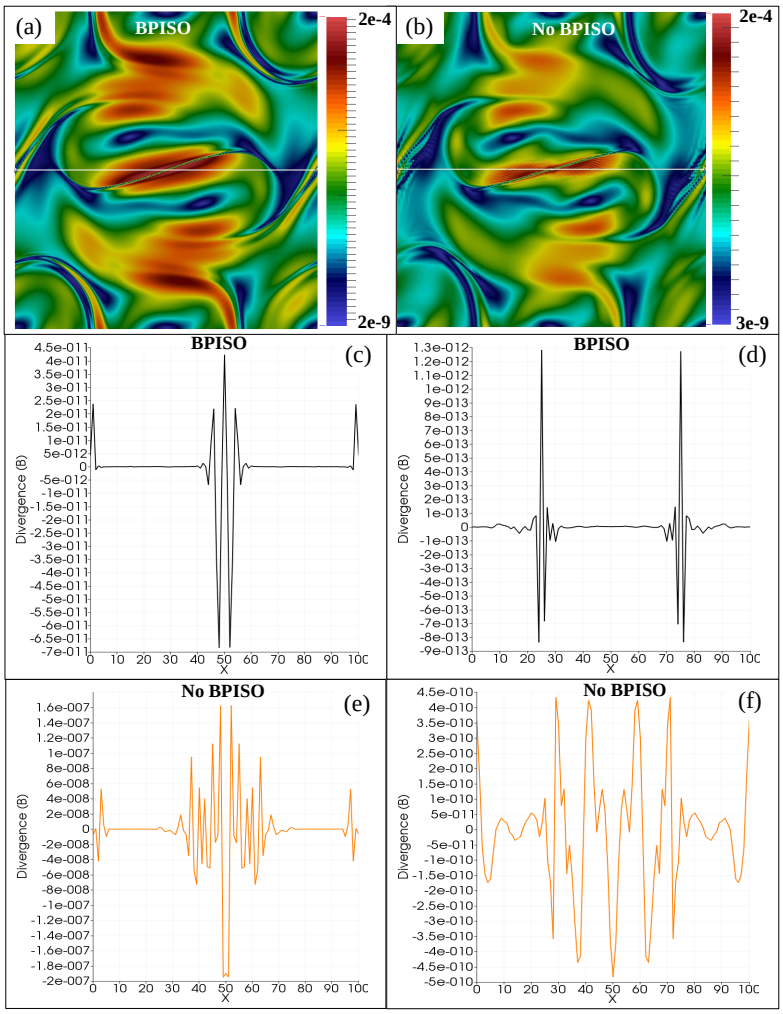

Figure 5.4: Distribution of magnetic field (in T) and its divergence (in T/m) of the Orszag-Tang vortex at time t = 3.5 sec. Panels (a) and (b) are respectively the magnitude of the magnetic field with and without the use of Bpiso method. Panels (c) and (d) are respectively the plots, using Bpiso, of $\vec{\nabla}.\vec{B}$ versus X (in km) over the middle of the computational domain and over the bottom boundary. Panels (e) and (f) are respectively the same plots of $\vec{\nabla}.\vec{B}$ without using Bpiso.

origin ($\vec{r} = \vec{0}$) for $0 < t < 4$ (time is normalized by $0.5\lambda_0/V_A$), which causes MGR as an initial disturbance. Then, he investigated the evolution of the MGR process by applying Spitzer-like resistivity for $t > 4$ using his 3D code. Following his case, we did the same as Ugai, but using our $2D$ code including the effect of the z-components of magnetic field and velocity. The equations for this test case

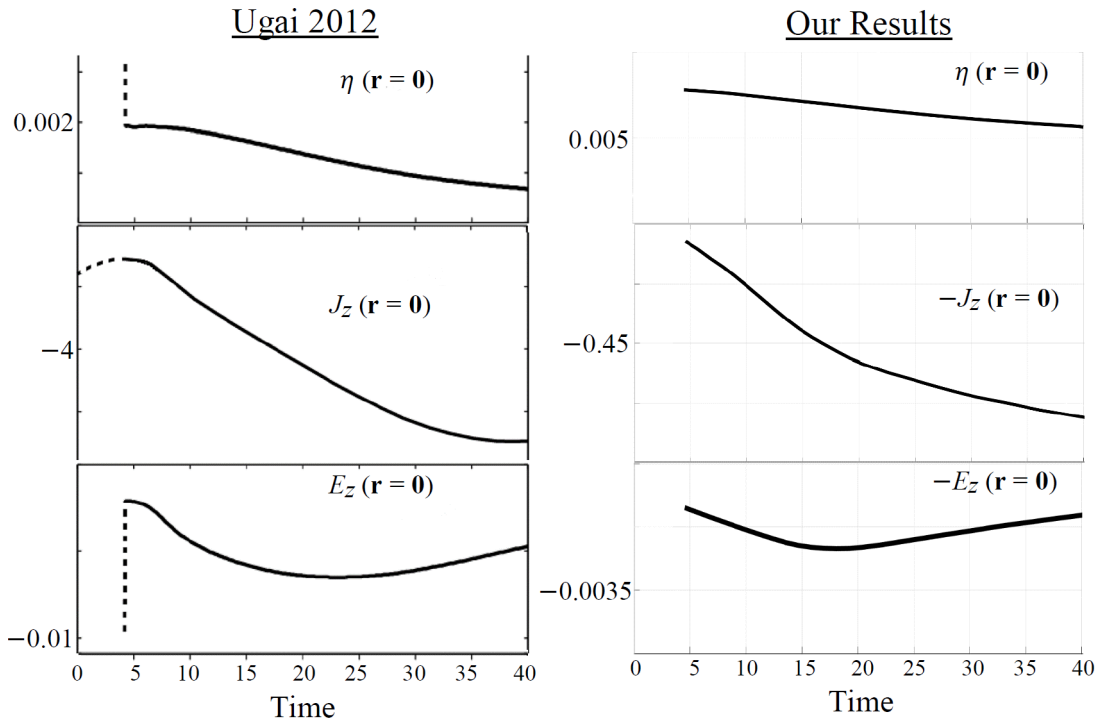

Figure 5.5: Comparison between our results and Ugai's for the case of Spitzer resistivity initiated by localized resistivity around the origin. Ugai set the amplitude of the localized resistivity to 0.02 (normalized by $0.5\mu_0 V_A \lambda_0$), and that of the Spitzer resistivity is set to 0.002. In our results, the amplitudes of the localized and the Spitzer resistivities are respectively set to 0.145 and 0.0145. η, J_Z, E_Z and time are all expressed in normalized units.

are thus our basic equations without fluctuations, i.e. Equation (2.55) to Equation (2.60) without the sources and sinks generated by the fluctuating magnetic field $\vec{B}_F$ ($S = 0$).

Figure (5.5) shows the time evolution of the resistivity η, the z-components of current density J_Z and electric field E_Z at origin, all are expressed in normalized units. Left panels were done by Ugai, and the right panels are the results we got using the Ugai's setup. Note that in Ugai's calculations, J_Z and E_Z are pointed in the negative z-direction. In our calculations, J_Z and E_Z are pointed in the positive z-direction, this is why we plotted $-J_Z$ and $-E_Z$ instead of J_Z and E_Z. It is evident, as Ugai found, that the MGR process does not grow since Spitzer resistivity η and the reconnection rate $|E_Z|$ ($= |\eta J_Z|$) become reduced around the

origin ($\vec{r} = \vec{0}$) at later times. Thus, our results show good agreement with the Ugai's for the Spitzer resistivity model initiated by localized resistivity around the origin. Therefore, we can apply our code for numerically investigating the MGR process using the Spitzer resistivity model.

Chapter 6

Simulation of MGR using the Spitzer Resistivity Model

6.1 Introduction

As outlined in Chapter 1, the coronal magnetic field lines are anchored to the Sun's photosphere at locations called footpoints. Thus, it can be assumed that the solar corona could be affected by magnetic fluctuations initiated by the turbulent motion of these footpoints. Consequently, as discussed in Chapter 2, we add fluctuations to the coronal magnetic field in order to incorporate the effect of the photospheric turbulence on the MGR and heating processes of the solar corona. We start this chapter by describing the functional forms of both the initial coronal magnetic field and the magnetic field fluctuations, which are used for all the runs. Then, in Chapters 6, 7 and 8, we present our results of the MGR cases with and without fluctuations described as follows:

- In Chapter 6 here, we use Spitzer-like form for resistivity η and all the cases start with zero initial velocity.
- In Chapter 7, we present new MGR cases using a uniform resistivity instead of the Spitzer-like one applying the same initial and boundary conditions

as those of Chapter 6.

- In Chapter 8, we show other cases of the MGR process using the same functional form of Spitzer resistivity as in Chapter 6, but we start with initial velocity $\neq 0$ along the outflow direction (y-direction).

The Spitzer resistivity is defined as $\eta = \tilde{\eta} k_\eta T^{-3/2}$ [105], where T is the temperature, k_η is ≈ 356 SI units determined using the plasma parameters of the solar corona [106], and $\tilde{\eta}$ denotes a dimensionless amplification factor equals to 1 for the measured values of resistivity in the solar corona. As justified below under section 6.4.1, we enhance the resistivity by setting $\tilde{\eta} = 5.62 \times 10^8$ in order to keep our calculations valid in the framework of resistive MHD. In other words, for this value of $\tilde{\eta}$, the resistive term $\eta \vec{J}$ dominates the Hall and the inertial terms on the right hand side of the generalized Ohm's law presented before in Chapter 2 by Equation (2.40).

6.2 Treatment of Magnetic Field Fluctuations

This section is an extension of Section 2.7 of Chapter 2. The modified MHD equations, Equation (2.55) to Equation (2.60), represent the basic equations of our model. Recall that the total magnetic field $\vec{B}$ of the corona can be split into three parts, the coronal magnetic fields ($\vec{B}_M$ and B_z) and the magnetic field fluctuations ($\vec{B}_F$), as given before by Equation (2.54). Additionally, we further assume that the fluctuations are static and sinusoidal, and remember that both $\vec{B}_M$ and $\vec{B}_F$ are lying in two-dimensional space, the $(x-y)-$plane, as noted previously in Chapter 2. In order to match the pattern of the anti-parallel coronal field lines between two coronal loops near the photosphere, we choose hyperbolic tangent as initial profile for $\vec{B}_M$. For the fluctuation component, $\vec{B}_F$, we consider

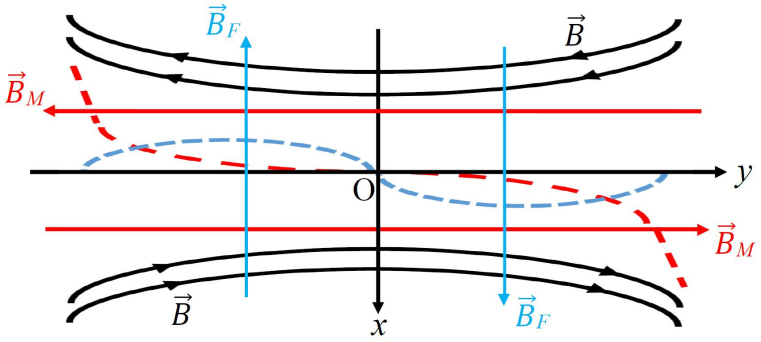

Figure 6.1: Illustration of the space profiles of the coronal mean field $\vec{B}_M$, the magnetic field fluctuations $\vec{B}_F$ and the total field $\vec{B}$ in the $(x-y)-$plane. $\vec{B}_M$ is anti-parallel (hyperbolic tangent), $\vec{B}_F$ is sinusoidal, and the profile of $\vec{B}$ is thus deduced from Equation (2.53).

a time-independent sine wave of the form

$$\vec{B}_F = \tilde{B}\sin(k_y y)\hat{x}, \tag{6.1}$$

where $\tilde{B}$ and k_y are respectively the amplitude and the wavenumber of the magnetic field fluctuations. Figure (6.1) illustrates $\vec{B}_M$, $\vec{B}_F$ and $\vec{B}$ in the $(x-y)-$plane. $\vec{B}_M$ is x-dependent and pointing in the y-direction, whereas $\vec{B}_F$ is y-dependent and pointing in the x-direction. The initial profiles of $\vec{B}_M$ and B_z are given by the force-free Harris sheet [107, 108],

$$\vec{B}_{M(t=0)} = B_0\tanh(x/\lambda_0)\hat{y} \quad ; \quad \vec{B}_{z(t=0)} = \frac{B_0}{\cosh(x/\lambda_0)}\hat{z}, \tag{6.2}$$

where λ_0 is the characteristic half-width of the Harris sheet, and B_0 is the amplitude of the coronal magnetic fields.

We wish to link the wavenumber of B_F to the footpoint motion to have an order of magnitude of k_y. The Alfvén speed, V_A, is the characteristic speed for the magnetic field to reach the solar corona initiated in the sun's photosphere. Moreover, we assume that the dispersion relation $\omega = k_y V_A$ holds, where ω is the angular frequency of the fluctuations. Referring to [109], the average speed

of the footpoint motion is observed to be $\sim$ 1 km/sec and the granular size is $\sim$ 1000 km. Accordingly, the time-scale of this motion is about 1000 sec. However, it is reasonable to assume that fluctuations would occur at a faster rate and that the observed values are rather closer to the average values of the footpoint motion. It is therefore plausible to have values about 100 or even 10 sec, which yields wavelengths $\Lambda_y = 10L_y$ and L_y respectively. L_y is the length of our computational domain as shown in Figure (6.2).

6.3 Numerical Simulation

The equations, Equations (2.55)$-$(2.60) derived previously in Chapter 2, are solved in two dimensional space, the $(x-y)-$plane, in order to simulate the MGR process with and without magnetic fluctuations. We emphasize that, during simulation, the continuity equation, Equation (2.55), is written in terms of the thermal pressure p_{th} using the equation of state $\rho = p_{th}/R_M T$. Moreover, the total energy equation, Equation (2.60), is used to solve for the temperature T, since E_k and E_{mag} are calculated from the velocity and the magnetic field, which are respectively obtained from the momentum and the induction equations, Equations (2.56)$-$(2.59).

6.3.1 Initial and boundary conditions

The same initial conditions are applied for all the runs, with and without magnetic fluctuations. At $t = 0$, we initiate our simulation by setting the fluctuating magnetic field, $\vec{B}_F$, to zero. We use Equation (6.2) as initial conditions for the coronal magnetic field components, $\vec{B}_M$ and B_z, leading to have uniform magnetic pressure at $t = 0$. The plasma fluid velocity is also set to 0. The initial thermal pressure is uniform in the $(x-y)-$plane, and it is thus balanced by the initial magnetic pressure. The initial plasma β is also uniform. By the adequate choice

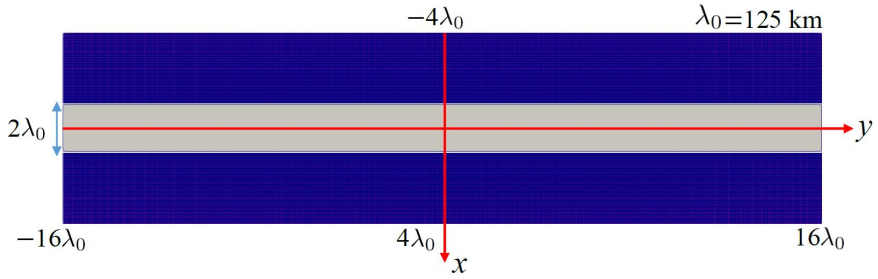

Figure 6.2: We present the mesh of our computational domain in which we perform all the simulation cases. The mesh is two-dimensional lying in the $(x-y)-$plane, where the vertical side is the x-axis and the horizontal side is the y-axis. The gray part specified at the middle represents the initial Harris sheet of width $2\lambda_0$ elongated along the y-direction, and it will be used after in this chapter to present the magnetic field lines at different instants during the simulation.

of the magnetic field, we insure that the coronal plasma $\beta < 1$ initially. We set the initial temperature to be uniform, and by using the equation of state, the initial plasma density is constant.

All the boundaries of the four sides of our computational domain are open. This is done by setting the gradient in the normal direction to be zero for all the plasma quantities at the boundaries.

6.3.2 Numerical setup

The mesh used in our simulation is non-uniform grid spacing, and it has 256-by-512 mesh points. As shown in Figure (6.2), the size of the computational domain is $L_x = 8\lambda_0$ in the x-direction and $L_y = 32\lambda_0$ in the y-direction, where $\lambda_0 (= 125$ km) is the initial half-width of the current sheet. The mesh is refined around its center (around which we expect to have an X-point), and the minimum grid size is $\Delta x \approx \lambda_0/36$ and $\Delta y \approx \lambda_0/18$. The authors in [110] performed MHD simulation using forced reconnection model to study the acceleration of particles in solar flares, and they used uniform grid steps $\Delta x = \Delta y = L_x/128 = \lambda_0/16$.

The typical background magnetic field of the corona, assuming quiet corona,

is chosen to be $B_0 \approx 6$ Gauss [111, 112]. Thus, the initial magnetic pressure is $p_{mag_0} = 0.14$ Pa. The initial plasma β is uniform equals to $\beta_0 = 0.15$. Referring to Equation (1) of [113], the author obtained the plasma β, defined with scaled parameters, for the solar corona to be 0.2. The thermal pressure is $p_{th_0} = \beta_0 p_{mag_0} = 0.021$ Pa. The particle density n of the coronal plasma is $\sim 10^{14}$ or 10^{15} m^{-3} [114, 98] and here we set it $\approx 2 \times 10^{15}$/m^3. The initial plasma density is thus $\rho_0 = n m_{ion} \approx 3.5 \times 10^{-12}$ kg/m^3. The initial temperature is uniform and calculated from the equation of state $T_0 = p_{th_0}/\rho_0 R_M \approx 7.3 \times 10^5$ K. As mentioned in Chapter 2 and discussed here in this chapter, the value of the resistivity is initially enhanced and is set to $\eta_0 \approx 7.26 \times 10^{-3} \mu_0 V_A \lambda_0$ Ω.m. The Alfvén time $\tau_A = L_x/2V_A \approx 1.8$ seconds, and the time-step is set to $\Delta t = 0.05$ sec $\approx \tau_A/36$. We use the open source platform, "openFOAM" [82], to numerically solve the basic equations of our model, Equations (2.55)−(2.60). From the initial conditions described above, the current density $\vec{J}$ is then calculated according to Ampère's law. $\vec{J}$, $\vec{B}_M$ and B_z will generate plasma flows leading to $\vec{u}_{xy}$ and u_z different from 0 according to momentum equations, Equation (2.56) and (2.57). The plasma bulk velocities $\vec{u}_{xy}$ and u_z will affect the plasma density ρ and the thermal pressure p_{th} through the continuity equation and the equation of state. At same time, $\vec{u}_{xy}$, u_z, $\vec{J}$ and the plasma resistivity η will change $\vec{B}_M$ and B_z according to Equations (2.58) and (2.59). Finally, all the plasma quantities ρ, p_{th}, $\vec{u}_{xy}$, u_z, $\vec{B}_M$, B_z, $\vec{J}$, and η influence the temperature T according to Equation (2.60), which in turn leads to update the resistivity η when using the Spitzer resistivity model.

6.3.3 Error of $\vec{\nabla}.\vec{B}$

As discussed in Section 4.2.3 of Chapter 4, we use the BPISO method to reduce the divergence of $\vec{B}$. However, $\vec{\nabla}.\vec{B}$ is still non-zero leading to unphysical behaviors. What we need is a critical value for the error of $\vec{\nabla}.\vec{B}$ below which the

results are acceptable. The estimation of such error is given in [115, 116, 117] by the relation

$$(\vec{\nabla}.\vec{B})_{error} = \frac{\sum_{i=1}^{N} \int_{CV} |(\vec{\nabla}.\vec{B})_i| dV}{\sum_{i=1}^{N} \int_{CV} dV}. \tag{6.3}$$

Equation (6.3) denotes the error measurement to assess the divergence-free constraint for the magnetic field, where N is the number of mesh nodes in the computational domain, and CV is the control volume or mesh element. Equation (6.3) thus estimates the average of $|\vec{\nabla}.\vec{B}|$ over a spatial element CV.

The authors in [117] found that a value of 10^{-6} for $(\vec{\nabla}.\vec{B})_{error}$ (normalized to $\sqrt{\mu_0 \rho_0 a_0^2}/\lambda_0$, where a_0 is a characteristic sound speed) was acceptable, because no large error accumulation from $|\vec{\nabla}.\vec{B}|$ is noticed. In the present work, we consider 10^{-6} ($\sim 10^{-15}$ T/m) as a critical value. Thus, our results are acceptable if $(\vec{\nabla}.\vec{B})_{error}$ does not exceed the order of 10^{-15} T/m.

Next section, we simulate three cases of the MGR process using the Spitzer-

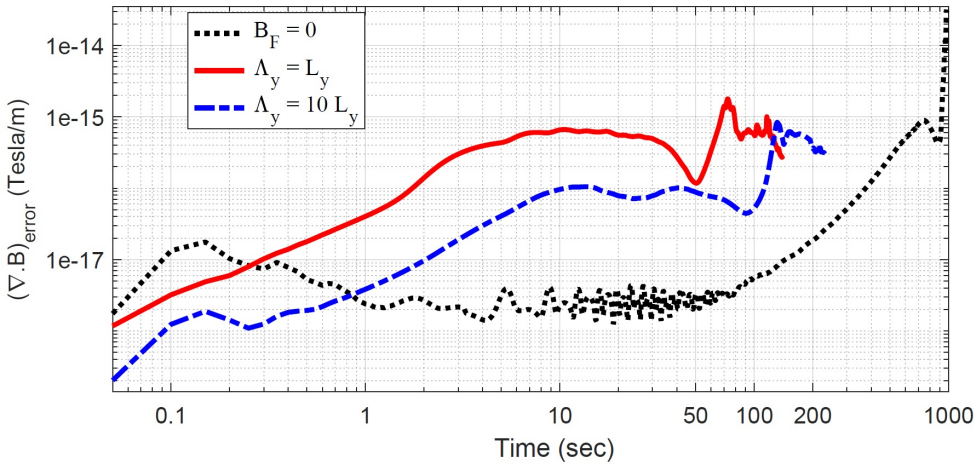

Figure 6.3: We present the temporal evolution of $(\vec{\nabla}.\vec{B})_{error}$ calculated for the three MGR cases using Equation (6.3). The dotted line is for the MGR case without fluctuations ($B_F = 0$). The solid and dashed-dotted lines are for the MGR cases with fluctuations ($B_F \neq 0$) $\Lambda_y = L_y$ and $\Lambda_y = 10L_y$ respectively. Logarithmic scale is used for the two axes and the full process of the MGR is completed within different simulation times for the three cases; 900 sec ($\sim 500\tau_A$) for $B_F = 0$, 230 sec ($\sim 128\tau_A$) and 140 sec ($\sim 78\tau_A$) for $\Lambda_y = 10L_y$ and $\Lambda_y = L_y$ respectively.

like resistivity and starting with zero initial velocity. The first case is performed without magnetic fluctuations, $B_F = 0$. The other two cases are done by adding static magnetic field fluctuations, $B_F \neq 0$, where we set the wavelength of the fluctuations to be $\Lambda_y = 10L_y$ and $\Lambda_y = L_y$ as mentioned previously in Section 6.2. However, before discussing our results and comparing them to previous work, we plot in Figure (6.3) the temporal variation of $(\vec{\nabla}.\vec{B})_{error}$ for the three cases. As shown in the figure, the value of $(\vec{\nabla}.\vec{B})_{error}$ for $B_F = 0$ increases slowly with time up to 900 sec, then it increases rapidly and exceeds the critical value. Thus, hereafter in the next section we consider the temporal evolution up to 900 sec for the case of no fluctuations. Concerning the fluctuation cases, starting with the same initial conditions as those for $B_F = 0$, we also find that $(\vec{\nabla}.\vec{B})_{error}$ does not exceed the order of 10^{-15} T/m during 230 sec for $\Lambda_y = 10L_y$ and 140 sec for $\Lambda_y = L_y$. As we will discover later in the results, the shorter times of the fluctuation cases compared to $B_F = 0$ are attributed to the enhanced process of the MGR due to the addition of the magnetic fluctuations.
We note that the simulation times 900 sec ($\sim 500\tau_A$), 230 sec ($\sim 128\tau_A$) and 140 sec ($\sim 78\tau_A$) are comparable to other numerical methods simulating MGR. The shorter maximum times of the numerical simulation for the fluctuation cases compared to $B_F = 0$ is caused not only by the error on the magnetic field but also by the validity of simulating resistive MHD. In fact, the fast MGR and the consequent jets along with our open boundaries lead to a dramatic decrease in the density, which makes the resistive MHD description inaccurate.

The present approach is illustrated in Figure (6.4) showing two procedures, with fluctuations (on the right) and without fluctuations (on the left). As mentioned in Section 6.2 above, the wavelength of the fluctuations Λ_y is chosen to be $10L_y$ and L_y. Moreover, the amplitude of the fluctuations $\tilde{B}$ is set to 1% of B_0. By comparing the two procedures, we may realize how important the method is based on the fluctuations of the magnetic field, and how they influence the MGR process. It is, after all, intriguing to relate the coronal heating to the dynamics

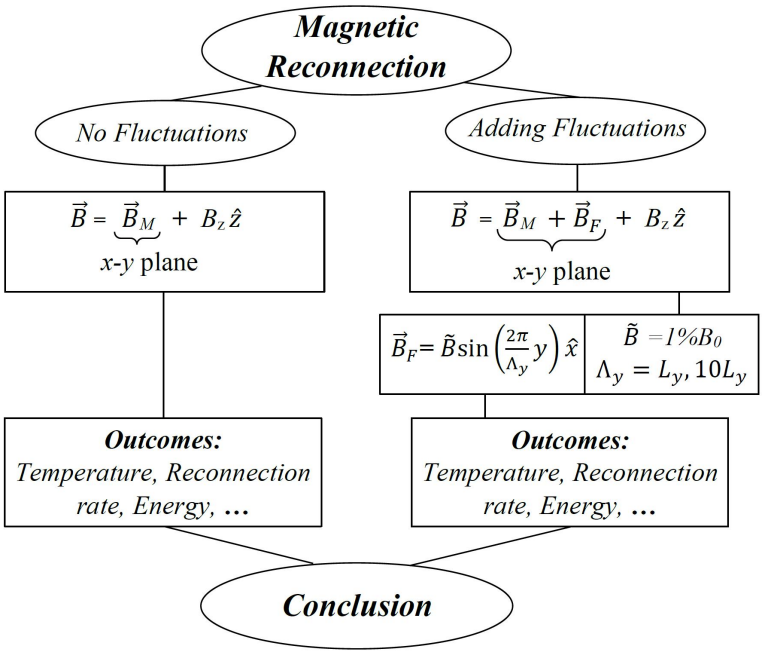

Figure 6.4: A flowchart showing the procedures we follow in treating the MGR process with and without fluctuations.

of the Sun's turbulent photosphere via MGR.

6.4 Results and Discussion

The contribution of the MGR to the heating mechanisms of the solar corona is a fundamental question in solar physics. In what follows in this chapter, we present the results of the MGR process, with and without fluctuations, using a Spitzer-like form for resistivity η defined above under Section 1. The case without fluctuations is compared to other contributions and forms the basis to assess the effects of magnetic field fluctuations when added.

6.4.1 MGR without Magnetic Fluctuations

In this section, we present the results of the MGR process without magnetic fluctuations. Often in the literature, a functional form of resistivity is used to

initiate the MGR followed immediately by resetting it using different models that could depend, or not, on the plasma parameters [73, 118, 104]. We do not follow this path as we set the resistivity to be Spitzer-like and we do not change its temperature dependence functional form in the course of the simulation.

According to the reduced form of Ohm's law, Equation (2.41), we have $\vec{E}+\vec{u}\times\vec{B} = \eta\vec{J}$. Reconnection thus takes place because the frozen-in condition is violated by the term $\eta\vec{J}$. For this reason, it is used to measure the reconnection rate [73] and one can verify that its maximum occurs always in the current sheet. High values of $|\eta J_z|$, $> 0.01 V_A B_0$, is a benchmark of fast reconnection [119]. Another quantity also used to measure the reconnection rate is the inflow Alfvén Mach number $M_A = U_x/V_A$ [24, 23, 120], where U_x is the inflow speed of plasma particles (or field lines) just outside the diffusion region. Note that $M_A \sim |\eta J_z|/V_A B_0$ is a normalized quantity that describes the MGR evolution, and fast MGR is characterized by $M_A > 0.01$.

The generalized Ohm's law normally includes the Hall and the electron pressure terms, i.e. Equation (2.40), which are effective at small scales close to the ion skin depth d_i. The latter is about 5 m in the solar corona for particle density 10^{15} m^{-3} [8]. On the other hand, the Spitzer resistivity in the solar corona is 5.74×10^{-7} Ω.m [106] implying a width of the current sheet of about 2 m. Consequently, the one-fluid MHD description fails at such small scales. To simulate the MGR in the framework of resistive MHD, we artificially increase the Spitzer resistivity by setting $\tilde{\eta}k_\eta = \eta_0 T_0^{3/2} = 2\times 10^{11}$ SI units, where η_0 and T_0 are respectively the initial values of resistivity and temperature given above under Section 6.3.2. In this case, the width of the current sheet becomes about 10 km, which is much greater than d_i, and the resistive term $\eta\vec{J}$ dominates the Hall and electron pressure terms.

The width of the current sheet 2λ is determined from the simulation using the

reduced Ampère's law, Equation (2.32), as

$$2\lambda = 2B_{My}/\mu_0 J_z, \tag{6.4}$$

where B_{My} is the value of the magnetic field in the inflow region near the boundaries at $x = \pm L_x/2$ and J_z is the average value of the current density J_z inside the current sheet. As shown in Figure (6.5), the width of the current sheet 2λ of the

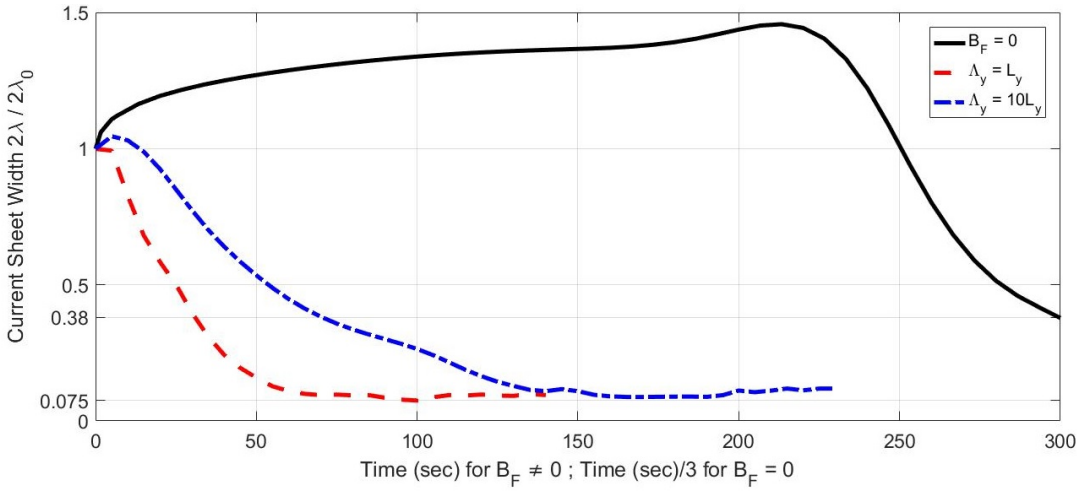

Figure 6.5: We present the current sheet width, calculated using Equation (6.4) and normalized to its initial value $2\lambda_0 = 250$ km, of the three MGR cases with and without B_F. The black solid line is for the case of no fluctuations ($B_F = 0$) with a time step divided by 3 for better visual representation. The red dashed and the blue dashed-dotted lines are for the fluctuation cases $\Lambda_y = L_y$ and $\Lambda_y = 10L_y$ respectively.

three MGR cases is reduced at the end of the simulation time and reaches values which are in the validation scale of the resistive MHD description, $0.38 \sim 100$ km for $B_F = 0$ and $0.075 \sim 20$ km for $B_F \neq 0$. Hereafter, we stop the simulation as we reach values where the resistive MHD description fails.

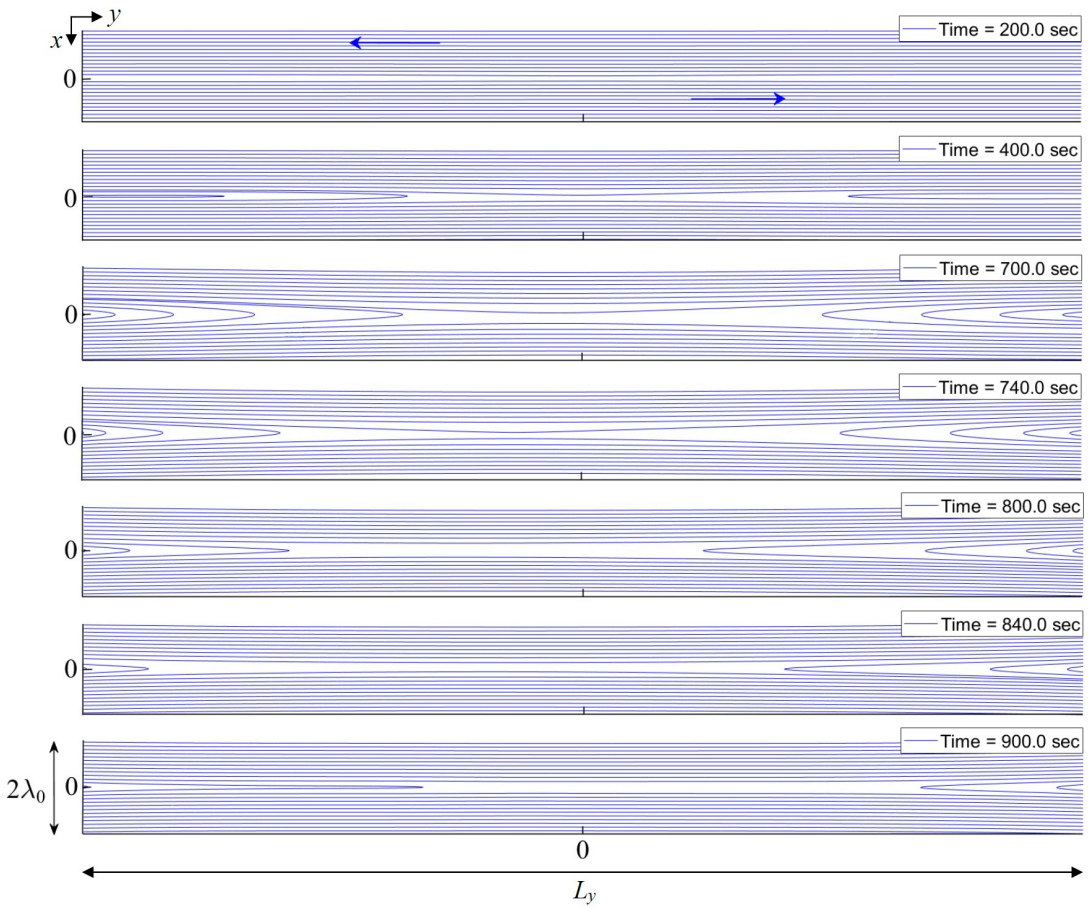

Figure 6.6: The field lines of the coronal magnetic field $\vec{B}_M$ for $B_F = 0$ are presented at different times indicated on the panels. The field lines are shown in the gray part of our computational box of width $2\lambda_0$ specified previously in Figure (6.2). The vertical side represents the x-direction of the mesh for $-\lambda_0 \leq x \leq \lambda_0$, where $\lambda_0 = 125$ km. The horizontal side is the y-direction for $-L_y/2 \leq y \leq L_y/2$, where $L_y = 32\lambda_0$. The arrows shown on the first panel ($t = 200$ sec) indicate the directions of $\vec{B}_M$.

Temporal Behavior of Magnetic Field Lines

Figure (6.6) shows the magnetic field lines at different instants indicated in each panel. The initial profile of the coronal field lines is 'purely' anti-parallel in the y-direction. The reconnection effects start to be visible on the magnetic field lines at 200 sec, then, they become well developed at 700 sec when we observe the X-point almost at the mesh center. After 700 sec, one can notice that the

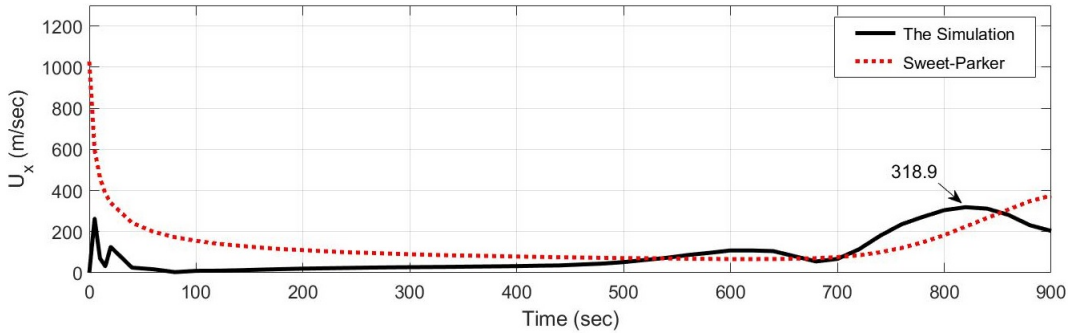

Figure 6.7: The plasma inflow speed U_x for the MGR without magnetic field fluctuations. The solid line represents the inflow speed using the maximum value of u_x just outside the current sheet at $x \sim \lambda$ and $y = 0$. The dotted line is for the inflow speed calculated using Equation (6.5), where η is determined using the spatial average of the Spitzer-like resistivity inside the current sheet for $-\lambda \leq x \leq \lambda$.

field lines start to move away from each other indicating the onset of two outflow jets along the y-direction. The current sheet becomes elongated and appears to behave like the one predicted in the Sweet-Parker reconnection model. According to the latter, the inflow of magnetic field lines in steady-state should balance the diffusion of the field lines in the vicinity of the X-point [6]. The inflow speed is thus related to resistivity η according to

$$U_x = \frac{\eta/\mu_0}{2\lambda}, \tag{6.5}$$

where 2λ is the width of the diffusion region or the current sheet.

Let us assume that Equation (6.5) holds for Spitzer-like resistivity, and we wish to investigate how close the MGR is to the Sweet-Parker model. Figure (6.7) shows the temporal evolution of two inflow speeds, one is calculated using Equation (6.5) and the other is determined using the maximum value of u_x just outside the current sheet at $x \sim \lambda$ and $y = 0$. The width of the current sheet 2λ in Equation (6.5) is determined from the simulation using Equation (6.4). At $t \simeq 0$, the two inflow speeds are different because $\eta \neq 0$ and all the speeds are set to zero.

With increasing time, they tend rapidly to be close indicating an MGR process similar to that described in the Sweet-Parker model even for Spitzer-like resistivity. This result has already been obtained by [121] for a uniform resistivity. They show that sheared magnetic fields undergo Sweet-Parker reconnection at the scales of the resistive MHD. Moreover, as indicated in Figure (6.7), the inflow speed in the simulation reaches ~ 319 m/sec, which corresponds to a reconnection rate $M_A \sim 10^{-3} < 0.01$ indicating a slow reconnection rate in agreement with the Sweet-Parker model.

Characterization of the MGR in the Absence of Magnetic Fluctuations

The MGR is an impulsive process, it takes place locally in the current sheet at relatively small scales before spreading out and affecting the whole spatial simulation domain. In Figure (6.8), we show the time dependence of some of the main physical quantities. The goal is to help us understand the MGR process as it develops over time.

In Figure (6.8-a), we plot the x-component of B_M taken at $x = 0$ and along the current sheet for $y \geq 0$ as a function of time. At $t = 0$, B_{Mx} is equal to zero as the current sheet is only in the y-direction. It increases right after starting the simulation at $t \simeq 0$. Consequently, although this was not evident in the magnetic field lines presented in Figure (6.6), the MGR process starts as early as the numerical simulation caused by the plasma resistivity. The amplitude of B_{Mx} remains rather small up to $t = 600$ sec, after which we detect a strong increase reflecting the spatial expansion of the X-point in agreement with the behavior of the magnetic field lines.

In Figure (6.8-b), we show a three-dimensional plot of the reconnection rate ηJ_z taken at $y = 0$ as a function of x and time. Starting from $t = 0$, ηJ_z decreases sharply leading to a more uniform variation, then it remains almost constant between 200 and 600 sec. After this time, thus for $t > 600$ sec, we observe a

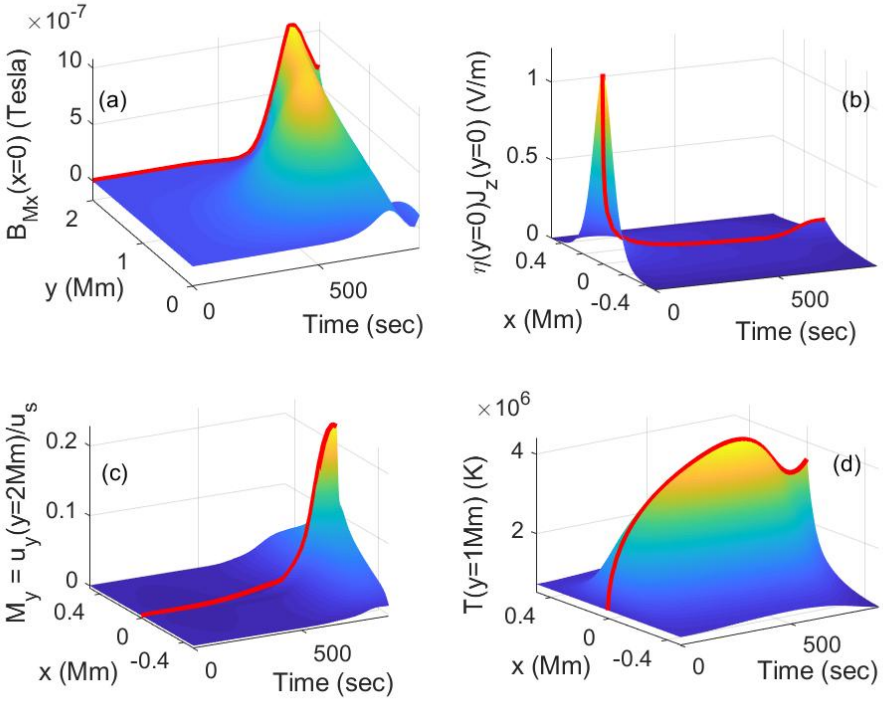

Figure 6.8: We present $3D$ plots showing the temporal and spatial variation of four physical quantities, which are (a) the x-component of the coronal magnetic field B_{Mx} at $x = 0$ and $y > 0$, (b) the reconnection rate ηJ_z at $y = 0$ for all values of x, (c) the Mach number associated with the velocity in the y-direction at $y = 16\lambda_0$ for all x values, and (d) the temperature T at $y = 1$ Mm for all x values. The thick solid curves shown on the $3D$ plots represent the maximum values of the quantities.

slight increase in its value and a regain of non-uniformity around the origin. At $t = 900$ sec, the maximum of ηJ_z reaches a value of $\sim 0.75 \times 10^{-3} V_A B_0$, indicating a slow reconnection rate, which yields an Alfvén Mach number M_A about 10^{-3} consistent with the result discussed above using the inflow speed.

In order to assess the plasma motion during the MGR, we determine the Mach numbers associated with the velocities in the x and y-direction defined respectively as $M_x = u_x/u_s$ and $M_y = u_y/u_s$ where $u_s = \sqrt{\gamma R_M T}$ is the sound speed. Along the current sheet, an outflow takes place because u_y is positive (negative)

for $y > 0$ ($y < 0$) leading to an ejection of the particles out from the computational domain along the y-direction. Not shown here, but we record a modest inflow in the x-direction with a Mach number that is 40 times smaller than that in the y-direction. In Figure (6.8-c), we show a three-dimensional plot of M_y taken at the outflow boundary at $y = 16\lambda_0 = 2$ Mm as a function of x and time. At $t = 0$, M_y is equal to zero as the initial velocity is set to zero, and then it remains small up to $t = 600$ sec after which it increases sharply. This quantifies the convection of the plasma caused by the MGR jets in the y-direction. Consequently, and because all the boundaries are set to be open, the density of the plasma in our computational domain decreases sharply for $t > 600$ sec.

The behavior of the temperature measured at $y = 8\lambda_0 = 1$ Mm as a function of x and time is shown in Figure (6.8-d). The temperature increases as a result of MGR going from the initial temperature of $\sim 7 \times 10^5$ K up to 4×10^6 K for t about 600 sec. Then for $t > 600$ sec, T appears to decrease. This does not reflect a cooling of the plasma inside the computational domain but rather the exit of the hot particles that lie close to the current sheet outside the computational domain by the jets in the y-direction. Consequently, one may safely deduce that the dynamics for $t > 600$ sec is dominated by the jets that eject plasma outside our domain. We note that the reconnection rate, shown in Figure (6.8-b), is consistent with the behavior of temperature in Figure (6.8-d) because the resistivity used is Spitzer-like. This causes the reconnection rate to remain low because of the resistivity decrease in the vicinity of the X-point. This result is in agreement with the work done by [118, 104], despite the difference in the initial conditions as they use a higher amplitude resistivity perturbation to initiate reconnection.

Energy Budget without Magnetic Fluctuations

We now discuss how magnetic energy is distributed during the MGR as a function of time. Initially only the current and the main magnetic field possess spatial

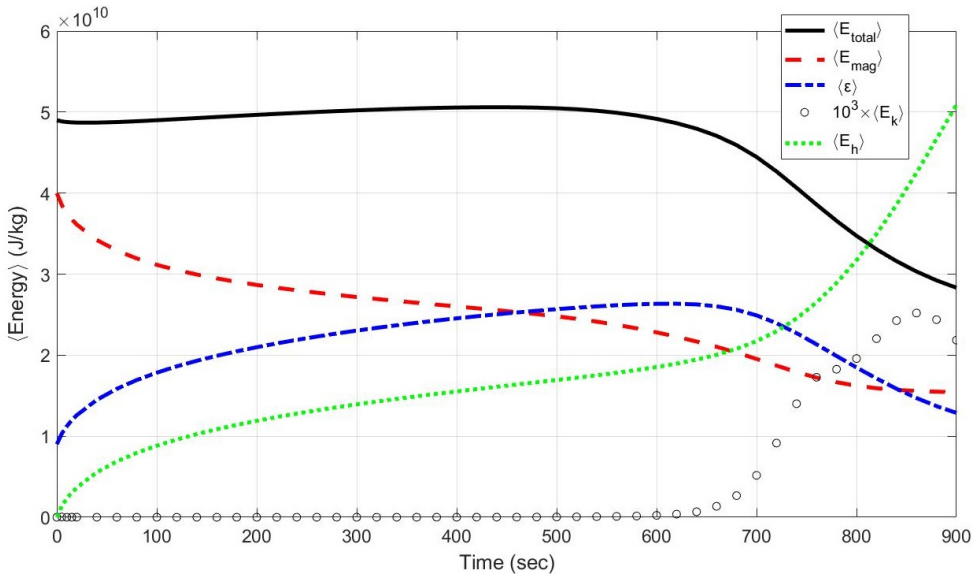

Figure 6.9: The temporal variation of the spatial average of the total energy per unit of mass $\langle E_{total} \rangle$ (solid line), the magnetic energy $\langle E_{mag} \rangle$ (dashed line), the internal energy $\langle \varepsilon \rangle$ (dash-dotted line), the kinetic energy $\langle E_k \rangle$ (circle) multiplied by 1000, and the heat energy $\langle E_h \rangle$ (dots).

variation. The spatial average of any form of energy E per unit mass is calculated as $\langle E \rangle = \langle \rho E \rangle / \langle \rho \rangle$. Figure (6.9) shows the temporal evolution of the total energy $\langle E_{total} \rangle$, and its components that are the kinetic energy $\langle E_k \rangle$, the magnetic energy $\langle E_{mag} \rangle$ and the internal energy $\langle \varepsilon \rangle$ per unit mass. Figure (6.9) also shows the temporal variation of the ohmic heating energy per unit mass, $\langle E_h \rangle = \int \langle \eta J_z^2 \rangle dt / \langle \rho \rangle$. The total energy remains almost constant up to ~ 600 sec after which it decreases. We find that the kinetic energy is small when compared to the other forms and for this reason in Figure (6.9) it is multiplied by a factor of 1000. The magnetic energy decrease is monotonous indicating its persistent conversion to other forms of energy during the MGR evolution. This causes the heat and internal energy to increase almost at the same rate up to $t \sim 600$ sec. Starting from $t \sim 600$ sec, the internal energy starts to decrease, while the heat energy continues to increase but at a faster rate. This abrupt change of both the heat and the internal energy right after $t \sim 600$ sec is strongly related to

the deficit of hot particles within the current sheet. For $t > 600$ sec, the plasma dynamics are dominated by the jets that expel plasma particles and lead to a decrease in both the plasma density and temperature. The decrease in the total, as well as the internal energy, indicates that the ohmic heating is not enough to compensate for the hot plasma expulsion by the jets. The plasma particles at relatively low temperatures come into the current sheet as inflow. After they are heated up by the MGR process, the particles leave the domain along with the jets as an outflow. Thus, the plasma particles carry the heat generated by the MGR to regions that are far from the X-point. Accordingly, the MGR jets generate non-local heating along the magnetic field lines far from the X-point location.
In this section, we studied the MGR using Spitzer-like resistivity without starting with a functional form of resistivity perturbation to initiate reconnection. We found that the reconnection rate (ηJ_z) decreases with time and it has low values indicating a slow MGR process. Thus, an additional ingredient is required to speed up the MGR process. As outlined in the Introduction section, the fast MGR process was investigated first by Petschek, and later on by other authors using various approaches such as resistivity enhancement [122, 123], anomalous resistivity [29, 72], Hall MHD [31]. Hereafter, we add time-independent magnetic fluctuations with a small amplitude and long wavelength to the coronal magnetic field to show that this is sufficient to trigger fast reconnection.

6.4.2 MGR with Time-Independent Magnetic Fluctuations

In this section, we discuss the results of the numerical simulation of the MGR with magnetic fluctuations using the same initial and boundary conditions as the case with $B_F = 0$. We recall that the magnetic field is composed of $\vec{B}_M$ and B_z that evolve as a function of time and space according to Equations (2.58) and (2.59). The additional magnetic field $\vec{B}_F$ that accounts for the footpoint motion

is applied at $t > 0$ and retained unmodified during the simulation. Our approach differs from that of the "forced reconnection model" in which a perturbation of the initially stationary force-free Harris sheet is introduced, at an initial time interval, via external boundary deformation [124, 125, 126, 127].

The basic idea is that the sources of $\vec{B}_F = \tilde{B}\sin(2\pi y/\Lambda_y)\hat{x}$ (see Figure 6.1) lie outside the simulation domain. Consequently, B_F is imposed on the magnetic field in the simulated region without being affected by its dynamics. We set the amplitude of the fluctuations $\tilde{B}$ to be as low as 1% of B_0. We emphasize that the numerical simulation is not restricted to time-independent magnetic fluctuations.

The Magnetic Field Configuration with Fluctuations

In this section, we discuss the results of the MGR with magnetic fluctuations obtained for two cases $\Lambda_y = 10L_y$ and $\Lambda_y = L_y$. The values of Λ_y are chosen such that Λ_y/V_A is of the same order as the time-scales of the photospheric footpoint motion. We use the same functional form of the Spitzer-like resistivity used above for the MGR case without fluctuations.

Figure (6.10) displays the field lines of the coronal magnetic field $\vec{B}_M$ at different times for the two-fluctuation cases $\Lambda_y = 10L_y$ in (a) and $\Lambda_y = L_y$ in (b). It is remarkable that the addition of static magnetic field fluctuations, even with an amplitude of 1% of B_0, has strong effects on the magnetic field evolution. In Figure (6.10-a), we report the onset of a plasmoid, which exists in the region between two X-points in the simulation domain, early in the simulation at $t =$ 50 sec. At $t = 120$ sec, another X-point is formed around the origin causing the formation of two plasmoids on both sides. Then, they move in the opposite y-direction leading to a decrease of the current sheet width with time. Plasmoids are not detected in the absence of magnetic fluctuations.

From the magnetic field configuration with $\Lambda_y = L_y$, as shown in Figure (6.10-b), we note that the formation of plasmoids occurs at a faster rate than for

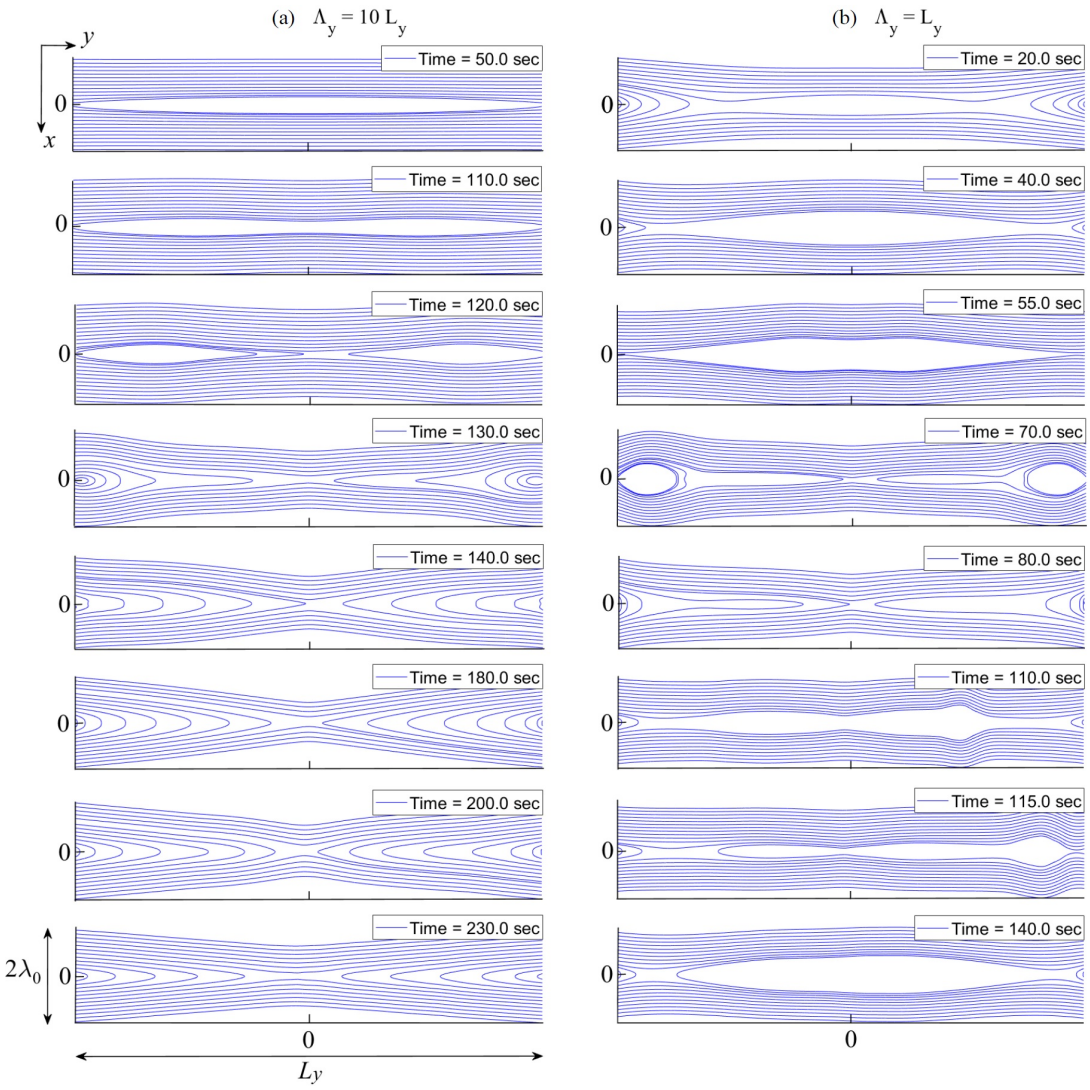

Figure 6.10: On the left side (a) and right side (b), we show respectively the magnetic field lines of B_M for the two MGR cases with magnetic fluctuations, $\Lambda_y = 10L_y$ and $\Lambda_y = L_y$. The different times indicated on the panels show the instants when these plots are calculated. The vertical axis (x-axis) is doubled relative to the horizontal axis (y-axis) for visualization purposes.

$\Lambda_y = 10L_y$. The onset of the first plasmoid is detected at $t = 20$ sec (50 sec for $\Lambda_y = 10L_y$) and is followed by an X-point around the origin. This leads to the formation of two plasmoids at 70 sec similar to what is observed at $t = 130$ sec for $\Lambda_y = 10L_y$. For $t \geq 80$ sec, we witness the generation of a third plasmoid

near the center, which is rapidly ejected in the positive y-direction leading to a strong asymmetry in the plasma motion not detected in the two cases studied above. For $t > 110$ sec, we report a rather complex magnetic configuration. The formation of plasmoids followed by convection away from the X-point has been also detected by [73] using anomalous resistivity. The formation and ejection of the plasmoid in the current sheet would then be attributed to the nature of fast magnetic reconnection [128].

The Onset of Jets

The convective motion of the plasma occurs mainly in the outflow directions along the y-axis. For $B_F = 0$, the onset of the jets is detected about 600 sec, after reconnection takes place. With $B_F \neq 0$, this process occurs at a much faster rate. This issue and its consequences are investigated in this section. Figure (6.11-a) shows the time evolution of the maximum of the Mach number in the y-direction for the three MGR cases as a function of time. The dotted curve is the same solid curve shown previously on the three-dimensional plot in Figure (6.8-c). We recall that Max(M_y) starts to increase at $t > 600$ sec for $B_F = 0$ and is accompanied by an important density decrease caused by the open boundary conditions of our simulation. The behavior of M_y for the two cases with magnetic fluctuations indicates an early development of the jets where the strong increase is reported at $t = 110$ and 50 sec for $\Lambda_y = 10L_y$ and $\Lambda_y = L_y$ respectively. Moreover, the ejection of the plasma by the jets occurs not only earlier but also faster as it can be deduced from the slope of Max(M_y) as a function of time. Moreover, adding magnetic fluctuations leads to values of the Mach number that is 6 times the maximum values reached at $B_F = 0$.

The jets lead to a strong decrease of the plasma density as shown in Figure (6.11-b) where we plot the time dependence of the spatial average of the density $\langle\rho\rangle$ for the three MGR cases with and without fluctuations. We recall that the three

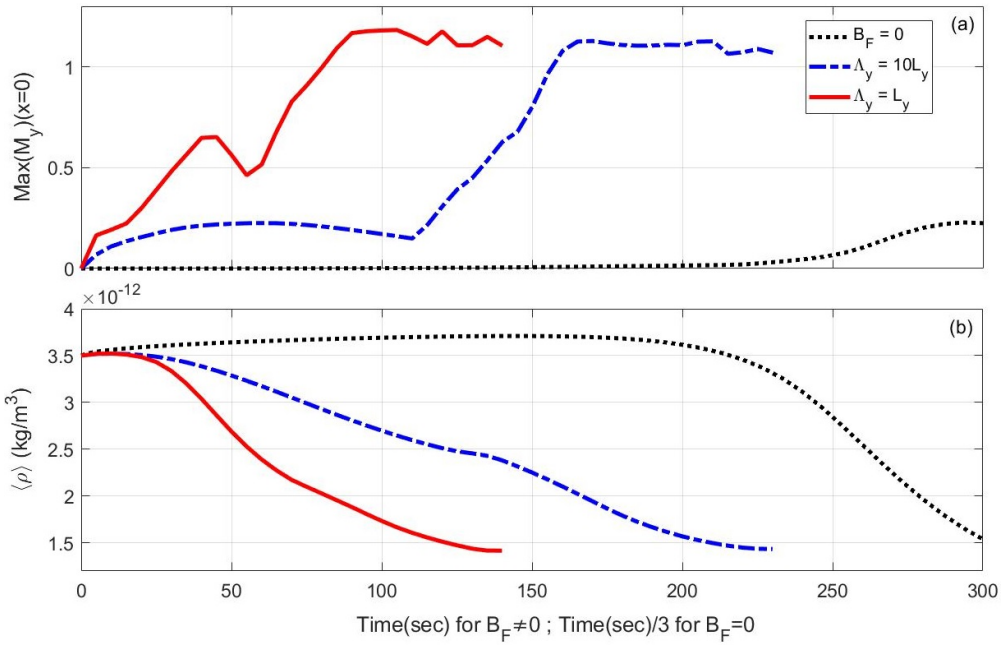

Figure 6.11: We show in (a) and (b) respectively the time dependence of the maximum of the Mach number associated with the velocity in the y-direction Max(M_y) and the mean plasma density $\langle\rho\rangle$ for the three MGR cases. The black dotted line is for the case of no fluctuations ($B_F = 0$) with a time step divided by 3 for better visual representation. The dashed-dotted and solid lines are for $\Lambda_y = 10L_y$ and $\Lambda_y = L_y$ respectively.

cases have the same initial conditions including the same $\langle\rho\rangle$. Initially, we record a density increase similar to the results for $B_F = 0$ caused by the influx of plasma in the x-direction. But this rise occurs for a brief amount of time when including the magnetic fluctuations, that is, about 20 sec. After this time, we report a sharp decrease in the average density at the same time M_y increases. The rates of this decrease are higher for $\Lambda_y = L_y$ than for $\Lambda_y = 10L_y$ also in agreement with the Mach number behavior. We stop the simulation just before the resistive MHD description starts to fail and other effects, such as Hall-MHD, need to be included in the physical model.

Effects on the Temperature and Reconnection Rate

The main goal of this section is to focus on characterizing the behavior of the reconnection rate and temperature when the magnetic fluctuations are added. In Figure (6.12), we show the temporal variation of the maxima of the magnetic field x-component, Max(B_{Mx}), the reconnection rate, Max(ηJ_z), the Alfvén Mach number, M_A, and the plasma temperature, Max(T), for the three MGR cases. Note that for clarity, the time increment for the case with $B_F = 0$ is 1/3 sec and not 1 sec as it is the case for $B_F \neq 0$. The maxima are taken along the y-direction at $x = 0$ because the motion of the X-points and the plasmoids take place in this direction. The dotted curves for $B_F = 0$ in panels (a), (b), and (d) are the same plots shown in Figure (6.8). Figure (6.12-a) shows the amplitude of B_{Mx} as a function of time for the three cases. One can verify that at $t \simeq 0$ sec, the values of B_{Mx} for the three cases are different from 0 reflecting the effect of resistivity on the magnetic reconnection. For $B_F \neq 0$ and $\Lambda_y = 10L_y$, B_{Mx} reaches 6.4×10^{-6} Tesla, that is 6.4 times Max(B_{Mx}) for $B_F = 0$, that scores 1×10^{-6} Tesla. Moreover, this increase is reached after only 150 sec, much earlier than without fluctuations, which takes up to $t = 800$ sec to reach maximum value. When Λ_y is decreased to become equals to L_y, the amplitude of B_{Mx} increases even more up to 2×10^{-5} Tesla in only 65 sec. The variation in the amplitude of B_{Mx} with time is caused by the existence of plasmoids with position changing with time. We deduce that the addition of a static B_F leads to a faster and stronger increase in the x-component of the coronal magnetic field $\vec{B}_M$.

The maximum value of the reconnection rate ηJ_z is plotted in Figure (6.12-b) as a function of time. In agreement with the behavior of Max(B_{Mx}), we note the rapid increase of the reconnection rate to values about 1.1 V/m for $B_F \neq 0$, which is 10 times greater than for $B_F = 0$. The time needed for the reconnection rate to reach its maximum value is about $t = 900$ sec for $B_F = 0$. This time decreases to 150 sec for $\Lambda_y = 10L_y$ and down to 100 sec for $\Lambda_y = L_y$. This also

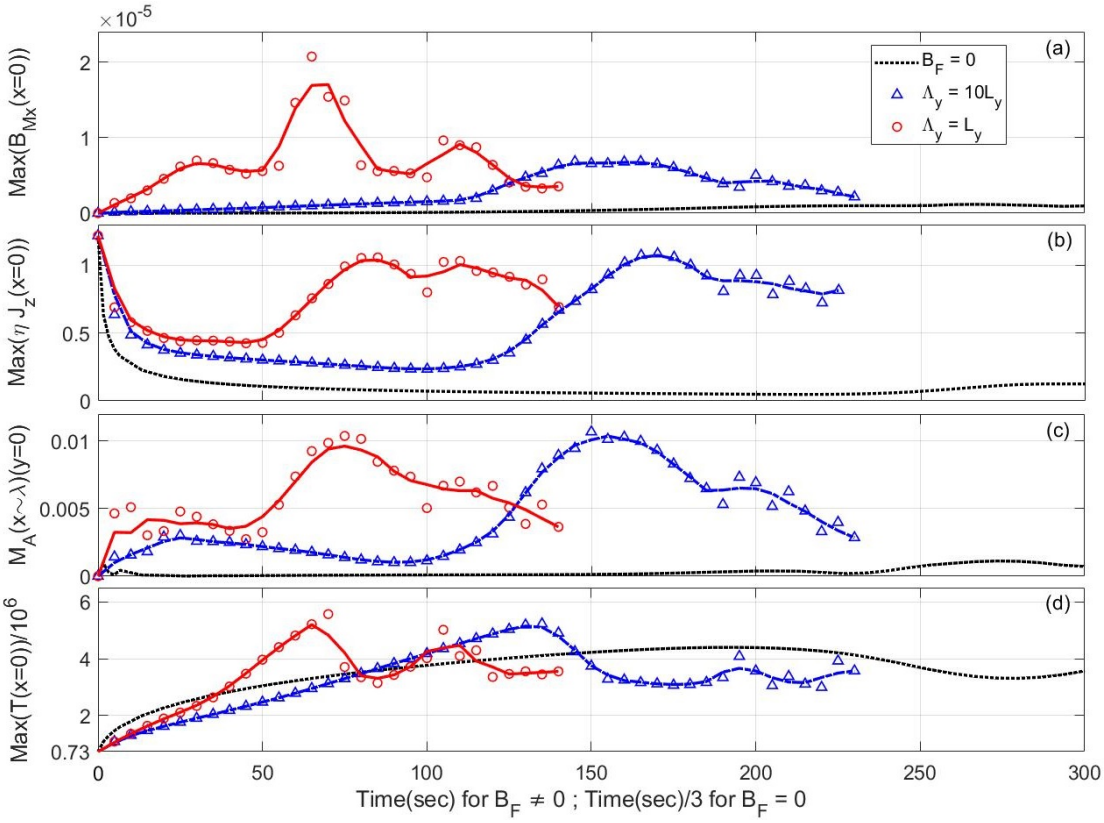

Figure 6.12: We show in (a), (b) and (d) the temporal variation of the maximum value in the y-direction at $x = 0$ of B_{Mx}, ηJ_z and T respectively. We also show in (c) the inflow Alfvén Mach number M_A calculated using the maximum of u_x just outside the current sheet at $x \sim \lambda$ and $y = 0$. The black dotted lines are for $B_F = 0$ with a time step set to 1/3 sec for clarity. The blue triangles and red circles correspond respectively to $\Lambda_y = 10L_y$ and $\Lambda_y = L_y$.

clearly indicates that MGR occurs much faster. Another way to investigate the reconnection rate is to show the behavior of the inflow Alfvén Mach number M_A as a function of time. Figure (6.12-c) shows the time dependence of M_A for the three MGR cases. In agreement with the evolution of Max(ηJ_z), with magnetic fluctuations, M_A increases to reach values greater than 0.01. The latter is often taken to be the fast reconnection threshold [119]. Furthermore, fast reconnection occurs in a period of about 150 sec for $\Lambda_y = 10L_y$ and about 100 sec for $\Lambda_y = L_y$. The two values are much smaller than the 900 sec obtained for $B_F = 0$. The

MGR process is therefore enhanced after including the static magnetic fluctuations.

One of the motivations of this work is to help us understand the abnormally high temperatures recorded in the solar corona. It is admitted that the conversion of the magnetic energy to thermal is a mean to increase the plasma temperature in this region. Here, we aim at investigating the effects of adding time-independent magnetic field fluctuations on the temperature. The three simulations have the same plasma initial conditions and namely the same initial temperature. Figure (6.12-d) shows that by adding magnetic fluctuations with an amplitude of $1\%B_0$, Max(T) reaches a value of $\sim 5.5 \times 10^6$ K, which is an increase of 40% when compared to the case with $B_F = 0$. The case of $\Lambda_y = L_y$ shows further a faster increase of Max(T) compared to the case of $\Lambda_y = 10L_y$ indicating the rate of increase of the temperature increases with decreasing wavelength. The increase in temperature is competing with the convection by the jets of plasma particles outside the simulation domain. Once the jets start emptying the simulation domain from primarily hot plasma, it causes the temperature to drop. This is detected to occur at 150 and 100 sec for $\Lambda_y = 10L_y$ and $\Lambda_y = L_y$ respectively. We conclude that by adding time-independent magnetic fluctuations, we showed that the magnetic reconnection is faster and the temperatures are higher even with a small amplitude of the fluctuations.

Energy Budget with Fluctuations

Before concluding, we turn into investigating the energy budget in the presence of the time-independent magnetic fluctuations with an amplitude equals to $1\%B_0$. Figure (6.13) exhibits the time dependence of the average total energy, $\langle E_{total} \rangle$, the average magnetic energy, $\langle E_{mag} \rangle$, the average internal energy, $\langle \varepsilon \rangle$, the average kinetic energy, $\langle E_k \rangle$ and the ohmic heating average energy $\langle E_h \rangle$ for $\Lambda_y = 10L_y$. The overall behavior of the different energies with fluctuations is similar to the

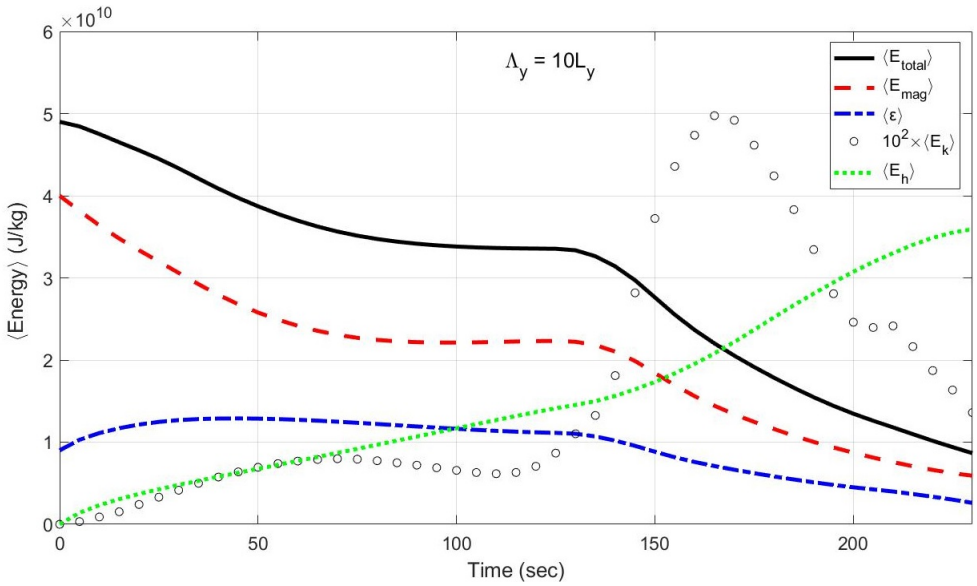

Figure 6.13: The energy budget for the fluctuation case with amplitude $\tilde{B} = 1\%B_0$ and wavelength $\Lambda_y = 10L_y$. The total energy $\langle E_{total} \rangle$ is in solid line, the magnetic energy $\langle E_{mag} \rangle$ is in dashed line, the thermal energy $\langle \varepsilon \rangle$ is in dashed-dotted line, the kinetic energy $\langle E_k \rangle$ multiplied by 100 is in black circles, and the ohmic heating $\langle E_h \rangle$ is in dotted line.

no-fluctuation case for $t > 600$ sec. The main difference between the case with and without fluctuations is the onset of jets much earlier in the simulation. Magnetic energy is still converted into internal energy but the effect of convection is important from $t = 0$ and is reflected in the decrease in the total energy. Convection becomes more important for $t > 150$ sec where the kinetic energy increases dramatically and the total energy decreases even further. The average kinetic energy, $\langle E_k \rangle$, is approximately 14 times greater with B_F than without. The internal and the heat energy, $\langle \varepsilon \rangle$ and $\langle E_h \rangle$, do not reach values as high as those for $B_F = 0$. This is because the amount of the heat generated rapidly leaves the simulation domain with the expelled hot particles due to the early development of high-speed jets in the current sheet.

Chapter 7

Simulation of MGR using the Uniform Resistivity Model

7.1 Introduction

Dissipation mechanisms due to plasma microscopic properties, such as Coulomb collisions and micro-instabilities, may lead to an enhanced resistivity [129, 130], which may be high enough to accelerate the MGR process. A basic question for the reconnection problem may thus be to determine which microscopic effects give rise to an effective resistivity in the diffusion region [129]. The plasma microscopic behaviors should be fully examined in connection with the self-consistent macroscopic reconnection flows. Thus, a resistivity may be given as a function of macroscopic quantities without referring to any detail of the microscopic mechanisms causing effective resistivity [131]. For example, in the MHD formulation which deals with macroscopic plasma behaviors, we use either a Spitzer-like form for the resistivity η (relating resistivity to temperature T and other plasma quantities) describing the Coulomb collisions, or a current-driven anomalous resistivity (relating resistivity to current density J and other quantities) for the micro-instabilities that would take place in the current sheet [132, 133, 134, 135].

Actual plasma systems, such as space and laboratory, are characterized by high-temperature plasmas leading to extremely small electrical resistivity due to Coulomb collisions. This is why we used in Chapter 6 an enhanced form of Spitzer-like resistivity to keep our calculations valid in the framework of MHD as discussed before.

Most of the conventional theoretical studies have considered that MGR should not be influenced by the effective resistivity form, so that the uniform resistivity model has often been employed [119]. Although uniform resistivity is not realistic in actual plasma systems [104], but it is important to (1) examine its effect on the evolution of the MGR process and (2) to compare its results to those obtained using the Spitzer resistivity model.

7.2 Results and Discussion

In this chapter, we simulate new cases of the MGR process with and without fluctuations using the uniform resistivity model, where the resistivity η is assumed to be uniform in space and constant in time. The value of this uniform resistivity is chosen to be the same initial value of the Spitzer-like form used previously in Chapter 6, i.e. $\eta = \eta_0 \approx 7.26 \times 10^{-3} \mu_0 V_A \lambda_0$ Ω.m. We emphasize that the same initial and boundary conditions, that are used in Chapter 6, are applied here for the new MGR cases and we use the same mesh as before.

Before discussing the new results and comparing them to those of Chapter 6, we plot in Figure (7.1) the temporal variation of $(\vec{\nabla}.\vec{B})_{error}$ for the two cases. We find that $(\vec{\nabla}.\vec{B})_{error}$ for the two cases, with and without B_F, does not exceed the critical value for long simulation time of 1000 sec or $556\tau_A$. Thus, hereafter in the next sections we consider the temporal evolution up to 1000 sec for both cases.

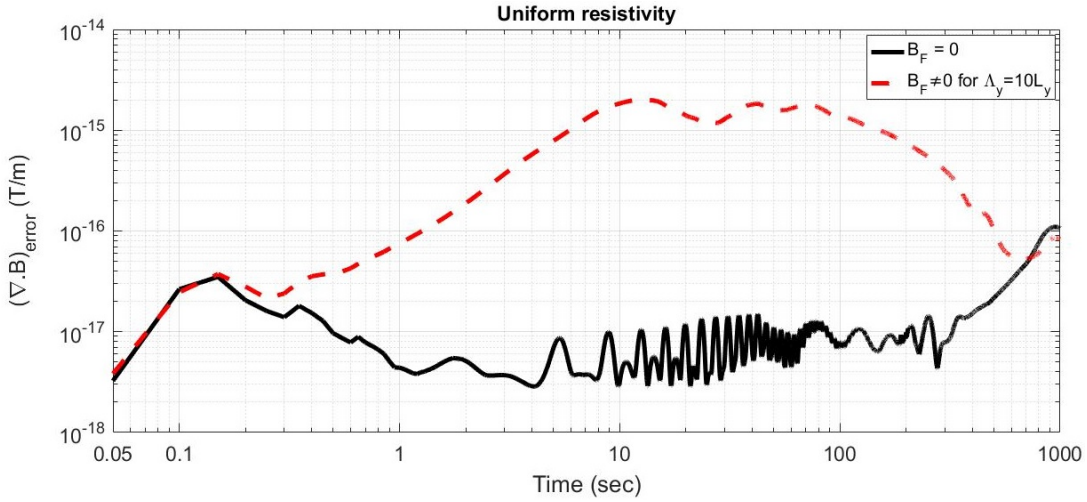

Figure 7.1: We present the temporal evolution of $(\vec{\nabla}.\vec{B})_{error}$ for the two new cases of the MGR process. The black solid line is for the MGR case without fluctuations ($B_F = 0$). The red dashed line is for the MGR case with fluctuations ($B_F \neq 0$) for $\Lambda_y = 10L_y$. Logarithmic scale is also used for the two axes.

7.2.1 Temporal Behavior of Magnetic Field Lines

Figure (7.2) displays the field lines of the coronal magnetic field $\vec{B}_M$ at different times for the MGR cases using constant resistivity without B_F (left panels) and with B_F for $\Lambda_y = 10L_y$ (right panels). In the case without B_F, we report the onset of a large plasmoid at $t > 200$ sec, which exists between two X-points that are outside the simulation box. Later, during the simulation time up to 1000 sec, the plasmoid is enlarged in the x-direction indicating an increase in the current sheet width, which was $2\lambda_0$ at $t = 0$. When fluctuations are added, we denote similar evolution of the magnetic field lines as in the case without fluctuations but at a faster rate. In other words, the behavior of the field lines observed at $t = 1000$ sec for $B_F = 0$ is similar to that observed for $B_F \neq 0$ at $t = 500$ sec. We emphasize that the case without B_F does not show any X-point inside the simulation box, and the case with B_F does not lead to the formation of multiple X-points and plasmoids as it was reported previously in the MGR cases using the Spitzer resistivity model (Chapter 6).

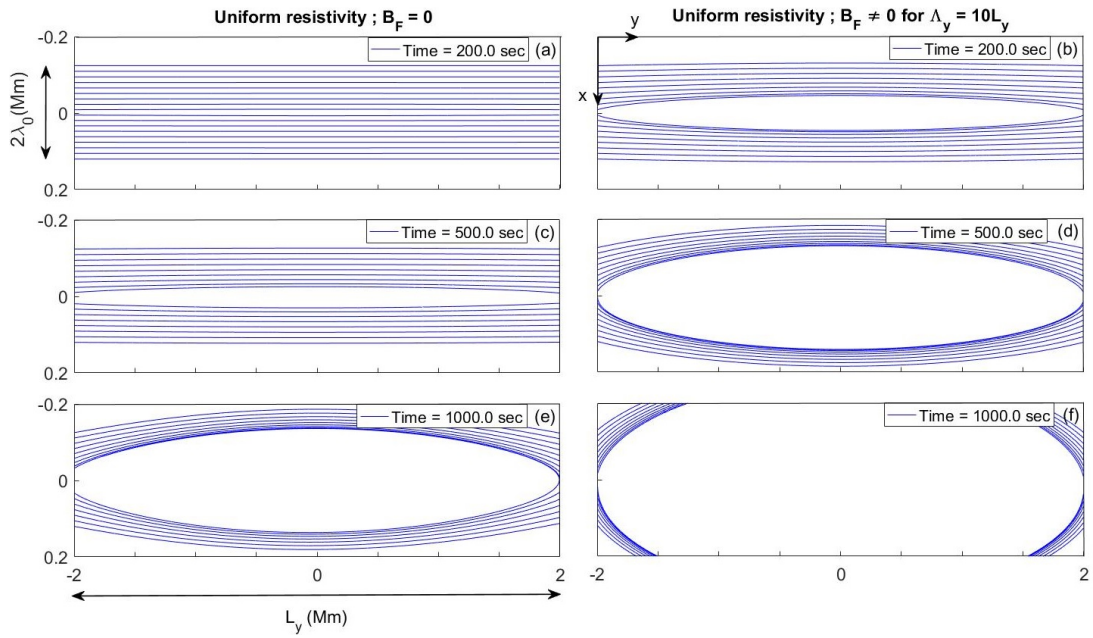

Figure 7.2: We present the magnetic field lines of B_M for the new MGR cases using the uniform resistivity model at different instants. Left panels (a), (c) and (e) are for the case without B_F, while right panels (b), (d) and (f) refer to the case with B_F for $\Lambda_y = 10L_y$. The horizontal side is the y-direction for $-L_y/2 \leq y \leq L_y/2$ and the vertical side is the x-direction for $-L_x/5 \leq x \leq L_x/5$, where $L_y = 4L_x = 32\lambda_0 = 4$ Mm. The x-axis is doubled relative to the y-axis for visualization purposes.

We show in Figure (7.3) the time evolution of the current sheet width 2λ, calculated using Equation (6.4), for the MGR cases using either the Spitzer or the uniform resistivity models with and without B_F. Starting from its initial value of $2\lambda_0$, the sheet width for both the MGR cases, with and without B_F, using the uniform resistivity model increases then decreases but its value at $t =$ 1000 sec is still high, which is greater than twice of $2\lambda_0$. This is in agreement with the behaviors of the field lines observed in Figure (7.2) where X-points do not exist because the sheet width becomes very thick at the center of the domain. Moreover, as noted previously in Chapter 6 as well as in Figure (7.3) here, the MGR cases using the Spitzer-like resistivity exhibit a decrease in the current sheet width below $2\lambda_0$ indicating the formation of the X-point around the origin.

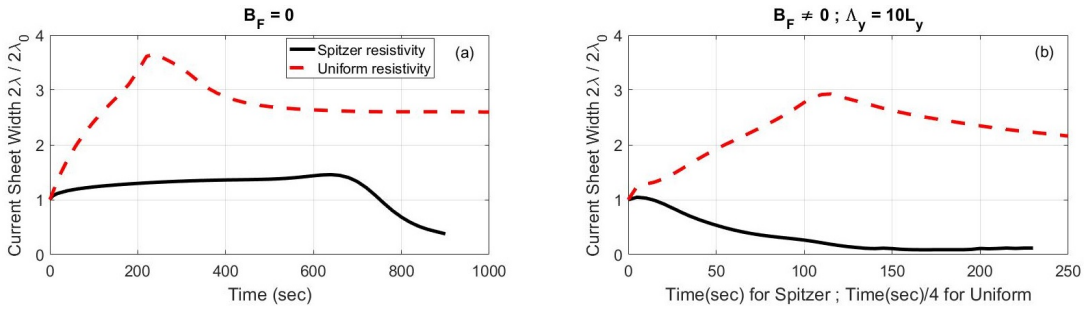

Figure 7.3: We present time evolution of the current sheet width, normalized to its initial value $2\lambda_0 = 250$ km, of the MGR cases for both the Spitzer and the uniform resistivity models. The panel (a) is for $B_F = 0$ and the panel (b) refers to $B_F \neq 0$ for $\Lambda_y = 10Ly$. The black solid line refers to Spitzer while the red dashed line is for the uniform resistivity. The time step of the MGR case with B_F using uniform resistivity, i.e. the red dashed curve in panel (b), is set to 1/4 sec for clarity.

7.2.2 Characterization of the MGR using the Uniform Resistivity Model

As discussed in Chapter 6, jets of plasma particles are detected in the outflow directions along the y-axis, and the increase in the Mach number is accompanied by a density decrease caused by the open boundary conditions of the simulation. In what follows in this section, we want to (1) investigate the time dependence of some of the main physical quantities for the MGR cases with and without B_F using the uniform resistivity model, and (2) to compare their behaviors to those of the same quantities obtained by the MGR cases using the Spitzer-like resistivity.

The panels (a) and (b) of Figure (7.4) show the time evolution of the maximum of the Mach number in the y-direction for the MGR cases, with and without B_F, using the Spitzer and the uniform resistivity models. According to panel (a) where $B_F = 0$, the maximum of the Mach number starts showing relatively higher values at $t > 200$ sec compared to those at $t < 200$ sec, whereas similar behavior takes place for the Spitzer resistivity model starting at $t > 600$ sec.

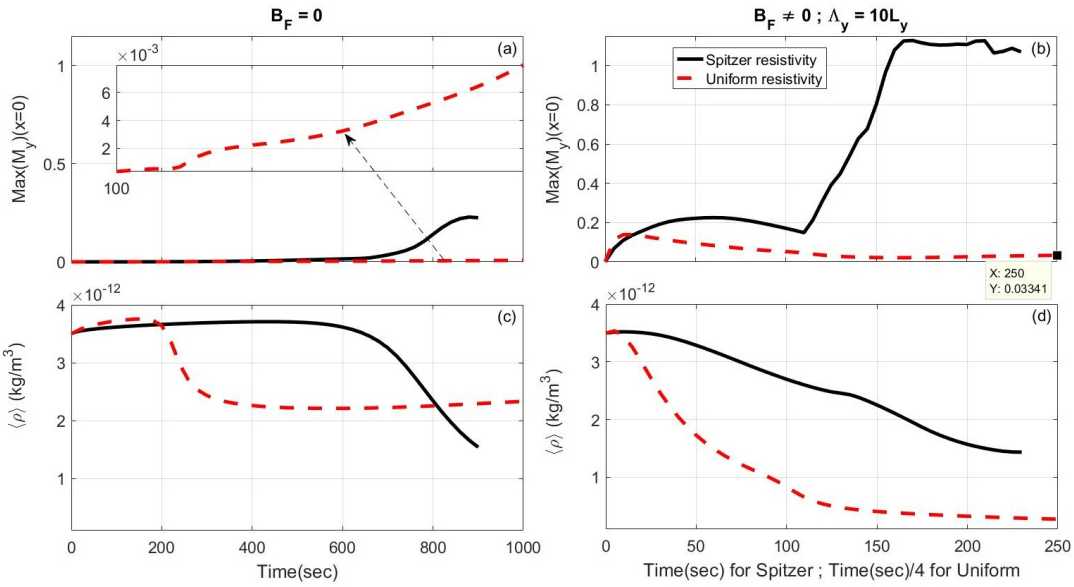

Figure 7.4: The left panels (a) and (c) present respectively the time dependence of the maximum of the Mach number associated with the velocity in the y-direction Max(M_y) and the mean plasma density $\langle\rho\rangle$ for the MGR cases without B_F. The right panels (b) and (d) presents respectively the time dependence of the same quantities for the MGR cases with B_F for $\Lambda_y = 10L_y$. The black solid and the red dashed lines are for the MGR cases using the Spitzer and the uniform resistivity models respectively. The time step of the MGR case with B_F using uniform resistivity, i.e. the red dashed curves in the right panels, is again set to 1/4 sec for clarity.

However, when fluctuations are added, we observe in panel (b) an early increase of Max(M_y) for the MGR case using the uniform resistivity, as in the case of Spitzer, and later it decreases. At the end of the simulation time, $t = 1000$ sec, we notice that Max(M_y) for both the MGR cases with $B_F \neq 0$, using the Spitzer and the uniform resistivity, reaches values that are greater by one order of magnitude compared to the cases without B_F.

We plot in the panels (c) and (d) of Figure (7.4) the time dependence of the spatial average of the density $\langle\rho\rangle$ for the two MGR cases with and without fluctuations using the Spitzer and the uniform resistivity models. As shown in (c) for the case without B_F using the uniform resistivity, $\langle\rho\rangle$ decreases at $t > 200$ sec, then it

becomes constant starting at $t > 400$ sec. For the case shown in (d) using uniform resistivity with $B_F \neq 0$, we observe an early decrease in $\langle\rho\rangle$ to reach lower values compared to $B_F = 0$ as well as to the case using the Spitzer resistivity for $B_F \neq 0$. Thus, the decrease in $\langle\rho\rangle$ occurs when Max(M_y) increases even for small values. Moreover, while the cases using the Spitzer resistivity with and without B_F lead to almost same value of $\langle\rho\rangle$ at the end of the simulation, we report more decrease in $\langle\rho\rangle$ for the case using the uniform resistivity with B_F than without.

In Figure (7.5), we show the time dependence of the maximum value in the

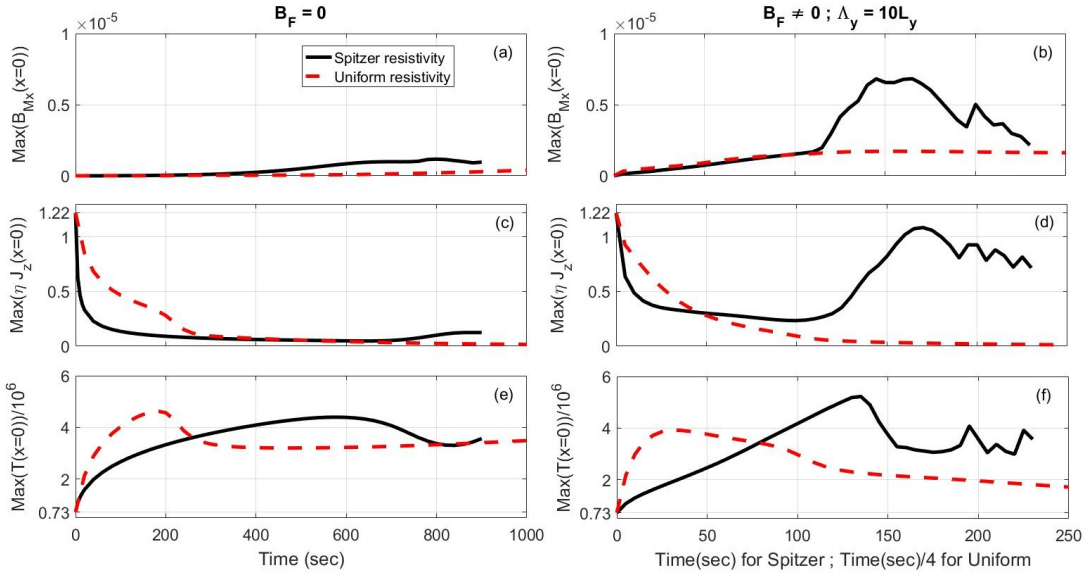

Figure 7.5: We show in the left panels (a), (c) and (e) respectively the temporal variation of the maximum value in the y-direction at $x = 0$ of B_{Mx}, ηJ_z and T for the MGR cases without fluctuations. We also show in the right panels (b), (d) and (f) the temporal variation of the same quantities for the MGR cases with fluctuations for $\Lambda_y = 10L_y$. The black solid and the red dashed lines are respectively for the MGR cases using the Spitzer and the uniform resistivity models. The red dashed curves in the right panels are also plotted with a time step divided by 4 for better visualization the results.

y-direction at $x = 0$ of B_{Mx}, ηJ_z and T for the MGR cases, with and without B_F, using the Spitzer and the uniform resistivity models. In (a) and (b), the case with B_F using uniform resistivity shows higher values of Max(B_{Mx}) compared to

the case without B_F. However, we do not observe a peak like the one we have in panel (b) for the Spitzer resistivity with fluctuations. The maximum value of the reconnection rate ηJ_z is plotted in (c) and (d) as a function of time. While we observe an increase in Max(ηJ_z) for the cases using the Spitzer resistivity with and without B_F, the cases using uniform resistivity always show a decrease in Max(ηJ_z). Thus, the cases using uniform resistivity does not lead to fast MGR process even if fluctuations are included. This is also in agreement with the work done by [136, 137, 138, 139, 119, 140, 141, 104] who showed that the fast reconnection mechanism can never be realized in the resistive MHD framework when the resistivity is uniform. The behavior of Max(T) as a function of time is shown in the panels (e) and (f) of Figure (7.5). In the cases using uniform resistivity with and without B_F, Max(T) increases to attain a maximum value of $\sim$ 5 MK for $B_F = 0$ and $\sim$ 4 MK for $B_F \neq 0$, then it decreases to values which are lower for $B_F \neq 0$ compared to $B_F = 0$. This is because the speed of the plasma particles along the y-direction, which leads to a density decrease, is greater with B_F than without as shown in the panels (b) and (d) of Figure (7.4). This also does not reflect a cooling of the plasma when T appears to decrease but rather the exit of the hot particles outside the computational domain. Finally, it is noticed that Max(T) reaches higher values when using Spitzer resistivity with fluctuations compared to the cases using uniform resistivity with and without B_F.

7.2.3 Energy Budget

We now discuss how the various forms of energy are distributed as a function of time during the MGR cases using the uniform resistivity model. Figure (7.6) presents the time evolution of the average total energy, $\langle E_{total} \rangle$, the average magnetic energy, $\langle E_{mag} \rangle$, the average internal energy, $\langle \varepsilon \rangle$, the average kinetic energy, $\langle E_k \rangle$ and the ohmic heating average energy $\langle E_h \rangle$ for $B_F = 0$ and $B_F \neq 0$ in panel

(a) and in panel (b) respectively.

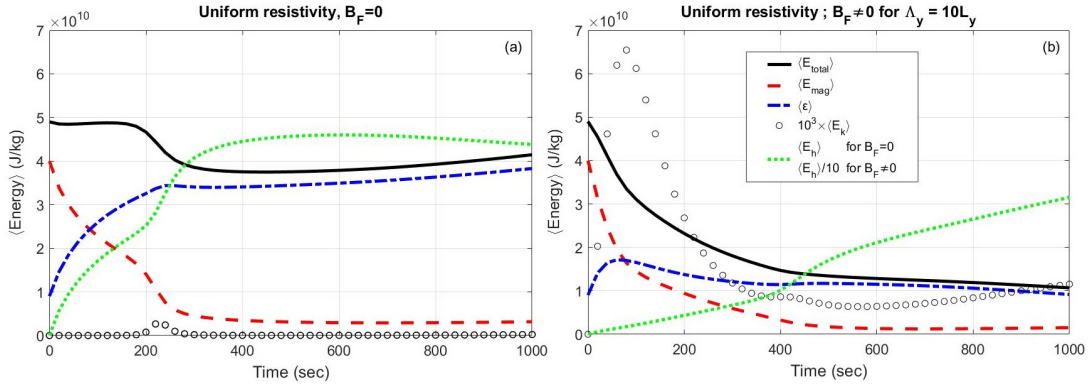

Figure 7.6: We present in (a) and (b) the energy budgets for the cases using the uniform resistivity model without B_F and with B_F respectively. The total energy $\langle E_{total} \rangle$ is in solid line, the magnetic energy $\langle E_{mag} \rangle$ is in dashed line, the thermal energy $\langle \varepsilon \rangle$ is in dashed-dotted line, the kinetic energy $\langle E_k \rangle$ multiplied by 1000 is in black circles, and the ohmic heating $\langle E_h \rangle$ is in dotted line. Note that the dotted line in (b) for $B_F \neq 0$ shows $\langle E_h \rangle / 10$.

We start with panel (a). The total energy remains almost constant up to $\sim$ 200 sec, then it drops to lower values which varies smoothly. The kinetic energy is multiplied by a factor of 1000 because it is small when compared to the other forms, and it shows little peak just after 200 sec. The magnetic energy decreases up to 300 sec after which it remains constant to a lower value compared to the initial one. This causes the heat and internal energy to increase up to $t \sim 300$ sec after which they show little variations in their values.

We observe in panel (b) for $B_F \neq 0$, that the total and the magnetic energy always decrease to reach lower values at $t = 1000$ sec compared to $B_F = 0$. The peak in the kinetic energy is observed almost 20 times larger and it occurs earlier compared to $B_F = 0$. The internal energy does not reach higher values as in the case without fluctuations. The heat energy continues increasing during the whole simulation time and it attains values at $t = 1000$ sec that are almost 7 times greater compared to $B_F = 0$. This is because the density $\langle \rho \rangle$ decreases more for $B_F \neq 0$ compared to $B_F = 0$ as noted previously in the panel (b) of

Figure (7.4).

The evolution of the MGR process is different using the uniform resistivity model instead of the Spitzer one. While we observe X-points and plasmoids when applying Spitzer-like resistivity, the MGR cases using uniform resistivity do not lead to such structures and we report only one big plasmoid extended in the whole computational box. However, adding fluctuations still accelerates the process so that the same behavior of the magnetic field lines are observed at a shorter time for $B_F \neq 0$ compared to $B_F = 0$. Nevertheless, we always witness slow MGR process when using uniform resistivity, which is in agreement with the literature.

Chapter 8

Simulation of MGR using the Spitzer Resistivity Model and Starting with Initial Velocity $\vec{u} \neq \vec{0}$

8.1 Introduction

All the cases of the MGR process done in Chapter 6 using the Spitzer resistivity model start with initial velocity equals to zero. However, our calculations are performed in a simulation box assumed to be a portion of the solar corona region at which flows of plasma particles always exist. Thus, a flow of plasma particles should be taken into consideration in order to make our simulation cases more realistic. The aim of this chapter is to investigate the results obtained from new MGR cases, with and without fluctuations, using the same functional form of the Spitzer resistivity applied in Chapter 6 and starting initially with a steady flow of particles along the outflow direction or the y-direction.

8.2 Error of $\vec{\nabla}.\vec{B}$

In this chapter, we perform two runs of the MGR process following the same simulation setup as in Chapter 6, same initial and boundary conditions and same mesh, except that we start with non-zero initial velocity along the y-direction, i.e. $u_y \neq 0$ at $t = 0$. The first case is done without B_F and the other case is done with B_F using only the longer wavelength of the fluctuations $\Lambda_y = 10L_y$.

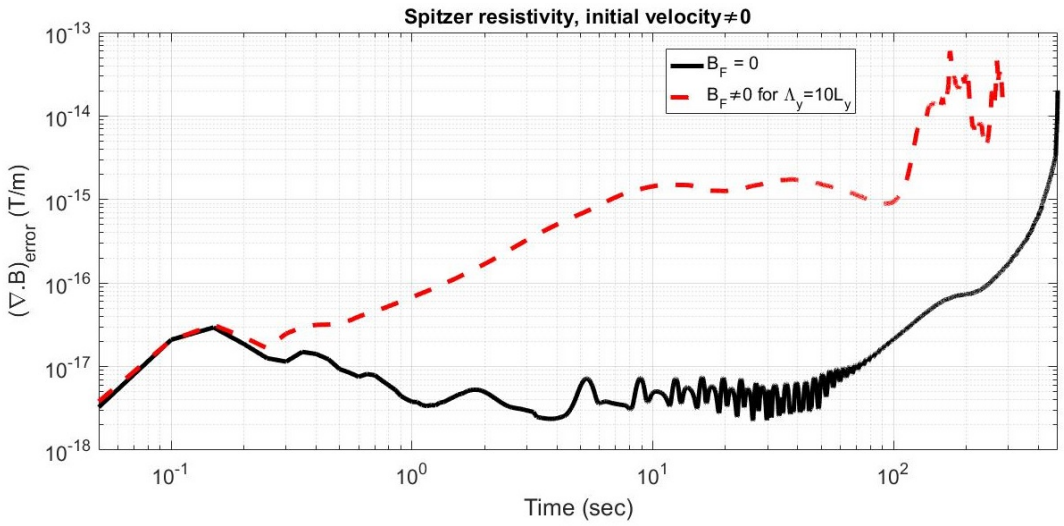

Figure 8.1: We present the temporal evolution of $(\vec{\nabla}.\vec{B})_{error}$ for the two new cases of the MGR process. The black solid line is for the MGR case without fluctuations ($B_F = 0$). The red dashed line is for the MGR case with fluctuations ($B_F \neq 0$) for $\Lambda_y = 10L_y$. Logarithmic scale is used for the two axes.

Following the same strategy, we start with the temporal variation of $(\vec{\nabla}.\vec{B})_{error}$ presented by Figure (8.1). As shown in the figure, the value of $(\vec{\nabla}.\vec{B})_{error}$ for $B_F = 0$ increases slowly with time up to 300 sec, then it increases rapidly and exceeds the critical value in a short time. Thus, we consider the temporal evolution up to 300 sec for the non-fluctuation case. Concerning the case with B_F, we find that $(\vec{\nabla}.\vec{B})_{error}$ starts increasing rapidly after $t > 100$ sec, and we present the results of the fluctuation case up to about 120 sec at which $(\vec{\nabla}.\vec{B})_{error}$ is still in the order of 10^{-15} T/m.

8.3 Results and Discussion

We set the initial velocity to be $\vec{u} = 0.1u_s\hat{y}$, where u_s is the sound speed equals to 100 km/sec at $t = 0$. Figure (8.2) shows the time evolution of Max(M_y), calculated in the y-direction at $x = 0$, and the mean plasma density $\langle\rho\rangle$ with and without fluctuations for initial velocity equal to and different from zero. The overall behaviors of Max(M_y) and $\langle\rho\rangle$ of these new cases with non-zero initial velocity are similar to those of Chapter 6 during 300 sec for $B_F = 0$ and 120 sec for $B_F \neq 0$. The main difference between the cases with and without initial velocity is the non-zero Mach number at $t = 0$.

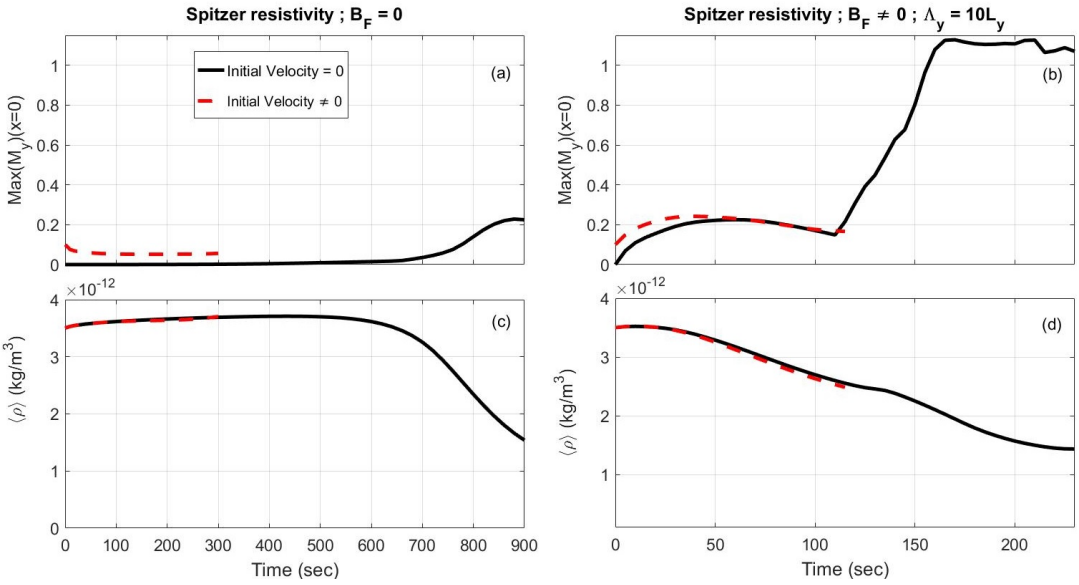

Figure 8.2: The left panels (a) and (c) present respectively the time dependence of Max(M_y) and the mean plasma density $\langle\rho\rangle$ for the MGR cases without B_F. The right panels (b) and (d) presents respectively the time dependence of the same quantities for the MGR cases with B_F for $\Lambda_y = 10L_y$. The black solid line is for the case without initial velocity presented previously in Chapter 6, and the red dashed line is for the case with initial velocity $u_y \neq 0$.

We show in Figure (8.3) the time evolution of Max(B_{Mx}), Max(ηJ_z) and Max(T), calculated in the y-direction at $x = 0$, for the MGR cases using the Spitzer-like resistivity with and without initial velocity for $B_F = 0$ and $B_F \neq 0$. It is observed

that the behaviors of these quantities for the new cases with initial velocity and for those without initial velocity are the same within 300 sec for $B_F = 0$ and 120 sec for $B_F \neq 0$.

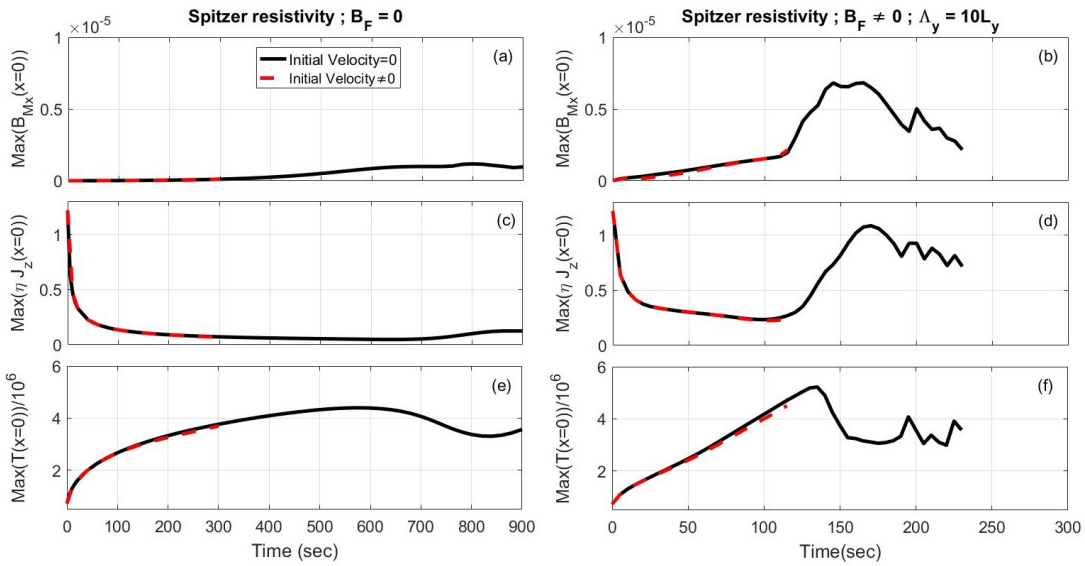

Figure 8.3: We show the temporal variation of Max(B_{Mx}), Max(ηJ_z) and Max(T) for the new cases using the Spitzer resistivity model with and without initial velocity. The left panels (a), (c) and (e) are for $B_F = 0$, whereas the right panels (b), (d) and (f) are for $B_F \neq 0$ using the fluctuation wavelength $\Lambda_y = 10L_y$. The maximum values of the mentioned quantities are calculated in the y-direction at $x = 0$. The black solid and the red dashed lines are respectively for the cases without initial velocity (presented previously in Chapter 6) and with initial velocity $u_y \neq 0$.

Figure (8.4) presents the time evolution of $\langle E_{total} \rangle$, $\langle E_{mag} \rangle$, $\langle \varepsilon \rangle$, $\langle E_k \rangle$ and $\langle E_h \rangle$ for $B_F = 0$ and $B_F \neq 0$ in panels (a) and (b) respectively. It is also noticed that the energy budgets for the new cases with initial velocity are similar to the cases without initial velocity, presented previously in Chapter 6, and the only difference is the non-zero kinetic energy at $t = 0$ as indicated by the figure.

In this chapter, we show part of the results of the new MGR cases using the Spitzer-like resistivity with initial velocity different from zero. We present the curves of the various quantities up to 300 sec for $B_F = 0$ and 120 sec for $B_F \neq 0$

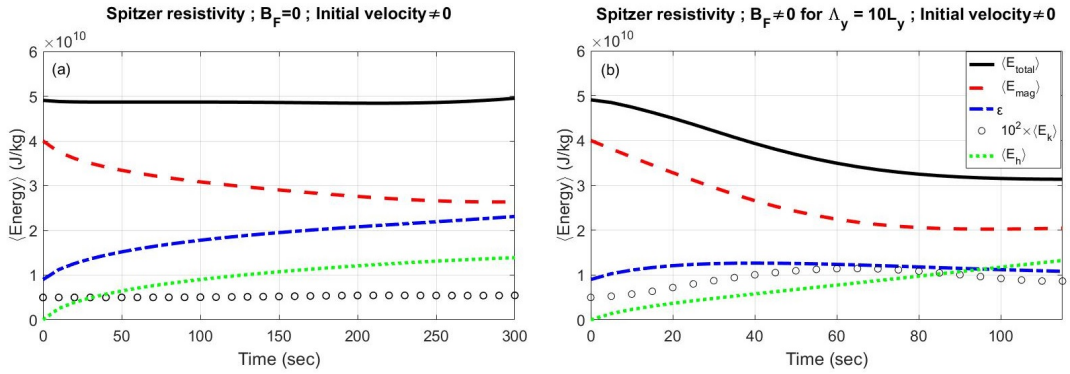

Figure 8.4: We present in (a) and (b) the energy budgets for the new cases, using the Spitzer resistivity model with and without initial velocity, for $B_F = 0$ and for $B_F \neq 0$ respectively. The total energy $\langle E_{total} \rangle$ is in solid line, the magnetic energy $\langle E_{mag} \rangle$ is in dashed line, the thermal energy $\langle \varepsilon \rangle$ is in dashed-dotted line, the kinetic energy $\langle E_k \rangle$ multiplied by 100 is in black circles, and the ohmic heating $\langle E_h \rangle$ is in dotted line.

during which $(\vec{\nabla}.\vec{B})_{error}$ does not exceed the critical value. After these two times, the results show numerical instabilities near the boundaries, not shown in the above results, which explains why $(\vec{\nabla}.\vec{B})_{error}$ exceeds the critical value at later times. As a future work, we intend to choose another type of boundary conditions that are more convenient with these MGR cases using a non-zero initial velocity along the outflow direction. By doing this, we thus are able to exploit the results for long simulation time with $(\vec{\nabla}.\vec{B})_{error} \lesssim 10^{-15}$ T/m.

Chapter 9

Summary, Conclusion and Future Work

9.1 Summary

Despite great advances in observations and modeling, the problem of solar coronal heating remains one of the most challenging problems in astrophysics. Heating in the solar corona is thought to be coming from many heating events [126]. This is the basic of the nanoflare hypothesis proposed by Parker in 1988 [142]. According to observations, it's difficult to survey one heating mechanism alone because several mechanisms may operate at the same time [54]. Recently, on August 2018, NASA has launched the first-ever mission to touch the Sun namely the "Parker Solar Probe" [143]. By capturing high resolution data, this spacecraft may find out how each individual heating mechanism will contribute in the global heating process of the solar corona.

MGR is modeled using many approaches, starting from the kinetic theory and ending with the single-fluid or MHD formulation, depending on the time and length scales of the plasma dynamics. For low frequency plasma compared to

the ion-cyclotron frequency and length-scales larger than the ion skin depth, the treatment of MGR can be done in the MHD framework. This reduces the plasma equations to only four which are the continuity, the momentum, the energy and the induction equations. These four equations form the so called: "resistive MHD model" if the plasma resistivity $\eta \neq 0$.

In the present thesis, we have made a serious effort to link the MGR process in the solar corona to the turbulent convective motion of the photospheric footpoints. We have done this link by assuming sinusoidal fluctuations in the coronal magnetic field, a sinusoidal behavior of footpoint motion is considered, and implementing them into the resistive MHD equations as source and sink terms (See Chapter 2). Thus, the fluctuations certainly lead to influence all the physical plasma quantities, including heating and particle acceleration, of the solar corona.

This treatment of fluctuations differs from that of the "forced reconnection model" in which a perturbation of the initially stationary force-free Harris sheet is introduced, in an initial time interval, via external boundary deformation [124, 125, 126, 127]. In our treatment, the fluctuations are applied for $t > 0$ over the whole mesh of our computational domain, and they are retained during the whole simulation time. We use static magnetic field fluctuations and we select typical values of their wavelengths based on the time-scales of the turbulent photospheric motion. The details of the calculations are summarized in Chapter 6.

The basic equations of our model are discretized into a system of linear algebraic equations using the finite volume method. They are implemented and solved using the openFoam code following two algorithms, PISO and BPISO. The PISO is used to guarantee the conservation of mass (continuity), whereas the BPISO is used to reduce the magnetic field divergence. Concerning $\vec{\nabla}.\vec{B}$, and since it is difficult to have zero-divergence for the magnetic field numerically, we

considered 10^{-15} T/m to be the order of $(\vec{\nabla}.\vec{B})_{error}$ below which the results are acceptable.

We performed in Chapter 6 three simulation cases of the MGR process using the Spitzer resistivity model without initial velocity. The first case is done without adding magnetic field fluctuations. The other two cases are done with fluctuations. The wavelengths of the fluctuations are respectively selected $\Lambda_y = L_y$ and $\Lambda_y = 10L_y$ to match our predictions of the time-scales of the photospheric footpoint motion. It is shown that the fluctuations contribute significantly to reconnection and heat processes of the solar corona.

We did in Chapter 7 two new cases using a uniform resistivity instead of the Spitzer-like one with and without fluctuations. We applied the same initial and boundary conditions using the same mesh as in Chapter 6. In fact, real plasma systems do not lead to a uniform resistivity, but it is important to see its effects on the evolution of the MGR process and to compare its results to those obtained using the Spitzer resistivity model. It is shown that the use of a uniform resistivity in the framework of resistive MHD does not exhibit a fast MGR process, which is well compared with the literature, even if fluctuations are added.

In Chapter 8 before concluding, we also did two other cases using the same functional form of the Spitzer-like resistivity as in Chapter 6, but we start the simulations with a non-zero initial velocity along the outflow direction (y-direction). The results behave similar to those obtained in Chapter 6 using zero initial velocity for short simulation time during which $(\vec{\nabla}.\vec{B})_{error}$ is below the critical value. However, some numerical instabilities near the boundaries are noticed at later times, which leads to have $(\vec{\nabla}.\vec{B})_{error} > 10^{-15}$ T/m. Thus, avoiding the numerical instabilities, to keep $(\vec{\nabla}.\vec{B})_{error}$ below the critical value and to exploit the results for long simulation time, is attributed to the best choice of the bound-

ary conditions that are convenient with the MGR cases using a non-zero initial velocity, and this is left for future work.

9.2 Conclusion

The results of the runs in the previous chapters are promising. The cases testing the dynamics of the MHD flow, with and without magnetic field, are well compared with the literature. In addition, the case of the Spitzer resistivity model, initiated by localized resistivity around the origin, shows also good agreement with the literature. All these test cases demonstrate that the MGR process is well handled in the MHD approach using our code. The following is the main results of the present work concluded for the cases of the MGR process with and without fluctuations using the Spitzer resistivity model and starting with a zero initial velocity (Chapter 6):

It is shown that for $B_F = 0$ the MGR tends to behave as that of the Sweet-Parker model, and the reconnection rate ηJ_z or M_A (~ 0.001) turns out to be slow and is not supported by observations. Moreover, two jets of accelerated particles are observed after relatively long simulation time of about 600 sec ($\sim 333\tau_A$), which leads to a dramatic decrease in the plasma density during a time range of about 300 sec ($\sim 167\tau_A$) and affects all other plasma quantities. When low-amplitude magnetic fluctuations of long wavelength, $\Lambda_y = 10L_y$, are added, the reconnection rate increases almost by a factor of 10 compared to $B_F = 0$, surpassing the threshold of the fast magnetic reconnection ($= 0.01$). We also find that the evolution of the magnetic field is strongly affected by this low-amplitude fluctuations that is 1% of B_0, where multiple plasmoids and X-points are detected. This differs the case for $B_F = 0$ where the formation of new plasmoids and X-points does not exist at all. Additionally, an early development of high-speed jets is noticed, which expel hot particles at a faster rate outside the simulation domain during a time range of about 210 sec ($\sim 116\tau_A$) compared to $B_F = 0$. It is also noticed

that the temperature amounts to higher values and the total energy decreases to lower values compared to $B_F = 0$. By decreasing the wavelength of the fluctuations, it is remarkable that the magnetic field evolution becomes further more complex where strong asymmetry is detected in the y-direction. Results show that the formation and evolution of plasmoids and X-points dominate when using fluctuations of shorter wavelength ($\Lambda_y = L_y$), and the temporal variation of the physical quantities takes place at shorter times compared to the fluctuations of longer wavelength ($\Lambda_y = 10L_y$). The temperature and the reconnection rate reach their maxima at about 80 sec ($\sim 44\tau_A$), which are almost the same maxima reached by those for $\Lambda_y = 10L_y$ but at longer times. The formation of the jets occurs even earlier compared to $\Lambda_y = 10L_y$, which leads to faster decrease of the plasma density during a time range of about 120 sec ($\sim 67\tau_A$). Consequently, the heat energy does not reach values as high as that for $B_F = 0$ because it is rapidly ejected out along with the expelled hot particles.

The existence of multiple X-points and plasmoids due to the addition of magnetic field fluctuations makes the MGR process faster. High-speed jets thus develop at early time, which govern the fast expulsion of hot plasma particles outside the simulation domain. Therefore, the heat generated by the MGR is convected out along with the hot particles (carriers of thermal energy), which leads to enhance heating of other coronal regions far from the reconnection site.

9.3 Future Work

Finally, we emphasize that our model is not restricted to static magnetic fluctuations and can include other forms that are varying with time. Thus, the model could be made more realistic when using space and time-dependent fluctuations, which mimic the real plasma dynamics supported by observations. For example, it is intriguing as future work to choose convenient functional forms for B_F to allow the field lines to oscillate in space and time. Temporal variation of the fluc-

tuation amplitude can be also investigated. Influx of plasma particles through the boundaries is a further example to simulate real coronal regions (Chapter 8), etc... . Moreover, our model can be applied also to investigate the MGR process in laboratory plasma devices, such as the plasma linear device (PLD) at AUB.

Appendix A

Abbreviations

MGR	Magnetic reconnection
MMS	Magnetospheric Multiscale Mission
PSP	Parker Solar Probe
MHD	Magnetohydrodynamics
HD	Hydrodynamics
PISO	Pressure-Implicit with Splitting Operators
BISO	Magnetic Pressure-Implicit with Splitting Operators
PDEs	Partial Differential Equations
FVM	Finite Volume Method
CFD	Computational Fluid Dynamics
PBA	Pressure Based Algorithm
SIMPLE	Semi-Implicit Method for Pressure-Linked Equations
SIMPLEC	SIMPLE Consistent
MCBA	Mass Conservation Based Algorithm
GCBA	Geometric Conservation Based Algorithm
OpenFOAM	Open source Field Operation And Manipulation
fvc	finite volume calculus

Appendix B

List Of Publications

In what follows, I included the list of my papers, conference and journal, that were done during the period it took to finalize this thesis. I only present the abstract of each paper to let the reader know the main results of the published work. The full text of those papers can be found online.

- Publication I: **Effect of magnetic reconnection in stellar plasma.**

  This conference paper has been presented during the international conference: "Frontiers in Theoretical and Applied Physics/UAE 2017 (FTAPS 2017)" that was held between 22^{nd} and 25^{th} of February 2017 at American University of Sharjah (AUS), UAE.

  Abstract:An important phenomenon in Astrophysics is the process of magnetic reconnection (MGR), which is envisaged to understand the solar flares, coronal mass ejection, interaction of the solar wind with the Earth's magnetic field (so called geomagnetic storm) and other phenomena. In addition, it plays a role in the formation of stars. MGR involves topological change of a set of magnetic field lines leading to a new equilibrium configuration of lower magnetic energy. The MGR is basically described in the framework of the Maxwell's equations linked to Navier-Stockes equations. Nevertheless, many details are still not understood. In this paper, we investigate the MGR process in the framework of the Magnetohydrodynamic (MHD) model of a single conducting fluid using a modern powerful computational tool (OpenFOAM). We will show that the MGR process takes place only if resistivity exists. However, despite the high conductivity of the plasma, resistivity becomes effective in a very thin layer generating sharp gradients of the magnetic field, and thus accelerating the reconnection process. The net effect of MGR is that magnetic energy is converted into thermal and kinetic energies leading to heating and acceleration of charged particles. The Sun's coronal ejection is an example of the MGR process.

- Publication II: **Role of Magnetic Reconnection in Heating Astrophysical Plasmas.**

  This conference paper has been presented during the international conference: "The 2017 American Geophysical Union (AGU) Fall Meeting" that was held between 11^{th} and 16^{th} of December 2017 in New Orleans, Louisiana, USA.

  Abstract:The description of plasma in the context of a fluid model reveals the important phenomenon of magnetic reconnection (MGR). This process is thought to be the cause of particle heating and acceleration in various astrophysical phenomena. Examples are geomagnetic storms, solar flares, or heating the solar corona, which is the focus of the present contribution. The magnetohydrodynamic approach (MHD) provides a basic description of MGR. However, the simulation of this process is rather challenging. Although it is not yet established whether waves or reconnection play the dominant role in heating the solar atmosphere, the present goal is to examine the tremendous increase of the temperature between the solar chromosphere and the corona in a very narrow transition region. Since we are dealing with very-high temperature plasma, the modeling of such heating process seems to require a two-fluid description consisting of ions and electrons. This treatment is an extension of the one-fluid model of resistive MHD that has been recently developed by (*Hammoud et al.*, 2017) [100] using the modern numerical openfoam toolbox. In this work, we outline the two-fluid approach using coronal conditions, show evidence of MGR in the two-fluid description, and investigate the temperature increase as a result of this MGR process.

- Publication III: **Effects of Magnetic Perturbation on Reconnection and Heating in the Solar Corona.**

  This journal paper has been submitted to the Astrophysical Journal (APJ) since May, 2020. This paper was done based on the results of Chapter 6 in this thesis.

  Abstract:The solar corona exhibits unusually high temperatures ($\sim 10^6$ K) compared to the temperature in the Sun's photosphere ($\sim$ 5800 K). This coronal heating is one of the fundamental problems in solar physics

that is yet to be resolved. Magnetic reconnection is thought to play a critical role in driving this enigmatic heating process. In this work, we present a newly-developed resistive magnetohydrodynamic (MHD) numerical model in which we investigate the effects of magnetic perturbations on the reconnection rate and the heating process in the solar corona. The perturbations are retained during the whole simulation time as they are assumed to be generated by the photospheric motion of footpoints. We use OpenFOAM to numerically solve the resistive MHD equations, which are modified by implementing the perturbations as sources or sinks. Our results show that including magnetic perturbations, even with a very small amplitude, leads to (1) more complex formation and evolution of X-points and plasmoids, (2) a transition from slow to fast reconnection rate, (3) a stronger increase of the temperature, and (4) a quicker formation of high-speed jets driving the hot plasma outside the simulation domain with a Mach number that is 6 times greater compared to the case without perturbations. Moreover, we also find that a magnetic perturbation with shorter wavelength promotes even a faster temporal evolution of the reconnection process than for the longer wavelength. Therefore, magnetic reconnection taking into account magnetic field perturbations leads to more effective heating of the solar corona.

Bibliography

[1] M. Darwish and F. Moukalled, "A fully coupled navier-stokes solver for fluid flow at all speeds," *Numerical Heat Transfer, Part B: Fundamentals*, vol. 65, no. 5, pp. 410–444, 2014.

[2] B. Favini, R. Broglia, and A. Di Mascio, "Multigrid acceleration of second-order eno schemes from low subsonic to high supersonic flows," *International journal for numerical methods in fluids*, vol. 23, no. 6, pp. 589–606, 1996.

[3] T. Warburton and G. Karniadakis, "A discontinuous galerkin method for the viscous mhd equations," *Journal of computational Physics*, vol. 152, no. 2, pp. 608–641, 1999.

[4] J. K. Hargreaves, *The solar-terrestrial environment: an introduction to geospace-the science of the terrestrial upper atmosphere, ionosphere, and magnetosphere*. Cambridge University Press, 1992.

[5] J. W. Freeman, *Storms in Space*. Cambridge University Press, 2001.

[6] M. Yamada, R. Kulsrud, and H. Ji, "Magnetic reconnection," *Reviews of Modern Physics*, vol. 82, no. 1, p. 603, 2010.

[7] R. M. Kulsrud, *Plasma physics for astrophysics*, vol. 77. Princeton University Press Princeton, 2005.

[8] E. G. Zweibel and M. Yamada, "Magnetic reconnection in astrophysical and laboratory plasmas," *Annual review of astronomy and astrophysics*, vol. 47, pp. 291–332, 2009.

[9] J. Ashbourn, L. Woods, and D. Kennedy, "Blinkers in the solar transition region," *The European Physical Journal D*, vol. 71, no. 3, p. 51, 2017.

[10] J. Zhao, B. Schmieder, H. Li, E. Pariat, X. Zhu, L. Feng, and M. Grubecka, "Observational evidence of magnetic reconnection for brightenings and transition region arcades in iris observations," *The Astrophysical Journal*, vol. 836, no. 1, p. 52, 2017.

[11] NASA, "The parker solar probe," 2018. https://www.nasa.gov/press-release/nasa-ula-launch-parker-solar-probe-on-historic-journey-to-touch-sun.

[12] J. Larmor, "How could a rotating body such as the sun become a magnet," *Rep. Brit. Adv. Sci.*, pp. 159–160, 1919.

[13] S. Tobias, "The solar dynamo," *Philosophical Transactions of the Royal Society of London. Series A: Mathematical, Physical and Engineering Sciences*, vol. 360, no. 1801, pp. 2741–2756, 2002.

[14] E. N. Parker, "Hydromagnetic dynamo models.," *The Astrophysical Journal*, vol. 122, p. 293, 1955.

[15] H. Babcock, "The topology of the sun's magnetic field and the 22-year cycle.," *The Astrophysical Journal*, vol. 133, p. 572, 1961.

[16] R. B. Leighton, "A magneto-kinematic model of the solar cycle," *The Astrophysical Journal*, vol. 156, p. 1, 1969.

[17] S. M. Tobias, N. H. Brummell, T. L. Clune, and J. Toomre, "Transport and storage of magnetic field by overshooting turbulent compressible convection," *The Astrophysical Journal*, vol. 549, no. 2, p. 1183, 2001.

[18] S. Sanchez, A. Fournier, K. J. Pinheiro, and J. Aubert, "A mean-field babcock-leighton solar dynamo model with long-term variability," *Anais da Academia Brasileira de Ciências*, vol. 86, no. 1, pp. 11–26, 2014.

[19] S. Braginskii, "Transport processes in a plasma," *Reviews of plasma physics*, vol. 1, p. 205, 1965.

[20] J. P. Freidberg, "Ideal magnetohydrodynamic theory of magnetic fusion systems," *Reviews of Modern Physics*, vol. 54, no. 3, p. 801, 1982.

[21] U. Shumlak and J. Loverich, "Approximate riemann solver for the two-fluid plasma model," *Journal of Computational Physics*, vol. 187, no. 2, pp. 620–638, 2003.

[22] J. Loverich, A. Hakim, and U. Shumlak, "A discontinuous galerkin method for ideal two-fluid plasma equations," *Communications in Computational Physics*, vol. 9, no. 2, pp. 240–268, 2011.

[23] P. A. Sweet, "14. the neutral point theory of solar flares," in *Symposium-International Astronomical Union*, vol. 6, pp. 123–134, Cambridge University Press, 1958.

[24] E. N. Parker, "Sweet's mechanism for merging magnetic fields in conducting fluids," *Journal of Geophysical Research*, vol. 62, no. 4, pp. 509–520, 1957.

[25] A. . Benz, "Flare observations," *Living reviews in solar physics*, vol. 14, no. 1, p. 2, 2017.

[26] E. G. Zweibel and M. Yamada, "Perspectives on magnetic reconnection," *Proceedings of the Royal Society A: Mathematical, Physical and Engineering Sciences*, vol. 472, no. 2196, p. 20160479, 2016.

[27] H. E. Petschek, "Magnetic field annihilation," *NASA Special Publication*, vol. 50, p. 425, 1964.

[28] D. Biskamp, "Magnetic reconnection via current sheets," *The Physics of fluids*, vol. 29, no. 5, pp. 1520–1531, 1986.

[29] R. M. Kulsrud, "Magnetic reconnection: Sweet-parker versus petschek," *Earth, Planets and Space*, vol. 53, no. 6, pp. 417–422, 2001.

[30] D. Uzdensky and R. Kulsrud, "Two-dimensional numerical simulation of the resistive reconnection layer," *Physics of Plasmas*, vol. 7, no. 10, pp. 4018–4030, 2000.

[31] J. Birn, J. Drake, M. Shay, B. Rogers, R. Denton, M. Hesse, M. Kuznetsova, Z. Ma, A. Bhattacharjee, A. Otto, *et al.*, "Geospace environmental modeling (gem) magnetic reconnection challenge," *Journal of Geophysical Research: Space Physics*, vol. 106, no. A3, pp. 3715–3719, 2001.

[32] M. Hesse and D. Winske, "Electron dissipation in collisionless magnetic reconnection," *Journal of Geophysical Research: Space Physics*, vol. 103, no. A11, pp. 26479–26486, 1998.

[33] K. Singh, K. Shibata, N. Nishizuka, and H. Isobe, "Chromospheric anemone jets and magnetic reconnection in partially ionized solar atmosphere," *Physics of Plasmas*, vol. 18, no. 11, p. 111210, 2011.

[34] J. Büchner, "Three-dimensional magnetic reconnection in astrophysical plasmaskinetic approach," in *Plasma Astrophysics And Space Physics*, pp. 25–42, Springer, 1999.

[35] P. Pongkitiwanichakul, K. D. Makwana, and D. Ruffolo, "Driving reconnection in sheared magnetic configurations with forced fluctuations," *Physics of Plasmas*, vol. 25, no. 2, p. 022114, 2018.

[36] A. Jafari and E. Vishniac, "Introduction to magnetic reconnection," *arXiv preprint arXiv:1805.01347*, 2018.

[37] M. Hoshino, A. Nishida, T. Yamamoto, and S. Kokubun, "Turbulent magnetic field in the distant magnetotail: Bottom-up process of plasmoid formation?," *Geophysical research letters*, vol. 21, no. 25, pp. 2935–2938, 1994.

[38] W. Matthaeus and S. L. Lamkin, "Turbulent magnetic reconnection," *The Physics of fluids*, vol. 29, no. 8, pp. 2513–2534, 1986.

[39] A. Lazarian and E. T. Vishniac, "Reconnection in a weakly stochastic field," *The Astrophysical Journal*, vol. 517, no. 2, p. 700, 1999.

[40] P. Goldreich and S. Sridhar, "Toward a theory of interstellar turbulence. 2: Strong alfvenic turbulence," *The Astrophysical Journal*, vol. 438, pp. 763–775, 1995.

[41] G. Kowal, A. Lazarian, E. Vishniac, and K. Otmianowska-Mazur, "Numerical tests of fast reconnection in weakly stochastic magnetic fields," *The Astrophysical Journal*, vol. 700, no. 1, p. 63, 2009.

[42] S. Servidio, W. Matthaeus, M. Shay, P. Cassak, and P. Dmitruk, "Magnetic reconnection in two-dimensional magnetohydrodynamic turbulence," *Physical review letters*, vol. 102, no. 11, p. 115003, 2009.

[43] N. Loureiro, D. Uzdensky, A. Schekochihin, S. Cowley, and T. Yousef, "Turbulent magnetic reconnection in two dimensions," *Monthly Notices of the Royal Astronomical Society: Letters*, vol. 399, no. 1, pp. L146–L150, 2009.

[44] D. Uzdensky, N. Loureiro, and A. Schekochihin, "Fast magnetic reconnection in the plasmoid-dominated regime," *Physical review letters*, vol. 105, no. 23, p. 235002, 2010.

[45] A. Bhattacharjee, Y.-M. Huang, H. Yang, and B. Rogers, "Fast reconnection in high-lundquist-number plasmas due to the plasmoid instability," *Physics of Plasmas*, vol. 16, no. 11, p. 112102, 2009.

[46] W. Daughton, V. Roytershteyn, B. Albright, H. Karimabadi, L. Yin, and K. J. Bowers, "Influence of coulomb collisions on the structure of reconnection layers," *Physics of Plasmas*, vol. 16, no. 7, p. 072117, 2009.

[47] N. Yokoi, R. Rubinstein, A. Yoshizawa, and F. Hamba, "A turbulence model for magnetohydrodynamic plasmas," *Journal of Turbulence*, no. 9, p. N37, 2008.

[48] N. Yokoi and M. Hoshino, "Flow-turbulence interaction in magnetic reconnection," *Physics of Plasmas*, vol. 18, no. 11, p. 111208, 2011.

[49] N. Yokoi, K. Higashimori, and M. Hoshino, "Transport enhancement and suppression in turbulent magnetic reconnection: A self-consistent turbulence model," *Physics of Plasmas*, vol. 20, no. 12, p. 122310, 2013.

[50] A. Grünwald, "Xlvi. on the remarkable relationships between the spectrum of water-vapour and the line-spectra of hydrogen and oxygen, and on the chemical structure of the two latter, and their dissociation in the sun's atmosphere," *The London, Edinburgh, and Dublin Philosophical Magazine and Journal of Science*, vol. 24, no. 149, pp. 354–367, 1887.

[51] B. Edlén and F. Tyrén, "Atomic energy states of an unusual type," *Nature*, vol. 143, no. 3631, p. 940, 1939.

[52] G. L. Withbroe and R. W. Noyes, "Mass and energy flow in the solar chromosphere and corona," *Annual review of astronomy and astrophysics*, vol. 15, no. 1, pp. 363–387, 1977.

[53] J. A. Klimchuk, "On solving the coronal heating problem," *Solar Physics*, vol. 234, no. 1, pp. 41–77, 2006.

[54] R. Erdélyi and I. Ballai, "Heating of the solar and stellar coronae: a review," *Astronomische Nachrichten: Astronomical Notes*, vol. 328, no. 8, pp. 726–733, 2007.

[55] P. J. Cargill, "The fine structure of a nanoflare-heated corona," *Solar physics*, vol. 147, no. 2, pp. 263–268, 1993.

[56] I. Roussev, K. Galsgaard, R. Erdélyi, and J. Doyle, "Modelling of explosive events in the solar transition region in a 2d environment-i. general reconnection jet dynamics," *Astronomy & Astrophysics*, vol. 370, no. 1, pp. 298–310, 2001.

[57] I. Roussev, K. Galsgaard, R. Erdélyi, and J. Doyle, "Modelling of explosive events in the solar transition region in a 2d environment-ii. various mhd experiments," *Astronomy & Astrophysics*, vol. 375, no. 1, pp. 228–242, 2001.

[58] I. Roussev, J. Doyle, K. Galsgaard, and R. Erdélyi, "Modelling of solar explosive events in 2d environments-iii. observable consequences," *Astronomy & Astrophysics*, vol. 380, no. 2, pp. 719–726, 2001.

[59] M. J. Aschwanden, R. W. Nightingale, J. Andries, M. Goossens, and T. Van Doorsselaere, "Observational tests of damping by resonant absorption in coronal loop oscillations," *The Astrophysical Journal*, vol. 598, no. 2, p. 1375, 2003.

[60] Y. B. ZelDovich and Y. P. Raizer, *Physics of shock waves and high-temperature hydrodynamic phenomena*. Courier Corporation, 2012.

[61] B. De Pontieu, R. Erdélyi, and S. P. James, "Solar chromospheric spicules from the leakage of photospheric oscillations and flows," *Nature*, vol. 430, no. 6999, p. 536, 2004.

[62] N. Freij, E. Scullion, C. Nelson, S. Mumford, S. Wedemeyer, and R. Erdélyi, "The detection of upwardly propagating waves channeling energy from the chromosphere to the low corona," *The Astrophysical Journal*, vol. 791, no. 1, p. 61, 2014.

[63] D. Gomez, "Heating of the solar corona," *Fundamentals of Cosmic Physics*, vol. 14, pp. 131–233, 1990.

[64] E. Priest and T. Forbes, "Book review: Magnetic reconnection/cambridge u press, 2000," *Irish Astronomical Journal*, vol. 27, p. 235, 2000.

[65] B. Roberts and V. Nakariakov, "Theory of mhd waves in the solar corona," in *Turbulence, Waves and Instabilities in the Solar Plasma*, pp. 167–191, Springer, 2003.

[66] R. Erdélyi, "Heating of the solar corona," in *British–Romanian–Hungarian N+ N+ N Workshop for Young Researchers*, p. 7, 2005.

[67] E. Parker, "Comments on the reconnexion rate of magnetic fields," *Journal of Plasma Physics*, vol. 9, no. 1, pp. 49–63, 1973.

[68] D. Biskamp, "Nonlinear magnetohydrodynamics, volume 1 of cambridge monographs on plasma physics," 1993.

[69] A. Bhattacharjee, "Impulsive magnetic reconnection in the earth's magnetotail and the solar corona," *Annu. Rev. Astron. Astrophys.*, vol. 42, pp. 365–384, 2004.

[70] E. Priest and T. Forbes, "Magnetic reconnection: Mhd theory and applications, 2000."

[71] M. Ugai, "Computer studies on the spontaneous fast reconnection model as a nonlinear instability," *Physics of Plasmas*, vol. 6, no. 5, pp. 1522–1531, 1999.

[72] D. A. Uzdensky, "Petschek-like reconnection with current-driven anomalous resistivity and its application to solar flares," *The Astrophysical Journal*, vol. 587, no. 1, p. 450, 2003.

[73] T. Yokoyama and K. Shibata, "Magnetohydrodynamic simulation of a solar flare with chromospheric evaporation effect based on the magnetic reconnection model," *The Astrophysical Journal*, vol. 549, no. 2, p. 1160, 2001.

[74] G. Dennis *et al.*, "Multi-fluid plasma modelling," 2005.

[75] B. B. Rossi and S. Olbert, "Introduction to the physics of space," 1970.

[76] D. R. Nicholson and D. R. Nicholson, *Introduction to plasma theory*. Wiley New York, 1983.

[77] F. F. Chen *et al.*, *Introduction to plasma physics and controlled fusion*, vol. 1. Springer, 1984.

[78] J. D. Jackson, *Classical electrodynamics*. John Wiley & Sons, 2012.

[79] H. Goedbloed, R. Keppens, and S. Poedts, *Magnetohydrodynamics: Of Laboratory and Astrophysical Plasmas*. Cambridge University Press, 2019.

[80] R. J. Goldston and P. H. Rutherford, *Introduction to plasma physics*. CRC Press, 1995.

[81] S. Patankar, *Numerical heat transfer and fluid flow*. CRC press, 1980.

[82] F. Moukalled, L. Mangani, M. Darwish, *et al.*, "The finite volume method in computational fluid dynamics," *An Advanced Introduction with OpenFOAM and Matlab*, pp. 3–8, 2016.

[83] P. J. Oliveira, "Method for time-dependent simulations of viscoelastic flows: vortex shedding behind cylinder," *Journal of non-newtonian fluid mechanics*, vol. 101, no. 1-3, pp. 113–137, 2001.

[84] U.-L. Pen, P. Arras, and S. Wong, "A free, fast, simple, and efficient total variation diminishing magnetohydrodynamic code," *The Astrophysical Journal Supplement Series*, vol. 149, no. 2, p. 447, 2003.

[85] S. V. Patankar and D. B. Spalding, "A calculation procedure for heat, mass and momentum transfer in three-dimensional parabolic flows," in *Numerical Prediction of Flow, Heat Transfer, Turbulence and Combustion*, pp. 54–73, Elsevier, 1983.

[86] R. I. Issa, "Solution of the implicitly discretised fluid flow equations by operator-splitting," *Journal of computational physics*, vol. 62, no. 1, pp. 40–65, 1986.

[87] J. Van Doormaal and G. Raithby, "Enhancements of the simple method for predicting incompressible fluid flows," *Numerical heat transfer*, vol. 7, no. 2, pp. 147–163, 1984.

[88] S. Acharya and F. Moukalled, "Improvements to incompressible flow calculation on a nonstaggered curvilinear grid," *Numerical Heat Transfer, Part B Fundamentals*, vol. 15, no. 2, pp. 131–152, 1989.

[89] P. J. Oliveira, Raad I. Issa, "An improved piso algorithm for the computation of buoyancy-driven flows," *Numerical Heat Transfer: Part B: Fundamentals*, vol. 40, no. 6, pp. 473–493, 2001.

[90] M. Darwish, F. Moukalled, and B. Sekar, "A unified formulation of the segregated class of algorithms for multifluid flow at all speeds," *Numerical Heat Transfer: Part B: Fundamentals*, vol. 40, no. 2, pp. 99–137, 2001.

[91] F. Moukalled, M. Darwish, and B. Sekar, "A pressure-based algorithm for multi-phase flow at all speeds," *Journal of Computational Physics*, vol. 190, no. 2, pp. 550–571, 2003.

[92] F. Moukalled and M. Darwish, "Pressure-based algorithms for multifluid flow at all speedspart i: Mass conservation formulation," *Numerical Heat Transfer, Part B: Fundamentals*, vol. 45, no. 6, pp. 495–522, 2004.

[93] F. Moukalled and M. Darwish, "Pressure-based algorithms for multifluid flow at all speedspart ii: Geometric conservation formulation," *Numerical Heat Transfer, Part B: Fundamentals*, vol. 45, no. 6, pp. 523–540, 2004.

[94] M. Darwish, D. Asmar, and F. Moukalled, "A comparative assessment within a multigrid environment of segregated pressure-based algorithms for fluid flow at all speeds," *Numerical Heat Transfer, Part B: Fundamentals*, vol. 45, no. 1, pp. 49–74, 2004.

[95] U. Ziegler, "A semi-discrete central scheme for magnetohydrodynamics on orthogonal–curvilinear grids," *Journal of Computational Physics*, vol. 230, no. 4, pp. 1035–1063, 2011.

[96] G. Tóth, "The?· b= 0 constraint in shock-capturing magnetohydrodynamics codes," *Journal of Computational Physics*, vol. 161, no. 2, pp. 605–652, 2000.

[97] M. Zhang and X. Feng, "A comparative study of divergence cleaning methods of magnetic field in the solar coronal numerical simulation," *Frontiers in Astronomy and Space Sciences*, vol. 3, p. 6, 2016.

[98] X. Feng, *Magnetohydrodynamic Modeling of the Solar Corona and Heliosphere*. Springer, 2019.

[99] J. U. Brackbill and D. C. Barnes, "The effect of nonzero?· b on the numerical solution of the magnetohydrodynamic equations," *Journal of Computational Physics*, vol. 35, no. 3, pp. 426–430, 1980.

[100] M. Hammoud, M. El Eid, and M. Darwish, "Effect of magnetic reconnection in stellar plasma," in *Journal of Physics Conference Series*, vol. 869, 2017.

[101] M. M. Hammoud, M. El Eid, M. Darwish, and M. Dayeh, "Role of magnetic reconnection in heating astrophysical plasmas," in *AGU Fall Meeting Abstracts*, 2017.

[102] J. Balbás and E. Tadmor, "A central differencing simulation of the orszag-tang vortex system," *IEEE Transactions on Plasma Science*, vol. 33, no. 2, pp. 470–471, 2005.

[103] D. Derigs, A. R. Winters, G. J. Gassner, S. Walch, and M. Bohm, "Ideal glm-mhd: About the entropy consistent nine-wave magnetic field divergence diminishing ideal magnetohydrodynamics equations," *Journal of Computational Physics*, vol. 364, pp. 420–467, 2018.

[104] M. Ugai, "Physical conditions for fast reconnection evolution in space plasmas," *Physics of Plasmas*, vol. 19, no. 7, p. 072315, 2012.

[105] D. A. Gurnett and A. Bhattacharjee, *Introduction to plasma physics: with space and laboratory applications*. Cambridge university press, 2005.

[106] S. R. Spangler, "Joule heating and anomalous resistivity in the solar corona," *arXiv preprint arXiv:0812.4220*, 2008.

[107] M. G. Harrison and T. Neukirch, "One-dimensional vlasov-maxwell equilibrium for the force-free harris sheet," *Physical Review Letters*, vol. 102, no. 13, p. 135003, 2009.

[108] F. Wilson and T. Neukirch, "A family of one-dimensional vlasov-maxwell equilibria for the force-free harris sheet," *Physics of Plasmas*, vol. 18, no. 8, p. 082108, 2011.

[109] G. Vekstein, "Storing free magnetic energy in the solar corona," *Journal of Plasma Physics*, vol. 82, no. 4, 2016.

[110] M. Gordovskyy, P. Browning, and G. Vekstein, "Particle acceleration in fragmenting periodic reconnecting current sheets in solar flares," *The Astrophysical Journal*, vol. 720, no. 2, p. 1603, 2010.

[111] D. M. Long, D. R. Williams, S. Régnier, and L. K. Harra, "Measuring the magnetic-field strength of the quiet solar corona using eit waves," *Solar Physics*, vol. 288, no. 2, pp. 567–583, 2013.

[112] H. Morgan and Y. Taroyan, "Global conditions in the solar corona from 2010 to 2017," *Science advances*, vol. 3, no. 7, p. e1602056, 2017.

[113] G. A. Gary, "Plasma beta above a solar active region: Rethinking the paradigm," *Solar Physics*, vol. 203, no. 1, pp. 71–86, 2001.

[114] T. Sakurai, "Heating mechanisms of the solar corona," *Proceedings of the Japan Academy, Series B*, vol. 93, no. 2, pp. 87–97, 2017.

[115] X. Feng, Y. Zhou, and S. Wu, "A novel numerical implementation for solar wind modeling by the modified conservation element/solution element method," *The Astrophysical Journal*, vol. 655, no. 2, p. 1110, 2007.

[116] M. Zhang, S.-T. J. Yu, S.-C. Chang, and I. Blankson, "Calculation of the ideal mhd equations by the cese method without special treatment for the divergence-free constraint of magnetic field," in *41st Aerospace Sciences Meeting and Exhibit*, p. 324, 2003.

[117] X. Feng, L. Yang, C. Xiang, S. Wu, Y. Zhou, and D. Zhong, "Three-dimensional solar wind modeling from the sun to earth by a sip-cese mhd model with a six-component grid," *The Astrophysical Journal*, vol. 723, no. 1, p. 300, 2010.

[118] M. Ugai and L. Zheng, "Conditions for the fast reconnection mechanism in three dimensions," *Physics of plasmas*, vol. 12, no. 9, p. 092312, 2005.

[119] M. Ugai, "The evolution of fast reconnection in a three-dimensional current sheet system," *Physics of Plasmas*, vol. 15, no. 8, p. 082306, 2008.

[120] E. N. Parker, "The solar-flare phenomenon and the theory of reconnection and annihiliation of magnetic fields.," *The Astrophysical Journal Supplement Series*, vol. 8, p. 177, 1963.

[121] P. Cassak, J. Drake, and M. Shay, "A model for spontaneous onset of fast magnetic reconnection," *The Astrophysical Journal Letters*, vol. 644, no. 2, p. L145, 2006.

[122] M. Ugai and T. Tsuda, "Magnetic field-line reconnexion by localized enhancement of resistivity: Part 1. evolution in a compressible mhd fluid," *Journal of Plasma Physics*, vol. 17, no. 3, pp. 337–356, 1977.

[123] T. Sato and T. Hayashi, "Externally driven magnetic reconnection and a powerful magnetic energy converter," *The Physics of Fluids*, vol. 22, no. 6, pp. 1189–1202, 1979.

[124] T. Hahm and R. Kulsrud, "Forced magnetic reconnection," *The Physics of fluids*, vol. 28, no. 8, pp. 2412–2418, 1985.

[125] G. Vekstein and R. Jain, "Energy release and plasma heating by forced magnetic reconnection," *Physics of Plasmas*, vol. 5, no. 5, pp. 1506–1513, 1998.

[126] R. Jain, P. Browning, and K. Kusano, "Solar coronal heating by forced magnetic reconnection: Multiple reconnection events," *Physics of plasmas*, vol. 12, no. 1, p. 012904, 2005.

[127] M. Gordovskyy, P. Browning, and G. Vekstein, "Particle acceleration in a transient magnetic reconnection event," *Astronomy & Astrophysics*, vol. 519, p. A21, 2010.

[128] K. Shibata, "Evidence of magnetic reconnection in solar flares and a unified model of flares," *Astrophysics and Space Science*, vol. 264, no. 1-4, pp. 129–144, 1998.

[129] F. Coroniti and A. Eviatar, "Magnetic field reconnection in a collisionless plasma," *The Astrophysical Journal Supplement Series*, vol. 33, pp. 189–210, 1977.

[130] F. V. Coroniti, "Explosive tail reconnection: The growth and expansion phases of magnetospheric substorms," *Journal of Geophysical Research: Space Physics*, vol. 90, no. A8, pp. 7427–7447, 1985.

[131] M. Ugai, "Computer studies on development of the fast reconnection mechanism for different resistivity models," *Physics of Fluids B: Plasma Physics*, vol. 4, no. 9, pp. 2953–2963, 1992.

[132] O. Buneman, "Dissipation of currents in ionized media," *Physical Review*, vol. 115, no. 3, p. 503, 1959.

[133] A. Lui, "A multiscale model for substorms," *Space Science Reviews*, vol. 95, no. 1-2, pp. 325–345, 2001.

[134] A. Lui, "Potential plasma instabilities for substorm expansion onsets," *Space Science Reviews*, vol. 113, no. 1-2, pp. 127–206, 2004.

[135] P. Petkaki and M. Freeman, "Nonlinear dependence of anomalous ion-acoustic resistivity on electron drift velocity," *The Astrophysical Journal*, vol. 686, no. 1, p. 686, 2008.

[136] M. Ugai, "Self-consistent development of fast magnetic reconnection with anomalous plasma resistivity," *Plasma physics and controlled fusion*, vol. 26, no. 12B, p. 1549, 1984.

[137] M. Scholer, "Undriven magnetic reconnection in an isolated current sheet," *Journal of Geophysical Research: Space Physics*, vol. 94, no. A7, pp. 8805–8812, 1989.

[138] T. Yokoyama and K. Shibata, "What is the condition for fast magnetic reconnection?," *The Astrophysical Journal*, vol. 436, pp. L197–L200, 1994.

[139] S. Nitta, S. Tanuma, K. Shibata, and K. Maezawa, "Fast magnetic reconnection in free space: self-similar evolution process," *The Astrophysical Journal*, vol. 550, no. 2, p. 1119, 2001.

[140] S. Zenitani and T. Miyoshi, "Magnetohydrodynamic structure of a plasmoid in fast reconnection in low-beta plasmas," *Physics of Plasmas*, vol. 18, no. 2, p. 022105, 2011.

[141] R.-L. Jiang, K. Shibata, H. Isobe, and C. Fang, "Detailed analysis of fan-shaped jets in three dimensional numerical simulation," *Research in Astronomy and Astrophysics*, vol. 11, no. 6, p. 701, 2011.

[142] E. Parker, "Nanoflares and the solar x-ray corona," *The Astrophysical Journal*, vol. 330, pp. 474–479, 1988.

[143] NASA, "The parker solar probe," 2018. https://www.nasa.gov/press-release/nasa-ula-launch-parker-solar-probe-on-historic-journey-to-touch-sun.